Maria Leonor Carvalho Morgado

Licenciatura em Química Aplicada

Structural and functional studies of PpcA: a key protein in the electron transfer pathways of *Geobacter sulfurreducens*

Dissertação para obtenção do Grau de
Doutor em Bioquímica, ramo de Biotecnologia

Orientador: Prof. Carlos A. Salgueiro, Professor Auxiliar,
Faculdade de Ciências e Tecnologia, Universidade Nova de Lisboa

Júri:

Presidente:	Prof. Doutor Fernando Jorge da Silva Pina
Arguentes:	Prof. Doutor Brian James Goodfellow
	Doutora Inês Antunes Cardoso Pereira
Vogais:	Prof. Doutora Marta Bruix Bayés
	Prof. Doutor Carlos Alberto Gomes Salgueiro

FACULDADE DE CIÊNCIAS E TECNOLOGIA
UNIVERSIDADE NOVA DE LISBOA

Dezembro 2011

Universidade Nova de Lisboa

Maria Leonor Carvalho Morgado

Licenciatura em Química Aplicada

Structural and functional studies of PpcA: a key protein in the electron transfer pathways of *Geobacter sulfurreducens*

Dissertação para obtenção do Grau de
Doutor em Bioquímica, ramo de Biotecnologia

Orientador: Prof. Carlos A. Salgueiro, Professor Auxiliar,
Faculdade de Ciências e Tecnologia, Universidade Nova de Lisboa

FACULDADE DE CIÊNCIAS E TECNOLOGIA
UNIVERSIDADE NOVA DE LISBOA

Dezembro 2011

Structural and functional studies of PpcA: a key protein in the electron transfer pathways of *Geobacter sulfurreducens*

AGRADECIMENTOS

Apesar de uma tese ser apresentada em nome individual, esta resulta de um trabalho em equipa, e só foi possível devido ao trabalho e dedicação de diversas pessoas, às quais não posso deixar de agradecer.

Em primeiro lugar, ao meu orientador Prof. Doutor Carlos Salgueiro. Agradeço por ter acreditado nas minhas capacidades desde o início, por me ter iniciado no mundo da ciência e ter orientado ao longo deste trabalho. Agradeço a sua dedicação, disponibilidade, amizade, as inúmeras e infindáveis discussões, e por no final nunca desistir. Aprendi muito ao longo destes anos, especialmente a fazer um bom trabalho. E aprendi que quando se trabalha em equipa, trabalha-se melhor.

Devo um agradecimento especial à Prof. Doutora Marta Bruix, por me ter recebido por diversas vezes no seu laboratório no Instituto de Química-Física 'Rocasolano', Consejo Superior de Investigaciones Científicas em Madrid, e por me ter orientado e iniciado no mundo dos espectros de RMN tri-dimensionais. A sua confiança e entusiasmo são contagiantes e muito motivadores.

Ao Doutor Vítor Paixão agradeço toda a ajuda durante os cálculos para a determinação da estrutura do citocromo PpcA. Sem a sua ajuda, seria uma história sem fim.

Agradeço ao Prof. Doutor Derek R. Lovley a oportunidade de desenvolver parte deste projecto no seu laboratório na University of Massachusetts, integrado no Geobacter Project. Ao Doutor Muktak Aklukjar agradeço por me ter orientado e pela sua persistência. Agradeço ao Ashley Franks, Manju Sharma, Joy Ward, Ching Leang, Sarah, Roberto, Joanne e Zara pela sua disponibilidade e amizade durante a minha estadia em Amherst.

Agradeço à Prof. Doutora Marianne Schiffer, ao Doutor P. Raj. Pokkuluri e ao Doutor. Yuri Y. Londer do Argonne National Laboratory pela disponibilização das proteínas e dos plasmídeos, e as inúmeras discussões científicas.

Ao Prof. Doutor David L. Turner agradeço a disponibilização dos programas de cálculo para determinação dos parâmetros termodinâmicos de proteínas multihémicas e da estrutura de proteínas. Agradeço também a sua ajuda nos cálculos preliminares da estrutura do PpcA no estado paramagnético oxidado.

Agradeço ao Doutor Ricardo O. Louro e à Prof. Doutora Teresa Catarino as diversas sugestões e discussões quer de carácter experimental, quer de carácter teórico, e a disponibilidade na logística da utilização da câmara anaeróbica no ITQB.

Agradeço à Prof. Doutora Isabel Couto pelo trabalho no desenvolvimento do protocolo de expressão para marcação isotópica de proteínas e pela ajuda e disponibilidade durante a implementação das ferramentas de Biologia Molecular no laboratório.

Agradeço ao Laboratório de RMN da FCT-UNL, integrado na Rede Nacional de RMN e financiado pela Fundação para a Ciência e Tecnologia através Projecto de Re-Equipamento

Científico (REDE/1517/RMN/2005), pelo acesso aos espectrómetros de RMN. Agradeço a disponibilidade do Aldino Viegas, Daniel Jana, Prof. Doutor Eurico Cabrita e Doutor Ângelo Figueiredo, durante a utilização dos espectrómetros. Ao Daniel e ao Ângelo agradeço também toda a ajuda a nível informático na instalação dos programas de cálculo.

A todos os que passaram pelo Lab. 611 agradeço a ajuda, a disponibilidade, a amizade, os inóculos matinais, por aturarem os meus dias de mau feitio, e todos os cafés, bolachas e palhaçadas. Ana, André, Sílvia, Joana, Marta, Marta, Eduardo e Verónica: obrigada. Agradeço em especial à Ana pelo trabalho no desenvolvimento do protocolo de expressão para marcação isotópica de proteínas e pelas inúmeras ajudas na expressão das diferentes proteínas; à Sílvia e à Joana que trabalharam na caracterização de alguns dos mutantes; à Marta pela ajuda durante os crescimentos, e à Verónica por se ter aventurado comigo na primeira clonagem feita neste laboratório.

Agradeço aos vários colegas do DQ (não nomeio para que não falhe ninguém) que estiveram presentes ao longo destes anos, e que me ajudaram de alguma forma, quer na utilização de um equipamento, quer no empréstimo de um reagente, ou apenas pelas conversas de corredor. Estes anos também não teriam sido os mesmos sem os almoços com o Gang do Tupperware. Agradeço a companhia e a animação durantes os nossos almoços.

Não posso deixar de agradecer à minha família, por serem uma parte fundamental da minha vida. À minha Mãe e ao meu Pai agradeço todo o apoio e por quererem sempre saber como se estavam a portar as proteínas e as bactérias, e como o trabalho estava a correr. Agradeço à minha irmã Ana Luísa e ao João por estarem sempre por perto, e por me terem “dado” dois sobrinhos lindos durante estes anos. É por estas coisas que a vida vale a pena. Agradeço aos meus Avós por, mesmo não percebendo bem o que faço, saber que os faço sentir orgulhosos. De todos senti o apoio e a força, principalmente quando estava longe ou quando as coisas não corriam como esperado.

Aos meus amigos, e em especial às minhas grandes amigas, que sabem bem que não tenho jeito para estas coisas, penso que um obrigado diz tudo. Estiveram sempre comigo, e sei que vão continuar a estar.

Ao Filipe, obrigada por estares sempre ao meu lado, em tudo.

Por último, gostaria de agradecer o financiamento à Fundação para a Ciência e a Tecnologia através da Bolsa de Doutoramento SFRH/BD/37415/2007 e do Projecto PTDC/QUI/70182/2006 atribuído ao Prof. Carlos Salgueiro, e à Fundação das Universidades Portuguesas através da Acção Integrada E-69/07.

ABSTRACT

Geobacter species show an impressive respiratory versatility and can sustain their growth by using insoluble extracellular compounds as terminal electron acceptors. The genome of *Geobacter sulfurreducens* has been completely sequenced and it revealed an unprecedented number of putative *c*-type cytochromes, 73 of which with more than one heme binding site. Although numerous electron transfer proteins have been identified, the electron transfer pathways that allow *G. sulfurreducens* to obtain energy are still far from being understood.

Five homologous triheme cytochromes (PpcA-E) were identified in *G. sulfurreducens* periplasm and gene knockout studies revealed their involvement in Fe(III) and U(VI) extracellular reduction. This thesis focuses on the characterization of these proteins, with special emphasis on PpcA, the most abundant in *G. sulfurreducens'* periplasm.

PpcA, PpcB, PpcD and PpcE were thermodynamically characterized in detail using Nuclear Magnetic Resonance and ultraviolet-visible spectroscopy. The results obtained showed that PpcA and PpcD were able to perform e^-/H^+ energy transduction in addition to their role in the electron transfer pathways. No evidence for coupling of e^-/H^+ transfer was observed for PpcB and PpcE. The functional implications of these results are discussed.

PpcA solution structure in the fully reduced state was determined using NMR spectroscopy and the redox-Bohr center responsible for controlling the e^-/H^+ transfer was identified, as well as the putative interacting regions between PpcA and its redox partners.

In order to elucidate the physiologic function of PpcA individual key residues and understand its functional mechanism, a family of mutants covering the entire protein was prepared using site-directed mutagenesis. The results obtained revealed how proper tuning of the reduction potentials of the heme groups is fundamental to achieve concerted e^-/H^+ transfer.

Keywords: *Geobacter*, electron transfer, multiheme cytochromes, NMR, protein structure, site-directed mutagenesis

RESUMO

As bactérias do género *Geobacter* apresentam uma versatilidade respiratória impressionante. Estas conseguem crescer usando compostos extracelulares insolúveis como aceitadores finais de electrões. O genoma de *Geobacter sulfurreducens* foi sequenciado e possui um número nunca antes observado de possíveis citocromos do tipo *c*, 73 dos quais contendo mais do que um local de ligação para grupos hemo. Apesar de inúmeras proteínas de transferência electrónica terem sido identificadas, pouco se sabe sobre os caminhos de transferência electrónica que permitem a esta bactéria obter energia para o seu crescimento.

Cinco citocromos trihémicos homólogos (PpcA-E) foram identificados no periplasma de *G. sulfurreducens* e estudos de crescimento com deleção dos genes que os codificam revelaram o seu envolvimento na redução extracelular de Fe(III) e U(VI). Esta tese tem como objectivo a caracterização destas proteínas, com especial relevo no citocromo PpcA, o mais abundante no periplasma de *G. sulfurreducens*.

Os citocromos PpcA, PpcB, PpcD and PpcE foram caracterizados termodinamicamente pela utilização de espectroscopias de Ressonância Magnética Nuclear e ultravioleta-visível. Os resultados obtidos mostram que os citocromos PpcA e PpcD têm as propriedades necessárias para efectuar transdução de energia e^-/H^+ para além do seu papel nos caminhos de transferência electrónica. No entanto, não foram encontradas evidências para a transferência acoplada e^-/H^+ para os citocromos PpcB e PpcE. As implicações funcionais destes resultados são discutidas.

A estrutura do citocromo PpcA em solução no estado reduzido foi determinada por espectroscopia de RMN e o centro redox-Bohr responsável pelo controlo da transferência acoplada e^-/H^+ foi identificado, assim como as possíveis regiões de interacção entre o PpcA e os seus parceiros redox.

Com o objectivo de elucidar a função fisiológica de resíduos individuais no citocromo PpcA e compreender o seu mecanismo funcional, uma família de proteínas mutadas em diversos resíduos em toda a proteína foi preparada por mutagénese dirigida. Os resultados obtidos revelaram que a regulação precisa dos potenciais de redução dos grupos hemo é essencial para que ocorra transferência acoplada de e^-/H^+.

Palavras chave: *Geobacter*, transferência de electrões, citocromos multihémicos, Resonância Magnética Nuclear, estrutura de proteínas, mutagénese dirigida

TABLE OF CONTENTS

FIGURES INDEX

1. INTRODUCTION

2. EXPERIMENTAL PROCEDURES

3. THERMODYNAMIC CHARACTERIZATION OF A TRIHEME CYTOCHROME FAMILY FROM *GEOBACTER SULFURREDUCENS*

4. STRUCTURAL STUDIES ON PPCA

5. FUNCTIONAL ROLE OF PPCA KEY AMINO ACIDS

6. ONGOING STUDIES

7. FINAL CONSIDERATIONS

APPENDIX

TABLES INDEX

ABBREVIATIONS, SYMBOLS AND CONSTANTS

1D – one dimensional

2D – two dimensional

3D – three dimensional

AQDS – anthraquinone-2,6-disulfonate

AMP – ampicillin

ATP – adenosine triphosphate

BLAST – Basic Local Alignment Search Tool

BMRB – Biological Magnetic Resonance Data Bank

CLO – chloramphenicol

COSY – COrrelation SpectroscopY

D. acetoxidans – *Desulfuromonas acetoxidans*

Dac$_7$ – *Desulfuromonas acetoxidans* c_7 cytochrome

DL1 – *G. sulfurreducens* wild-type strain

DL3 – *G. sulfurreducens* strain with *ppcA* gene knocked-out

DNA – deoxyribonucleic acid

*Dv*Hc_3 – *Desulfovibrio vulgaris* strain Hildenborough tetraheme cytochrome c_3

*Dv*Mc_3 – *Desulfovibrio vulgaris* strain Miyazaki tetraheme cytochrome c_3

E. coli – *Escherichia coli*

e_{app} – apparent midpoint reduction potential

EDTA – ethylenediamine tetraacetic acid

EXSY – EXchange SpectroscopY

G. sulfurreducens – *Geobacter sulfurreducens*

Gsc$_7$ – *Geobacter sulfurreducens* cytochromes c_7

HSQC - Heteronuclear Single-Quantum Correlation

IPTG – isopropyl β-D-1-thiogalactopyranoside

IUPAC-IUB – International Union of Pure and Applied Chemistry and International Union of Biochemistry

lov – lower limit volume

MQH_2 – menaquinol

MQ – menaquinone

NMR – Nuclear Magnetic Resonance

NOE – Nuclear Overhauser Effect

NOESY – Nuclear Overhauser Enhancement SpectroscopY

OD_{600} – optical density at 600 nm

PDB – Protein Data Bank

pI – isoelectric point

PpcA – *G. sulfurreducens* c_7 cytochrome (GSU0612)

PpcB – *G. sulfurreducens* c_7 cytochrome (GSU0364)

PpcC – *G. sulfurreducens* c_7 cytochrome (GSU0365)

PpcD – *G. sulfurreducens* c_7 cytochrome (GSU1024)
PpcE – *G. sulfurreducens* c_7 cytochrome (GSU1760)
ppm – parts per million
rmsd – root mean square deviation
SDS-PAGE – sodium dodecyl sulfate polyacrylamide gel electrophoresis
SHE – Standard Hydrogen Electrode
TOCSY – TOtal Correlation SpectroscopY
Tris – tris(hydroxymethyl)aminomethane
upl – upper distance limit
upv – upper limit volume
UV-visible – ultraviolet-visible

δ - chemical shift

F – Faraday constant (96485 $Cmol^{-1}$)
R – molar gas constant (8.314 $JK^{-1}mol^{-1}$)

Amino acid abbreviations

Alanine	Ala	A
Arginine	Arg	R
Asparagine	Asn	N
Aspartate	Asp	D
Cysteine	Cys	C
Glutamate	Glu	E
Glutamine	Gln	Q
Glycine	Gly	G
Histidine	His	H
Isoleucine	Ile	I
Leucine	Leu	L
Lysine	Lys	K
Methionine	Met	M
Phenylalanine	Phe	F
Proline	Pro	P
Serine	Ser	S
Threonine	Thr	T
Tryptophan	Trp	W
Tyrosine	Tyr	Y
Valine	Val	V

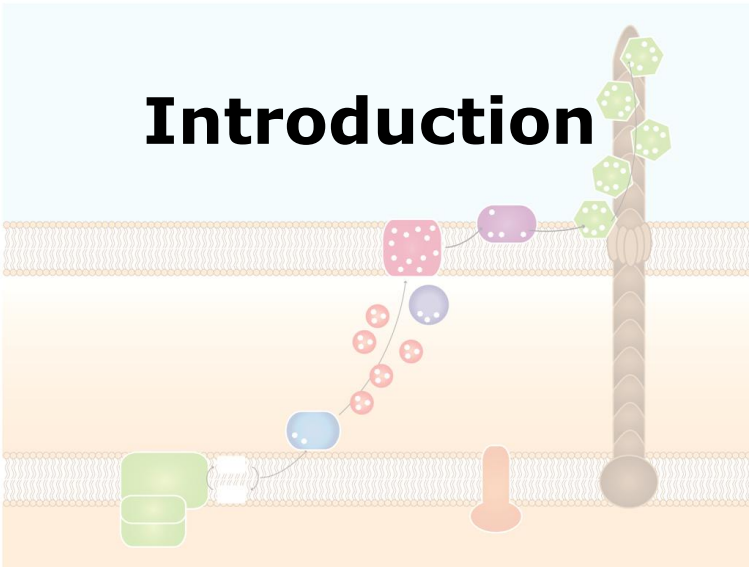
Introduction

1. INTRODUCTION

Dissimilatory metal reduction is the process by which microorganisms couple the oxidation of organic matter with the reduction of metal ions for other purposes than its assimilation into cellular components. These processes play important roles in the biogeochemical cycles of metals as iron, manganese, uranium and chromium [1].

Geobacter species show an impressive respiratory versatility. These bacteria are able to sustain their growth by using extracellular compounds, as Fe(III), U(VI) or Mn(IV) oxides, as terminal electron acceptors, in addition to the more frequent respiratory processes, which use both soluble electron donors (*e.g.* acetate) and acceptors (*e.g.* fumarate) [1,2]. Some of these compounds are toxic or radioactive, making this organism a potential target for bioremediation and biotechnological applications.

Based on these skills and the fact that these bacteria are highly enriched in subsurface environments, several bioremediation applications towards the decontamination of different environments have been developed [2-4]. This includes the reduction of soluble U(VI) to insoluble U(IV) for the immobilization of uranium in contaminated ground waters [5,6] and the anaerobic benzene degradation in petroleum-contaminated aquifers [7]. These strategies rely on the stimulation of *Geobacter* growth by addition of an electron donor to the groundwater [4].

Geobacter species are also being used to harvest electricity from aquatic sediments and waste organic matter by growing with electrodes as electron acceptors in microbial fuel cells [8-11]. This characteristic of *Geobacter* as "The microbe electric" was highlighted as one of the 50 best inventions of 2009 by the Time Magazine.

1.1 The bacterium *Geobacter sulfurreducens*

The bacterium *Geobacter sulfurreducens* (*G. sulfurreducens*) PCA was described for the first time in 1994 after being isolated from surface sediments of hydrocarbon-contaminated ditch near Norman, Oklahoma, USA [12]. This was the first bacterium described that couples the oxidation of acetate or hydrogen to the reduction of Fe(III). Phylogenetic analysis of its 16S rRNA placed *G. sulfurreducens* in the subgroup of δ-proteobacteria [12].

The genome of *G. sulfurreducens* has been sequenced and it revealed an unprecedented number of 111 putative *c*-type cytochromes, 73 of which with more than one heme binding site [13]. *G. sulfurreducens* is the microorganism with the largest number of *c*-type cytochrome genes [14]. The co-existence of such a large number of multiheme cytochromes might help the organism to efficiently use a diverse range of respiratory pathways and highlights their involvement in a broad range of essential cellular functions.

In the last years, *G. sulfurreducens* DL1 (wild-type strain maintained for many transfers in laboratory) has been used as a model for the study of *Geobacteraceae* because a genetic system was developed for this bacterium [15]. This system allows the mutagenesis of the chromosome by gene replacement, to introduce foreign DNA by electroporation and to

express proteins from extrachromossomal elements. These advances enabled to study the effect of the deletion of some genes, as well as their expression *in trans*.

1.2 Extracellular electron transfer

Many of the terminal electron acceptors that can be used by *G. sulfurreducens* are insoluble and, thus, unable to diffuse inside the cells. Therefore, reduction of these acceptors cannot occur in the periplasm as for soluble acceptors, and requires electron transfer across the outer membrane [16,17].

To assist electron transfer to the cell exterior, the spatial disposition of the redox components in *G. sulfurreducens* cells differs from that of the majority of other microorganisms. In fact, in addition to the usual location in the inner membrane and periplasmic space, multiheme cytochromes have been identified in *G. sulfurreducens'* outer membrane [18].

Although numerous electron transfer proteins have been identified in *G. sulfurreducens*, the electron transfer pathways that allow this microorganism to obtain energy are still far from being understood. It is essential to obtain a detailed characterization of *G. sulfurreducens* electron transfer proteins before understanding these electron transfer mechanisms and delineate their physiological roles. Insights into electricity production mechanisms can arise from the elucidation of the cellular strategies that allow energy production from the reduction of natural extracellular terminal acceptors [9]. This is of major interest for the design of improved biotechnological applications.

1.3 Gene knockout and proteomic studies in *G. sulfurreducens*

Several studies have been made in order to identify the proteins involved in the different reduction pathways used by *G. sulfurreducens*. Proteomic analysis under different growth conditions and gene deletion studies were performed, with special focus on *c*-type cytochromes since these proteins may play an important role in electron transfer to extracellular electron acceptors. The results of these studies are summarized in Table 1.1.

Table 1.1 – Summary of gene knockout and proteomic studies on *G. sulfurreducens* *c*-type cytochromes.

Protein (GSU number)	Predicted number of heme groups	Predicted cellular localization	Gene knockout and proteomic studies
PpcB (GSU0364)	3	Periplasm	Detected in both Fe(III) citrate and Fe(III) oxide cultures, but more abundant in Fe(III) citrate [19]. Double deletion mutant with PpcC has U(VI) reduction affected [20].
PpcC (GSU0365)	3	Periplasm	Double deletion mutant with PpcB has U(VI) reduction affected [20].

Table 1.1 (cont.) – Summary of gene knockout and proteomic studies on *G. sulfurreducens c*-type cytochromes.

Protein (GSU number)	Predicted number of heme groups	Predicted cellular localization	Gene knockout and proteomic studies
MacA (GSU0466)	2	Periplasm	Deletion mutant reduction of U(VI) is affected [20]. Deletion mutant growth on Fe(III) citrate is impaired, by affecting OmcB expression [21]. More abundant during growth with Fe(III) oxides *vs.* Fe(III) citrate as electron acceptor [19].
PpcA (GSU0612)	3	Periplasm	Deletion mutant U(VI) and AQDS reduction is affected when acetate is electron donor [22]. Deletion mutant Fe(III) oxides reduction is affected [20]. Detected in both Fe(III) citrate and Fe(III) oxide cultures [19].
GSU0616	8	Periplasm	Deletion mutant has increased Fe(III) and U(VI) reducing activity [20].
OmcE (GSU0618)	4	Outer membrane	Deletion mutant growth in Fe(III) and Mn(IV) oxides is affected [18]; power production is affected but adapts with time [23]. More abundant during growth with Fe(III) citrate *vs.* fumarate as electron acceptor [24]. Deletion mutant reduction of U(VI) is affected [20]. No impact on current production [25].
PpcD (GSU1024)	3	Periplasm	More abundant during growth with Fe(III) oxides *vs.* Fe(III) citrate as electron acceptor [19].
GSU1334	7	Outer membrane	Reduction of U(VI) and Fe(III) oxides is affected [20]. More abundant during growth with Fe(III) oxides *vs.* Fe(III) citrate as electron acceptor [19].
PpcE (GSU1760)	3	Periplasm	Found only in cultures with Fe(III) citrate [19].
PgcA (GSU1761)	3	Periplasm	More abundant during growth with Fe(III) oxides *vs.* Fe(III) citrate as electron acceptor [19]. Increased expression in strains adapted to growth in Fe(III) oxides [26].
OmcZ (GSU2076)	7	Outer membrane	Severely inhibited current production and biofilm formation [25].
OmcF (GSU2432)	1	Outer membrane	Deletion mutant growth on Fe(III) citrate is impaired, by affecting OmcB expression [27]. Deletion mutant reduction of U(VI) is affected [20]. Deletion mutant decreased current production [28].
OmcS (GSU2504)	6	Outer membrane	Deletion mutant growth in Fe(III) and Mn(IV) oxides is affected [18]. Deletion mutant has no impact on current production [25]. Localized along the pili [29].
OmcC (GSU2731)	12	Outer membrane	Deletion mutant has no effect on Fe(III) [30] and U(VI) reduction [20].
OmcB (GSU2737)	12	Outer membrane	Deletion mutant grows poorly in Fe(III) citrate and doesn't grow in Fe(III) oxide [30] but there is no effect on reduction of electrodes and current production [23,25] or on U(VI) reduction [20]. More abundant during growth with Fe(III) citrate *vs.* fumarate as electron acceptor [24]. Affected by deletion of *omcF* [27], *omcG* and *omcH* genes [31].
GSU3332	2	Outer membrane	Reduction of U(VI) and Fe(III) oxides is affected in the deletion mutant [20]

From the results presented in Table 1.1 is possible to verify that *c*-type cytochromes can be involved not only in electron transfer but also in transcriptional and post-transcriptional regulation or processing in *G. sulfurreducens* [27,31]. It was also shown that deletion of individual genes for outer surface *c*-type cytochromes only partially inhibited humic substance or anthraquinone-2,6-disulfonate (AQDS, model compound for humics) reduction and suggested that there are multiple routes for transfer of electrons to these acceptors [32].

Based on all these studies, a model for electron transfer to Fe(III) oxides in *G. sulfurreducens* has been proposed (Figure 1.1) [9,17,29].

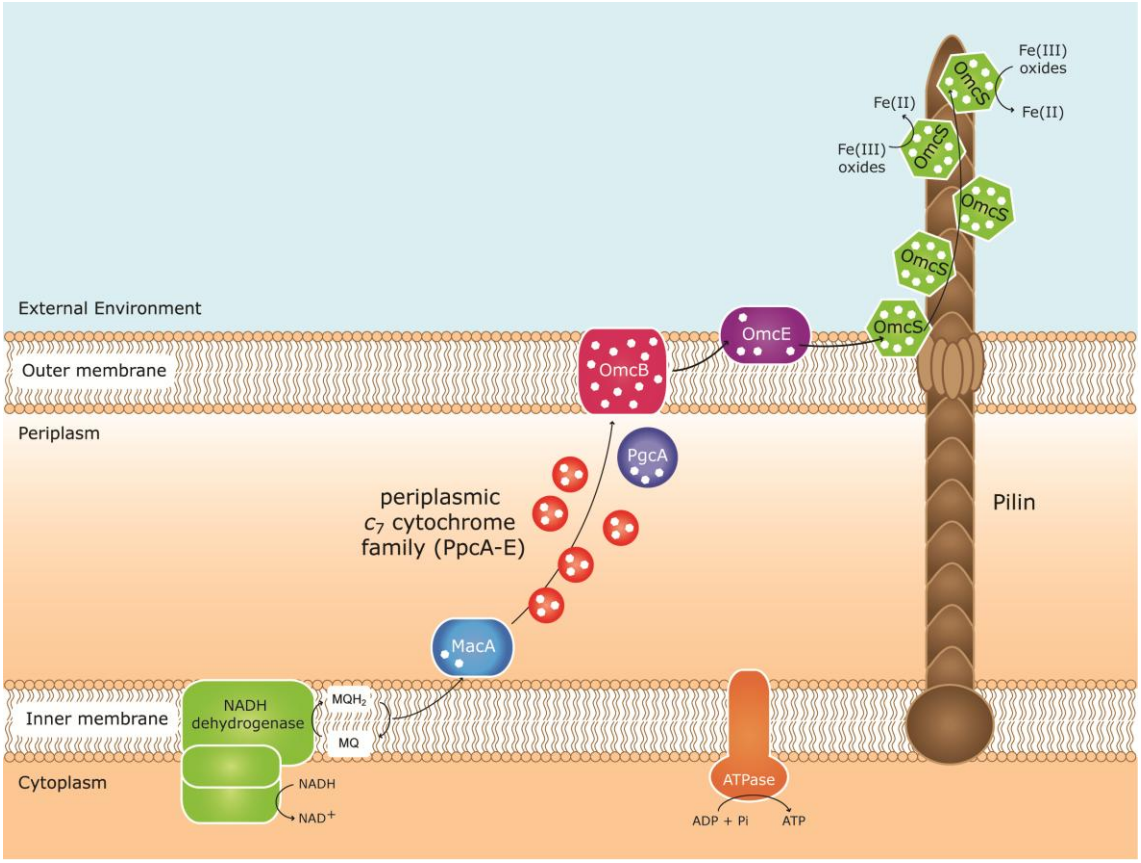

Figure 1.1 – Mechanism for extracellular electron transfer by *G. sulfurreducens*. Potential route for electron transfer to Fe(III) oxides based on previous models [9,17] and subsequent findings [26,29,33,34] (Table 1.1). The small white hexagons represent heme groups. MQH_2 is menaquinol and MQ is menaquinone.

Besides, the several cytochromes associated with the inner membrane, the periplasm and the outer membrane, it was shown that *G. sulfurreducens* forms pili when growing in Fe(III) oxides, and that these are essential for the contact with the oxides and for electron transfer [16]. Initial studies showed that pili were highly conductive and could serve as biological nanowires, working as the electrical connection between the cell and the surface of Fe(III) oxides [16]. However, more recent studies revealed that the hexaheme cytochrome OmcS was localized along the pili when *G. sulfurreducens* grows in Fe(III) oxides [29]. This suggests that pili may play a structural role by supporting *c*-type cytochromes along the way

to the surface of iron oxides [33,34]. It was proposed that cytochromes can also play a role in electron storage when an electron acceptor is not available [35]. However, the precise functions of these proteins are not yet elucidated and only a few components of the respiratory chain have been individually characterized so far.

The cytochrome OmcS has a molecular weight of 47 kDa, six heme groups and was purified from a strain that overproduces this protein [36]. Nuclear Magnetic Resonance (NMR) together with UV-visible spectroscopic studies allowed determining that all the heme groups are bis-histidinyl hexacoordinated and low spin in both fully oxidized and reduced states. The redox behavior of OmcS was studied by redox titrations followed by UV-visible [36]. It was observed that the six redox centers are not equivalent and the redox curve spans over a large range of reduction potentials from -360 mV to -40 mV. The midpoint reduction potential at pH 7 was -212 mV. Reduced OmcS was able to transfer electrons *in vitro* to different substrates as Fe(III) and Mn(IV) oxides and humic substances [36].

More related to electron transfer to electrodes, the cytochromes OmcF and OmcZ have also been characterized.

OmcF is a monoheme cytochrome with sequence similarity to soluble c_6 cytochromes of photosynthetic algae and cyanobacteria [37]. OmcF crystal structure was determined and was superimposable with a root mean square deviation (rmsd) of 1.1 Å to the structure of the cytochrome c_6 from the green alga *Monoraphidium braunii*. However the function of these two proteins is probably different, since their biochemical properties are very distinct. OmcF has an isoelectric point (pI) of 7.8 while *M. braunii* cytochrome has a pI of 4.2, and their reduction potentials at pH 7 are +180 mV and +357 mV, respectively [37].

OmcZ was shown be present in two forms in *G. sulfurreducens*: a large one ($OmcZ_L$) and a small one ($OmcZ_S$) that is a cleaved product from the first. $OmcZ_S$ is most probably the extracellular and active form [38]. $OmcZ_S$ has eight heme groups, seven bound to the typical heme binding motif CXXCH (where X represents any amino acid) and one with the unusual binding motif $CX_{14}CH$. A similar motif ($CX_{15}CH$) was identified in an octaheme protein from *Wolinella succinogenes* [39]. Redox titrations revealed that $OmcZ_S$ functional working potential range is between -420 mV and -60 mV with a midpoint reduction potential of -220 mV. *In vitro*, $OmcZ_S$ was able to transfer electrons to Fe(III) citrate, U(VI), Cr(VI), Au(III), Mn(IV) oxides, and AQDS, but not Fe(III) oxide [38].

1.4 Periplasmic cytochromes

In addition to the outer membrane cytochromes, an unusual periplasmic pool of five homologous triheme cytochromes (also known as c_7 cytochromes) was identified in *G. sulfurreducens* [40]. This family is considered essential in the bacterium electron transfer pathways since soluble periplasmic cytochromes are crucial for shuttling electrons from the cytoplasmic compartment to the outer membrane [9].

The five cytochromes are small proteins with approximately 10 kDa and a pI $\geq$ 9, due to the high content in lysine residues. The cytochromes are designated PpcA, PpcB, PpcC, PpcD, and PpcE (*Gsc*$_7$) and share a 77%, 62%, 57%, and 65% amino acid sequence identity with PpcA, respectively [40].

Using the PpcA amino acid sequence, the non-redundant amino acid database of NCBI using the Basic Local Alignment Search Tool (BLAST) [41] was searched and in addition to these five cytochromes c_7, 18 other cytochromes were found: five in *Geobacter metallireducens*, four in *Geobacter uraniireducens*, three in *Geobacter bemidjiensis*, two in *Anaeromyxobacter dehalogenans* and *Geobacter lovleyi*, and one in *Desulfuromonas acetoxidans* strain 5071 (*D. acetoxidans*) and in *Pelobacter propionicus*. A sequence alignment of these proteins is depicted in Figure 1.2 and shows that of the 21 highly conserved residues, only nine are not cysteine or histidine residues directly involved in heme binding.

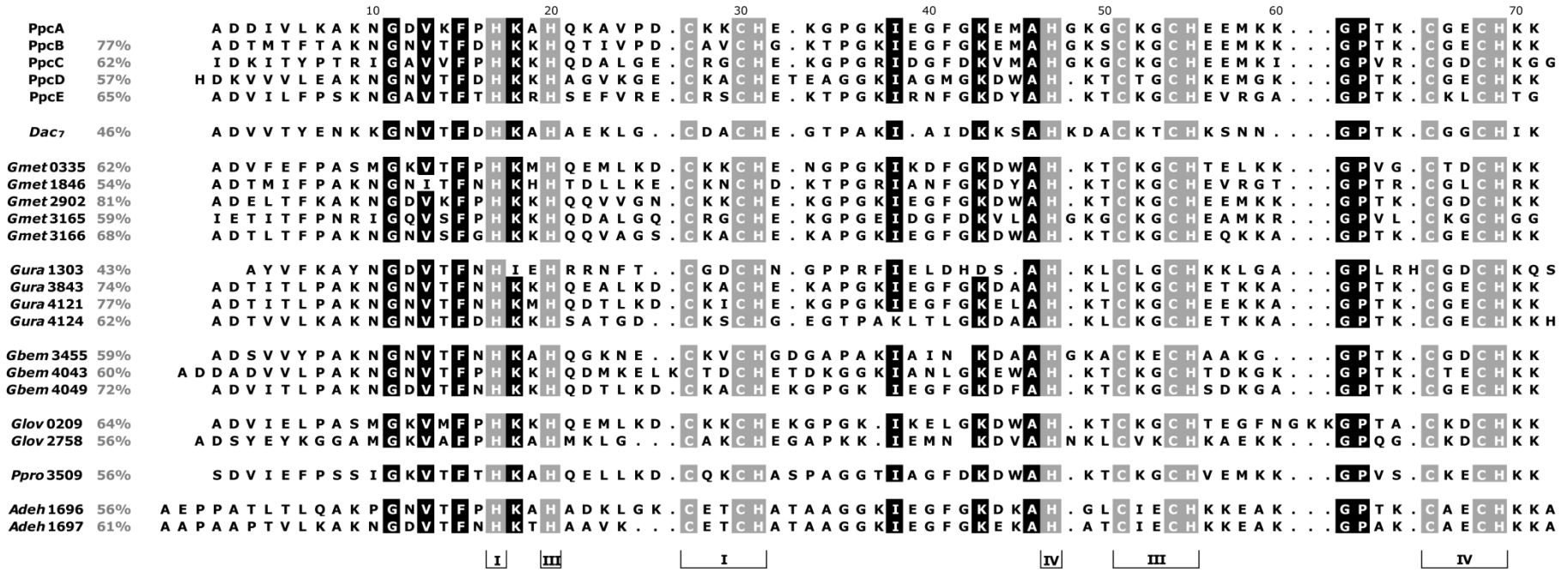

Figure 1.2 – Alignment of amino acid sequences of cytochromes c_7. PpcA, PpcB, PpcC, PpcD, PpcE, cytochromes c_7 from *Geobacter sulfurreducens*; Dac_7, cytochrome c_7 from *D. acetoxidans*; *Gmet*, *Geobacter metallireducens*; *Gura*, *Geobacter uraniireducens*; *Gbem*, *Geobacter bemidjiensis*; *Glov*, *Geobacter lovleyi*; *Ppro*, *Pelobacter propionicus*; *Adeh*, *Anaeromyxobacter dehalogenans*. The numbers refer to the gene that encodes each cytochrome. The conserved residues in the proteins are boxed: gray heme-attached residues and black non-heme-attached residues. The specific heme and the respective attached residues are indicated at the bottom of the last cytochrome c_7 amino acid sequence. The sequence identity for each cytochrome in relation to PpcA is also indicated.

The crystal structures of the five *G. sulfurreducens* c_7 cytochromes have been determined, showing that they have a high level of structural homology as depicted in Figure 1.3 [40,42,43].

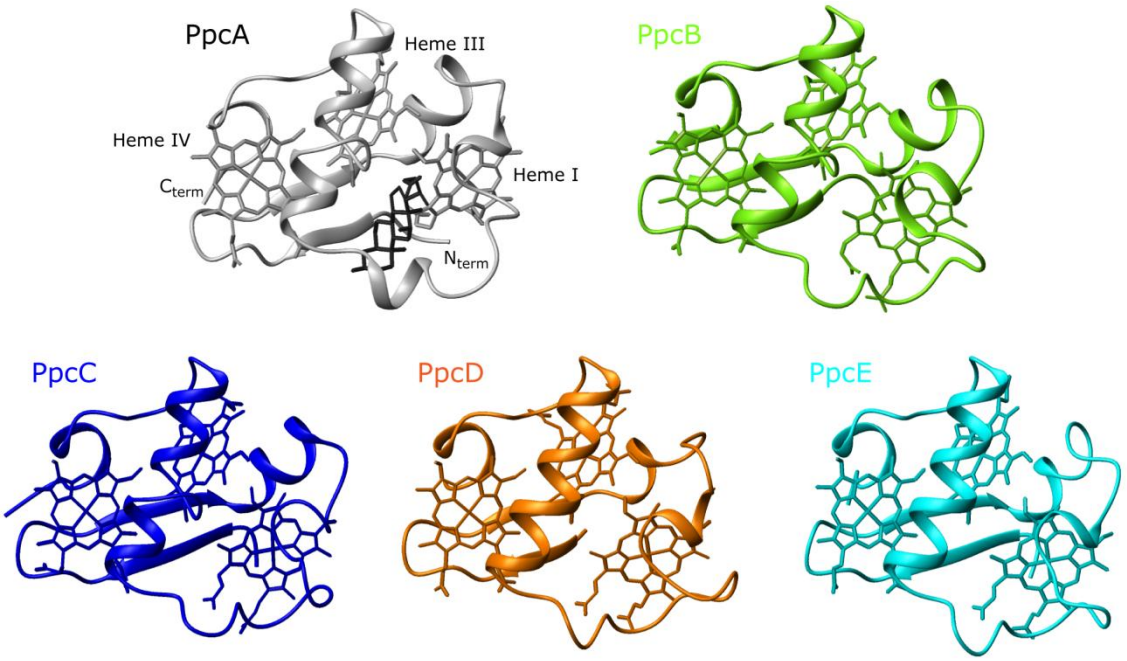

Figure 1.3 – Crystal structures of the five c_7 cytochromes from *G. sulfurreducens*. PpcA is represented in gray with the deoxycholate acid molecule used for crystallization in black (PDB 1OS6 [40]), PpcB in green (PDB 3BXU [43]), PpcC in blue (PDB 3H33), PpcD in orange (PDB 3H4N) and PpcE in cyan (PDB 3H34) [42]. PpcB and PpcD displayed two molecules in the crystal asymmetric unit (monomers A and B) and monomer A is represented. The molecules are all in the same orientation.

The spatial arrangements of the hemes in cytochromes c_7 are superimposable with those of the structurally homologous tetraheme cytochromes c_3, with the sole difference being lack of heme II and the corresponding polypeptide segment. For this reason, the three heme groups in cytochromes c_7 have been numbered as I, III, and IV [44].

The three heme groups form the protein core and are covalently linked to the cysteine residues of the CXXCH binding motifs (Figure 1.2). All the hemes are axially coordinated by two histidine residues and are low-spin both in the reduced (Fe(II), S = 0) and in the oxidized (Fe(III), S = ½) forms. The heme core structures are similar, with hemes I and III roughly parallel to each other and both nearly perpendicular to heme IV [40,42,43].

A two-strand β-sheet at the N-terminal is conserved in all the structures, and is followed by different helical regions in the different proteins [40,42,43]. The most conserved region is the positively charged surface around heme IV and the lowest similarity is found near heme I [42].

The only other c_7 cytochrome with structural information available is the one isolated from *D. acetoxidans* (*Dac*$_7$). The structure of this cytochrome has been studied by X-ray in its oxidized form [45], and by NMR in both redox states [46,47]. The overall fold of the polypeptide is similar to the *G. sulfurreducens* cytochromes; however, the heme core

rearrangement is somehow different, especially in the iron to iron distance between hemes I and IV (19.3 Å in *Dac*$_7$ compared to an average of 18.3 Å in the other proteins) [42].

The best studied *G. sulfurreducens* c_7 cytochrome is PpcA. In addition to the gene knockout and proteomic studies already described, the thermodynamic properties of the heme groups have been determined [48]. The results obtained showed that the heme groups of PpcA have negative reduction potentials that are modulated by heme-heme interactions and interactions with protonated groups (redox-Bohr effect). Taken together, the thermodynamic parameters obtained for PpcA showed that this protein is designed to present a preferential electron transfer pathway at physiologic pH coupled with proton transfer [48].

It had been previously showed that for growth in the presence of extracellular Fe(III) oxides, *G. sulfurreducens* needs additional e^-/H^+ coupling mechanisms in comparison to those used in fumarate respiration [49]. The authors suggested that the most likely mechanism for additional membrane potential generation is the coupling of electron transfer to the periplasmic cytochromes involved in the Fe(III) reduction with proton translocation, so that additional membrane potential can be generated for ATP production.

Since PpcA is known to be involved in Fe(III) reduction pathways, it was proposed that in the presence of extracellular electron acceptors PpcA might contribute to the H^+ electrochemical potential gradient across the periplasmic membrane that drives ATP synthesis [48]. These results contrast with the ones obtained for the triheme cytochrome *Dac*$_7$, which seems to be designed to work as simple electron transfer protein in the physiologic pH range [50].

1.5 Solution structures of multiheme proteins

Despite the cellular localization and phenotype associated to some *G. sulfurreducens* multiheme cytochromes are already known, no structural information in solution is available for any of these proteins. This relates with the traditional difficulties in obtaining isotopic labeled recombinant multiheme cytochromes with the correct fold and post-translational modification of the heme groups in a cost-effective manner [51-53].

Important contributions for the solution structure determination of multiheme cytochromes have been made by the research groups of Prof. António Xavier [54-58], Prof. Ivano Bertini [46,47] and Prof. Hideo Akutsu [59]. Although the proteins' molecular weights are appropriate for structural studies in solution, only a few structures have been determined for multiheme proteins. Indeed, reports of solution structures are still limited to five tetraheme cytochromes c_3 [54-59] and to one triheme cytochrome [46,47]. In total, ten solution structures have been reported, five for fully reduced proteins [46,54,56-58] and three for fully oxidized [47,54,55,58]. This clearly contrasts with the large number of structures determined by X-ray crystallography [60].

The smaller number of solution structures obtained in the oxidized form is undoubtedly associated with the inherent complexity of their NMR spectra (Figure 1.4).

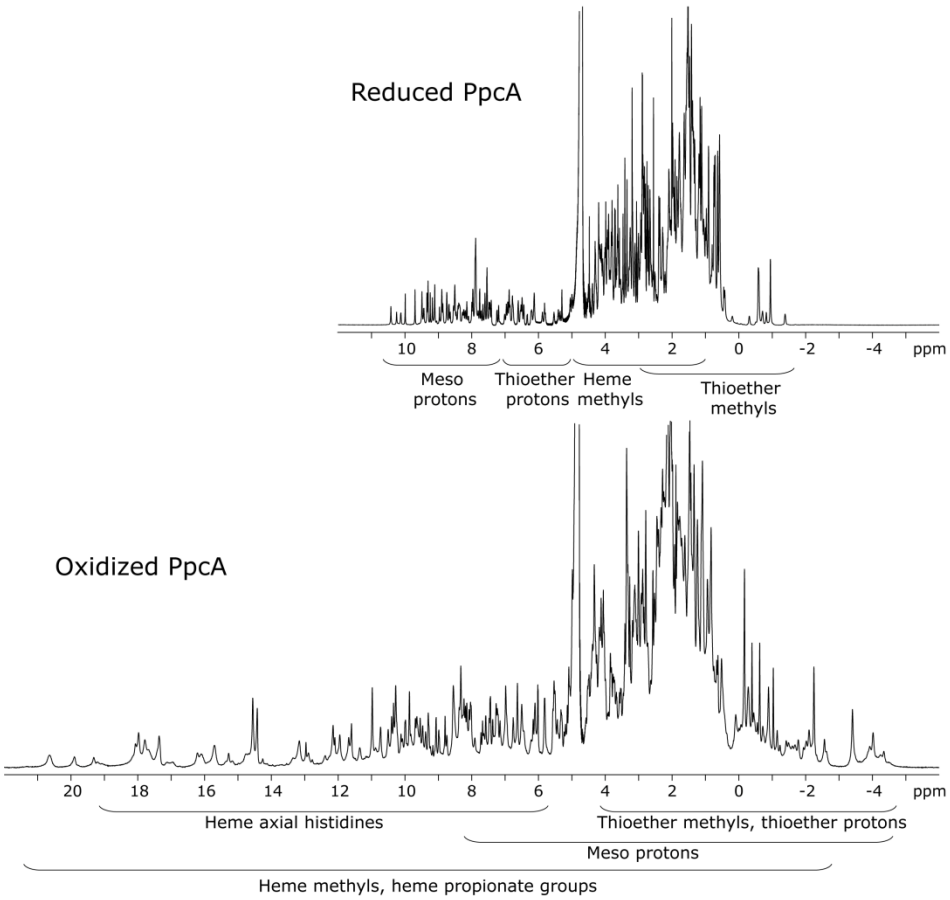

Figure 1.4 – 1D-^{1}H NMR spectra of reduced and oxidized triheme cytochrome PpcA obtained at 25 ºC. The typical regions of the heme substituents are indicated.

Indeed, in the oxidized form, the paramagnetic effect of the iron unpaired electrons, causes the spread of the signals of the heme cofactors (Figure 1.4), as well as those of the amino acid residues located in their neighborhoods, all over large NMR spectral widths [61]. Additionally, these resonances are generally broader, which makes the complete assignment of the heme and polypeptide resonances a laborious and very time consuming task.

On the other hand, for diamagnetic multiheme proteins, as it is the case of the reduced PpcA, the assignment of the heme substituents is facilitated since they are dominated by the porphyrin ring-current shifts and, therefore, appear in well defined regions of the ^{1}H NMR spectra (Figure 1.4). The only exception is observed for the heme propionate protons as they are structurally more variable.

An efficient expression system to produce multiheme *c*-type cytochromes, using *Escherichia coli* (*E. coli*) as host, was recently described and successfully applied to the expression of multiheme cytochromes containing up to 12 heme groups [62,63]. This was overcome by using a *lac* promoter in the expression plasmid and co-expressing the cytochrome *c* maturation gene cluster on a separate plasmid [63].

This system was also used to achieve cost-effective labeling of multiheme cytochromes using an experimental labeling methodology that is based on two major aspects: (i) use of a two-step culture growth procedure, where cell growth in rich media was followed by transfer

to minimal media containing ^{15}N-labeled ammonium chloride, and (ii) incorporation of the heme precursor δ-aminolevulinic acid in minimal culture media [64].

1.6 Thesis outline

In order to contribute to the studies of the electron transfer chains of *G. sulfurreducens*, the work developed on this thesis focused on the study of the periplasmic triheme cytochrome family, with special emphasis on PpcA, the most abundant in *G. sulfurreducens*.

The thermodynamic characterization of cytochromes PpcA, PpcB, PpcD and PpcE by NMR and UV-visible spectroscopy is described on Chapter 3. Chapter 4 is dedicated to structural studies of PpcA in solution. The assignment of the resonances of the protein and its co-factors is described, and the solution structure in the reduced state is presented. The physiological role of key amino acids in PpcA is discussed in Chapter 5. Finally, on Chapter 6, ongoing studies are presented.

1.7 References

[1] DR Lovley (1993) Dissimilatory metal reduction, Annu Rev Microbiol 47, 263-290.

[2] JR Lloyd, DR Lovley (2001) Microbial detoxification of metals and radionuclides, Curr Opin Biotechnol 12, 248-253.

[3] DR Lovley (2003) Cleaning up with genomics: applying molecular biology to bioremediation, Nat Rev Microbiol 1, 35-44.

[4] DE Holmes, KT Finneran, RA O'Neil, DR Lovley (2002) Enrichment of members of the family *Geobacteraceae* associated with stimulation of dissimilatory metal reduction in uranium-contaminated aquifer sediments, Appl Environ Microbiol 68, 2300-2306.

[5] RT Anderson, HA Vrionis, I Ortiz-Bernad, CT Resch, PE Long, R Dayvault, K Karp, S Marutzky, DR Metzler, A Peacock, DC White, M Lowe, DR Lovley (2003) Stimulating the *in situ* activity of *Geobacter* species to remove uranium from the groundwater of a uranium-contaminated aquifer, Appl Environ Microbiol 69, 5884-5891.

[6] KB Gregory, DR Lovley (2005) Remediation and recovery of uranium from contaminated subsurface environments with electrodes, Environ Sci Technol 39, 8943-8947.

[7] JN Rooney-Varga, RT Anderson, JL Fraga, D Ringelberg, DR Lovley (1999) Microbial communities associated with anaerobic benzene degradation in a petroleum-contaminated aquifer, Appl Environ Microbiol 65, 3056-3063.

[8] DR Bond, DR Lovley (2003) Electricity production by *Geobacter sulfurreducens* attached to electrodes, Appl Environ Microbiol 69, 1548-1555.

[9] DR Lovley (2006) Bug juice: harvesting electricity with microorganisms, Nat Rev Microbiol 4, 497-508.

[10] AE Franks, KP Nevin (2010) Microbial Fuel Cells, A Current Review, Energies 3, 899-919.

[11] DE Holmes, DR Bond, RA O'Neil, CE Reimers, LR Tender, DR Lovley (2004) Microbial communities associated with electrodes harvesting electricity from a variety of aquatic sediments, Microb Ecol 48, 178-190.

[12] F Caccavo, Jr., DJ Lonergan, DR Lovley, M Davis, JF Stolz, MJ McInerney (1994) *Geobacter sulfurreducens* sp. nov., a hydrogen- and acetate-oxidizing dissimilatory metal-reducing microorganism, Appl Environ Microbiol 60, 3752-3759.

[13] BA Methé, KE Nelson, JA Eisen, IT Paulsen, W Nelson, JF Heidelberg, D Wu, M Wu, N Ward, MJ Beanan, RJ Dodson, R Madupu, LM Brinkac, SC Daugherty, RT DeBoy, AS Durkin, M Gwinn, JF Kolonay, SA Sullivan, DH Haft, J Selengut, TM Davidsen, N Zafar, O White, B Tran, C Romero, HA Forberger, J Weidman, H Khouri, TV Feldblyum, TR Utterback, SE Van Aken, DR Lovley, CM Fraser (2003) Genome of *Geobacter sulfurreducens*: metal reduction in subsurface environments, Science 302, 1967-1969.

[14] SH Thomas, RD Wagner, AK Arakaki, J Skolnick, JR Kirby, LJ Shimkets, RA Sanford, FE Loffler (2008) The mosaic genome of *Anaeromyxobacter dehalogenans* strain 2CP-C suggests an aerobic common ancestor to the delta-proteobacteria, PLoS One 3, e2103.

[15] MV Coppi, C Leang, SJ Sandler, DR Lovley (2001) Development of a genetic system for *Geobacter sulfurreducens*, Appl Environ Microbiol 67, 3180-3187.

[16] G Reguera, KD McCarthy, T Mehta, JS Nicoll, MT Tuominen, DR Lovley (2005) Extracellular electron transfer via microbial nanowires, Nature 435, 1098-1101.

[17] KA Weber, LA Achenbach, JD Coates (2006) Microorganisms pumping iron: anaerobic microbial iron oxidation and reduction, Nat Rev Microbiol 4, 752-764.

[18] T Mehta, MV Coppi, SE Childers, DR Lovley (2005) Outer membrane *c*-type cytochromes required for Fe(III) and Mn(IV) oxide reduction in *Geobacter sulfurreducens*, Appl Environ Microbiol 71, 8634-8641.

[19] YH Ding, KK Hixson, MA Aklujkar, MS Lipton, RD Smith, DR Lovley, T Mester (2008) Proteome of *Geobacter sulfurreducens* grown with Fe(III) oxide or Fe(III) citrate as the electron acceptor, Biochim Biophys Acta 1784, 1935-1941.

[20] ES Shelobolina, MV Coppi, AA Korenevsky, LN Didonato, SA Sullivan, H Konishi, H Xu, C Leang, JE Butler, BC Kim, DR Lovley (2007) Importance of *c*-type cytochromes for U(VI) reduction by *Geobacter sulfurreducens*, BMC Microbiol 7, 16.

[21] BC Kim, DR Lovley (2008) Investigation of direct *vs.* indirect involvement of the *c*-type cytochrome MacA in Fe(III) reduction by *Geobacter sulfurreducens*, FEMS Microbiol Lett.

[22] JR Lloyd, C Leang, AL Hodges Myerson, MV Coppi, S Cuifo, B Methe, SJ Sandler, DR Lovley (2003) Biochemical and genetic characterization of PpcA, a periplasmic *c*-type cytochrome in *Geobacter sulfurreducens*, Biochem J 369, 153-161.

[23] DE Holmes, SK Chaudhuri, KP Nevin, T Mehta, BA Methe, A Liu, JE Ward, TL Woodard, J Webster, DR Lovley (2006) Microarray and genetic analysis of electron transfer to electrodes in *Geobacter sulfurreducens*, Environ Microbiol 8, 1805-1815.

[24] YH Ding, KK Hixson, CS Giometti, A Stanley, A Esteve-Núñez, T Khare, SL Tollaksen, W Zhu, JN Adkins, MS Lipton, RD Smith, T Mester, DR Lovley (2006) The proteome of dissimilatory metal-reducing microorganism *Geobacter sulfurreducens* under various growth conditions, Biochim Biophys Acta 1764, 1198-1206.

[25] KP Nevin, BC Kim, RH Glaven, JP Johnson, TL Woodard, BA Methe, RJ Didonato, SF Covalla, AE Franks, A Liu, DR Lovley (2009) Anode biofilm transcriptomics reveals outer surface components essential for high density current production in *Geobacter sulfurreducens* fuel cells, PLoS One 4, e5628.

[26] PL Tremblay, ZM Summers, RH Glaven, KP Nevin, K Zengler, CL Barrett, Y Qiu, BO Palsson, DR Lovley (2011) A *c*-type cytochrome and a transcriptional regulator responsible for enhanced extracellular electron transfer in *Geobacter sulfurreducens* revealed by adaptive evolution, Environ Microbiol 13, 13-23.

[27] BC Kim, C Leang, YH Ding, RH Glaven, MV Coppi, DR Lovley (2005) OmcF, a putative *c*-type monoheme outer membrane cytochrome required for the expression of other outer membrane cytochromes in *Geobacter sulfurreducens*, J Bacteriol 187, 4505-4513.

[28] BC Kim, BL Postier, RJ Didonato, SK Chaudhuri, KP Nevin, DR Lovley (2008) Insights into genes involved in electricity generation in *Geobacter sulfurreducens* via whole genome microarray analysis of the OmcF-deficient mutant, Bioelectrochemistry 73, 70-75.

[29] C Leang, X Qian, T Mester, DR Lovley (2010) Alignment of the *c*-type cytochrome OmcS along pili of *Geobacter sulfurreducens*, Appl Environ Microbiol 76, 4080-4084.

[30] C Leang, MV Coppi, DR Lovley (2003) OmcB, a *c*-type polyheme cytochrome, involved in Fe(III) reduction in *Geobacter sulfurreducens*, J Bacteriol 185, 2096-2103.

[31] BC Kim, X Qian, C Leang, MV Coppi, DR Lovley (2006) Two putative *c*-type multiheme cytochromes required for the expression of OmcB, an outer membrane protein essential for optimal Fe(III) reduction in *Geobacter sulfurreducens*, J Bacteriol 188, 3138-3142.

[32] JW Voordeckers, BC Kim, M Izallalen, DR Lovley (2010) Role of *Geobacter sulfurreducens* outer surface *c*-type cytochromes in reduction of soil humic acid and anthraquinone-2,6-disulfonate, Appl Environ Microbiol 76, 2371-2375.

[33] DR Lovley (2008) Extracellular electron transfer: wires, capacitors, iron lungs, and more, Geobiology 6, 225-231.

[34] G Reguera, RB Pollina, JS Nicoll, DR Lovley (2007) Possible nonconductive role of *Geobacter sulfurreducens* pilus nanowires in biofilm formation, J Bacteriol 189, 2125-2127.

[35] A Esteve-Núñez, J Sosnik, P Visconti, DR Lovley (2008) Fluorescent properties of *c*-type cytochromes reveal their potential role as an extracytoplasmic electron sink in *Geobacter sulfurreducens*, Environ Microbiol 10, 497-505.

[36] X Qian, T Mester, L Morgado, T Arakawa, ML Sharma, K Inoue, C Joseph, CA Salgueiro, MJ Maroney, DR Lovley (2011) Biochemical characterization of purified OmcS, a *c*-type cytochrome required for insoluble Fe(III) reduction in *Geobacter sulfurreducens*, Biochim Biophys Acta 1807, 404-412.

[37] PR Pokkuluri, YY Londer, SJ Wood, NE Duke, L Morgado, CA Salgueiro, M Schiffer (2009) Outer membrane cytochrome *c*, OmcF, from *Geobacter sulfurreducens*: high structural similarity to an algal cytochrome c_6, Proteins 74, 266-270.

[38] K Inoue, X Qian, L Morgado, BC Kim, T Mester, M Izallalen, CA Salgueiro, DR Lovley (2010) Purification and characterization of OmcZ, an outer-surface, octaheme *c*-type cytochrome essential for optimal current production by *Geobacter sulfurreducens*, Appl Environ Microbiol 76, 3999-4007.

[39] RS Hartshorne, M Kern, B Meyer, TA Clarke, M Karas, DJ Richardson, J Simon (2007) A dedicated haem lyase is required for the maturation of a novel bacterial cytochrome *c* with unconventional covalent haem binding, Mol Microbiol 64, 1049-1060.

[40] PR Pokkuluri, YY Londer, NE Duke, WC Long, M Schiffer (2004) Family of cytochrome c_7-type proteins from *Geobacter sulfurreducens*: structure of one cytochrome c_7 at 1.45 Å resolution, Biochemistry 43, 849-859.

[41] SF Altschul, TL Madden, AA Schaffer, J Zhang, Z Zhang, W Miller, DJ Lipman (1997) Gapped BLAST and PSI-BLAST: a new generation of protein database search programs, Nucleic Acids Res 25, 3389-3402.

[42] PR Pokkuluri, YY Londer, X Yang, NE Duke, J Erickson, V Orshonsky, G Johnson, M Schiffer (2010) Structural characterization of a family of cytochromes c_7 involved in Fe(III) respiration by *Geobacter sulfurreducens*, Biochim Biophys Acta 1797, 222-232.

[43] L Morgado, M Bruix, V Orshonsky, YY Londer, NE Duke, X Yang, PR Pokkuluri, M Schiffer, CA Salgueiro (2008) Structural insights into the modulation of the redox properties of two *Geobacter sulfurreducens* homologous triheme cytochromes, Biochim Biophys Acta 1777, 1157-1165.

[44] IB Coutinho, DL Turner, MY Liu, J LeGall, AV Xavier (1996) Structure of the three-haem core of cytochrome $c_{551.5}$ determined by ^{1}H NMR, J Biol Inorg Chem 1, 305-311.

[45] M Czjzek, P Arnoux, R Haser, W Shepard (2001) Structure of cytochrome c_7 from *Desulfuromonas acetoxidans* at 1.9 Å resolution, Acta Crystallogr D Biol Crystallogr 57, 670-678.

[46] M Assfalg, L Banci, I Bertini, M Bruschi, MT Giudici-Orticoni, P Turano (1999) A proton-NMR investigation of the fully reduced cytochrome c_7 from *Desulfuromonas acetoxidans*. Comparison between the reduced and the oxidized forms, Eur J Biochem 266, 634-643.

[47] M Assfalg, L Banci, I Bertini, M Bruschi, P Turano (1998) 800 MHz ^{1}H NMR solution structure refinement of oxidized cytochrome c_7 from *Desulfuromonas acetoxidans*, Eur J Biochem 256, 261-270.

[48] M Pessanha, L Morgado, RO Louro, YY Londer, PR Pokkuluri, M Schiffer, CA Salgueiro (2006) Thermodynamic characterization of triheme cytochrome PpcA from *Geobacter sulfurreducens*: evidence for a role played in e^-/H^+ energy transduction, Biochemistry 45, 13910-13917.

[49] R Mahadevan, DR Bond, JE Butler, A Esteve-Núñez, MV Coppi, BO Palsson, CH Schilling, DR Lovley (2006) Characterization of metabolism in the Fe(III)-reducing organism *Geobacter sulfurreducens* by constraint-based modeling, Appl Environ Microbiol 72, 1558-1568.

[50] IJ Correia, CM Paquete, RO Louro, T Catarino, DL Turner, AV Xavier (2002) Thermodynamic and kinetic characterization of trihaem cytochrome c_3 from *Desulfuromonas acetoxidans*, Eur J Biochem 269, 5722-5730.

[51] A Brige, JA Cole, WR Hagen, Y Guisez, JJ Van Beeumen (2001) Overproduction, purification and novel redox properties of the dihaem cytochrome *c*, NapB, from *Haemophilus influenzae*, Biochem J 356, 851-858.

[52] PN da Costa, C Conte, LM Saraiva (2000) Expression of a *Desulfovibrio* tetraheme cytochrome *c* in *Escherichia coli*, Biochem Biophys Res Commun 268, 688-691.

[53] ML Herbaud, C Aubert, MC Durand, F Guerlesquin, L Thöny-Meyer, A Dolla (2000) *Escherichia coli* is able to produce heterologous tetraheme cytochrome c_3 when the *ccm* genes are co-expressed, Biochim Biophys Acta 1481, 18-24.

[54] L Brennan, DL Turner, AC Messias, ML Teodoro, J LeGall, H Santos, AV Xavier (2000) Structural basis for the network of functional cooperativities in cytochrome c_3 from *Desulfovibrio gigas*: solution structures of the oxidised and reduced states, J Mol Biol 298, 61-82.

[55] AC Messias, AP Aguiar, L Brennan, CA Salgueiro, LM Saraiva, AV Xavier, DL Turner (2006) Solution structures of tetrahaem ferricytochrome c_3 from *Desulfovibrio vulgaris* (Hildenborough) and its K45Q mutant: the molecular basis of cooperativity, Biochim Biophys Acta 1757, 143-153.

[56] AC Messias, DH Kastrau, HS Costa, J LeGall, DL Turner, H Santos, AV Xavier (1998) Solution structure of *Desulfovibrio vulgaris* (Hildenborough) ferrocytochrome c_3: structural basis for functional cooperativity, J Mol Biol 281, 719-739.

[57] VB Paixão, CA Salgueiro, L Brennan, GA Reid, SK Chapman, DL Turner (2008) The solution structure of a tetraheme cytochrome from *Shewanella frigidimarina* reveals a novel family structural motif, Biochemistry 47, 11973-11980.

[58] VB Paixão, H Vis, DL Turner (2010) Redox linked conformational changes in cytochrome c_3 from *Desulfovibrio desulfuricans* ATCC 27774, Biochemistry 49, 9620-9629.

[59] E Harada, Y Fukuoka, T Ohmura, A Fukunishi, G Kawai, T Fujiwara, H Akutsu (2002) Redox-coupled conformational alternations in cytochrome c_3 from *D. vulgaris* Miyazaki F on the basis of its reduced solution structure, J Mol Biol 319, 767-778.

[60] CG Mowat, SK Chapman (2005) Multi-heme cytochromes - new structures, new chemistry, Dalton Trans 3381-3389.

[61] K Wüthrich, NMR of Proteins and Nucleic Acids, John Wiley and Sons, New York, 1986.

[62] YY Londer, PR Pokkuluri, V Orshonsky, L Orshonsky, M Schiffer (2006) Heterologous expression of dodecaheme "nanowire" cytochromes *c* from *Geobacter sulfurreducens*, Protein Expr Purif 47, 241-248.

[63] YY Londer, PR Pokkuluri, DM Tiede, M Schiffer (2002) Production and preliminary characterization of a recombinant triheme cytochrome c_7 from *Geobacter sulfurreducens* in *Escherichia coli*, Biochim Biophys Acta 1554, 202-211.

[64] AP Fernandes, I Couto, L Morgado, YY Londer, CA Salgueiro (2008) Isotopic labeling of *c*-type multiheme cytochromes overexpressed in *E. coli*, Prot Expr Purif 59, 182-188.

Experimental Procedures

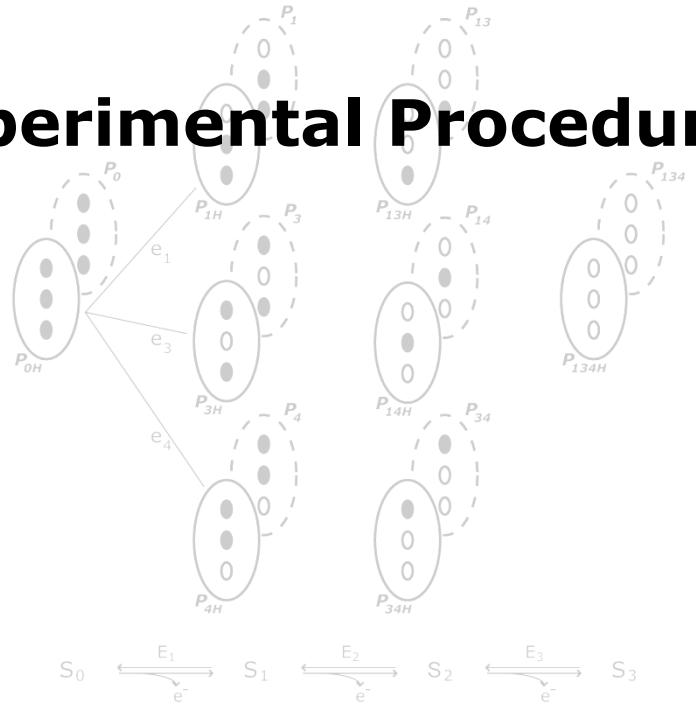

2. EXPERIMENTAL PROCEDURES

2.1 Protein expression and purification

2.1.1 Plasmids

All the molecular biology experiments were done by the collaborative group from the Argonne National Laboratory, Argonne, Illinois, USA.

The DNA sequence for mature PpcA was previously cloned in plasmid pCK32, a pUC derivative containing the *lac* promoter and the OmpA leader sequence [1]. Vector pVA203 [2], a pCK32 derivative, was used to clone PpcB, PpcD and PpcE mature sequences [3,4]. Plasmid pEC86 that contains the cytochrome *c* maturation gene cluster *ccmABCDEFGH* [5], was a kind gift from Dr. Thöny-Meyer (Zürich, Switzerland). The QuikChange Site-Directed Mutagenesis kit (Stratagene) was used to prepare the PpcA mutants.

2.1.2 Heterologous expression

Competents cells of *E. coli* strain BL21 (DE3) containing plasmid pEC86 were transformed with each of the plasmids, and grown overnight at 37 °C in 2xYT solid medium [6] supplemented with 34 μg/mL of chloramphenicol (CLO, for pEC86 selection) and 100 μg/mL of ampicillin (AMP, for expression plasmid selection). Isolated colonies were used for growth in liquid media for protein overexpression.

2.1.2.1 Unlabeled proteins

Cells were aerobically grown at 30 °C up to an OD_{600} of 1.5–1.8 at a shaking speed of 200 rpm in 2xYT medium supplemented with CLO and AMP in the same concentration. At this point, protein expression was induced with isopropyl β-D-1-thiogalactopyranoside (IPTG) at a final concentration of 10 μM for PpcA, PpcB and PpcD, and 200 μM for PpcE, and cultures allowed to grow overnight at 30 °C at a shaking speed of 180 rpm [1,7].

2.1.2.2 ^{15}N labeled proteins

The protocol for isotopic labeling of multiheme cytochromes was developed in our laboratory [8], and the initial steps of growth were the same as for unlabeled samples. However, after reaching an OD_{600} of 1.5–1.8, cells were harvested and washed twice, by centrifuge/resuspension cycles, with 250 mL per liter of culture of a salt solution containing 240 mM Na_2HPO_4, 110 mM KH_2PO_4 and 43 mM NaCl [8]. Cells were resuspended in minimal medium (in a ratio of 250 mL of minimal medium for each liter of 2xYT medium) containing 48 mM Na_2HPO_4, 22 mM KH_2PO_4 and 8.6 mM NaCl, 20 mg/L biotin, 2 mM $MgSO_4.7H_2O$, 0.1 mM $CaCl_2$, 5 μM $MnCl_2.4H_2O$, 10 μM $FeSO_4.7H_2O$, 20 mg/L vitamin B_1, 1 mM of the heme precursor δ-aminolevulinic acid, and 1 g/L $^{15}NH_4Cl$ and 4 g/L glucose as nitrogen and carbon sources, respectively [8].

Cells were incubated at 37 °C for 1h at 200 rpm for recovery and clearance of unlabeled metabolites [9]. After 1h, protein expression was induced with 0.8 mM IPTG and cells were allowed to grow overnight at 30 °C and 180 rpm [8].

2.1.3 Protein purification

Proteins were purified as previously described [1,8,10]. Cultures were harvested by centrifugation at 6400 *g* for 20 min and resuspended in 30 mL of lysis buffer (100 mM Tris-HCl, pH 8.0, 0.5 mM EDTA, 20% sucrose) per liter of cell culture, containing 0.5 mg/mL lysozyme. The cell suspension was incubated at room temperature for 15 min; 30 mL of cold water were added and incubated on ice for 15 min with gentle shaking. The supernatant constituting the periplasmic fraction was recovered by centrifugation at 15000 *g* at 4 °C for 20 min. The periplasmic fraction was ultracentrifugated at 150000 *g* for 90 min at 4 °C to remove any precipitate and dialyzed twice against 10 mM Tris-HCl (pH 8.5). The supernatant was loaled onto two 5 mL Econo-Pac HighS cartridges (BioRad) connected together and equilibrated with 10 mM Tris-HCl (pH 8.5), and eluted with a NaCl gradient (0-300 mM) in 10 mM Tris-HCl (pH 8.5). Red colored fractions were pooled together and concentrated to 1 mL for injection into a XK 16/70 column (GE Healthcare) packed with Superdex^{TM} 75 (GE Healthcare) previously equilibrated with 100 mM sodium phosphate pH 8.1. Protein was eluted at a flow rate of 1 mL/min. Protein purity was evaluated by Coomassie stained SDS-PAGE.

Purified proteins were concentrated and the buffer was exchanged to 20 mM NaCl by ultrafiltration methods. Protein concentration was determined with the absorbance of the α-band of the reduced forms using the specific absorption coefficient of 97.5 $mM^{-1}cm^{-1}$ determined for PpcA [11,12].

2.2 NMR spectroscopy

2.2.1 Sample preparation

For NMR studies the proteins were lyophilized twice with D_2O (99% atom) and then resuspended in the final buffer for each experiment. 1D-^{1}H NMR spectra were recorded before and after protein lyophilization to check proteins' integrity. The pH of the samples was adjusted by the addition of small amounts of NaOD or DCl and checked with a glass micro electrode. The pH values were not corrected for isotope effects. Protein samples for solution structure determination were prepared with 0.04% sodium azide to avoid bacterial growth.

2.2.1.1 Oxidized samples

Oxidized 70 μM samples of PpcA PpcB and PpcD were prepared in 80mM phosphate buffer with NaCl (final ionic strength of 250mM) in 99% D_2O. Oxidized 0.4 mM samples of

^{15}N labeled PpcA were prepared in 45 mM phosphate buffer with NaCl (final ionic strength of 100mM) in 92% H_2O/8% D_2O.

2.2.1.2 Reduced samples

For heme core solution structure studies, 140 μM samples of PpcA, PpcB, PpcD and PpcE were prepared in 80mM phosphate buffer with NaCl (final ionic strength of 250mM) in 99% D_2O [4,7].

For the determination of PpcA solution structure, samples were prepared in 45 mM sodium phosphate buffer (100 mM ionic strength) pH 7.1 [13]. ^{15}N labeled samples were prepared in 92% H_2O/8% D_2O and unlabeled samples prepared in 92% H_2O/8% D_2O or in 99% D_2O. Final protein concentration was about 1 mM.

In order to avoid oxidation of the samples, the NMR tubes were sealed with a gas-tight serum cap and the air was flushed out form the sample. The samples were reduced directly in the NMR tube with gaseous hydrogen in the presence of catalytic amounts of hydrogenase from *Desulfovibrio vulgaris* (Hildenborough), as previously described [4,7].

2.2.1.3 Samples for redox titrations

For NMR redox titrations, proteins were prepared in a concentration of 70 μM in 80mM phosphate buffer with NaCl (final ionic strength of 250mM) in 99% D_2O and reduced as described in the previous section. Partially oxidized samples were obtained by first removing the hydrogen from the reduced sample with nitrogen and then adding controlled amounts of air into the NMR tube [4,7].

2.2.2 NMR Experiments

NMR experiments were acquired on a Bruker Avance 600 MHz spectrometer available at Faculdade de Ciências e Tecnologia, Universidade Nova de Lisboa, on a Bruker Avance 800 MHz spectrometer available at Instituto de Química-Física "Rocasolano", Consejo Superior de Investigaciones Científicas (Madrid, Spain), both equipped with triple-resonance cryoprobes, or on a Bruker DRX-500 spectrometer equipped with a 5 mm inverse detection probe head with internal B_0 gradient coils available at Instituto de Tecnologia Química e Biológica (Oeiras, Portugal). Proton chemical shifts were calibrated using the water signal as internal reference, and nitrogen and carbon chemical shifts were calibrated through indirect referencing [14]. Spectra were processed using TOPSPIN (BrukerBiospin, Karlsruhe, Germany) and analyzed with Sparky [15].

2.2.2.1 Heme core structure in the reduced state

A series of 2D-NOESY (Nuclear Overhauser Effect SpectroscopY) with 50 and 100 ms mixing-time, TOCSY (TOtal Correlation SpectroscopY) with 45 ms mixing time, and COSY (COrrelation SpectroscopY) NMR spectra were acquired on fully reduced unlabeled samples in

D_2O at 15 °C to assist the heme proton resonance assignments. The spectra were recorded with a spectral width of 14 parts per million (ppm) and 128 scans per increment.

2.2.2.2 Redox titrations

The oxidation patterns of the heme groups of PpcA, PpcB, PpcD, PpcE and PpcA mutants were monitored by 2D-^{1}H-EXSY (EXchange SpectroscopY) on a Bruker AV-800 spectrometer [7]. For each pH value, a series of experiments with the sample poised at several degrees of oxidation were acquired to unambiguously map the oxidation of the individual hemes throughout the redox titrations. All the spectra were acquired at 15 °C with a mixing time of 25 ms and a sweep width of 40 ppm (for PpcA and its mutants, PpcB and PpcE) or 50 ppm (for PpcD), with 256 scans per increment.

2.2.2.3 Structural studies

For structural studies, spectra were acquired at 25 °C with different PpcA samples in the reduced state. The following set of experiments was acquired: ^{15}N labeled sample: 2D-^{1}H-^{15}N Heteronuclear Single Quantum Correlation (HSQC), 3D-^{1}H-^{15}N-TOCSY (60 ms) and 3D-^{1}H-^{15}N-NOESY (80 ms); unlabeled sample in 92% H_2O/8% D_2O: 2D-^{1}H-COSY, 2D-^{1}H-TOCSY (60 ms) and 2D-^{1}H-NOESY (50 ms); unlabeled sample in D_2O: 2D-^{1}H-COSY, 2D-^{1}H-TOCSY (45 ms) and 2D-^{1}H-NOESY (100 ms) [13]. Spectra were acquired with a sweep width of 14 ppm and 80 ppm (2D) or 40 ppm (3D) in proton and nitrogen dimensions, respectively. 1D-^{1}H NMR spectra were obtained before and after each multidimensional spectrum to confirm protein integrity and fully reduction.

2.2.3 Assignment strategy and methodology

2.2.3.1 Assignment of heme signals in the reduced state

The studied cytochromes have three hemes with bis-His axial coordination. Each heme includes several proton-containing groups: four methyl groups, four meso protons, two thioether protons, two thioether methyl and two propionate groups (Figure 2.1); which must be unambiguously identified and assigned.

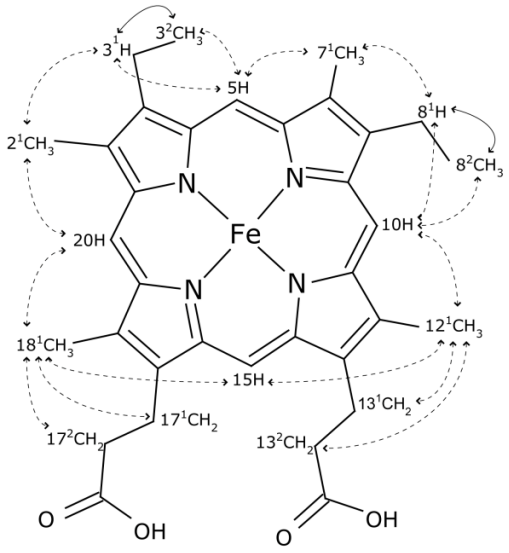

Figure 2.1 – Diagram of heme *c* numbered according to the IUPAC-IUB nomenclature [16]. Dashed lines indicate the connectivities observed in NOESY spectra and solid lines the connectivities observed in TOCSY spectra.

In the reduced state, these proteins are diamagnetic (S = 0) and the assignment of the heme substituents is facilitated since they are dominated by the porphyrin ring-current shifts and, therefore, appear in well defined regions of the NMR spectra (Figure 1.4 – Chapter 1). These are 11 to 7 ppm for meso protons 5H, 10H, 15H, and 20H; 7 to 5 ppm for protons 3^1H and 8^1H; 5 to 1 ppm for heme methyls 2^1CH_3, 7^1CH_3, 12^1CH_3, and 18^1CH_3; and 3 to −1.5 ppm for thioether methyls 3^2CH_3 and 8^2CH_3 [17-25]. The only exception is observed for the heme propionate protons as they are structurally more variable.

The heme proton resonances in the reduced form were identified for all the proteins by following the assignment strategy for heme protons described by Keller and Wüthrich [26] for the horse heart ferrocytochrome, and applied later to multiheme ferrocytochromes by Turner *et al.* [27]. Briefly, 2D-TOCSY spectra allow the identification of the thioether pairs 3^1H and 3^2CH_3, and 8^2CH_3 and 8^1H. In the NOESY spectra with shorter mixing time, characteristic patterns can be observed: H20 protons are connected to two methyl groups, H15 protons are not connected to any methyl or thioether groups, and H10 and H5 which are connected to one methyl group and one thioether pair. This last ambiguity is overcome by analyzing connectivities between 2^1CH_3 and 3^1H, and between 7^1CH_3 and 8^1H. H15 protons are identified by connectivities to the methyl groups 12^1CH_3, and 18^1CH_3 at longer mixing times. The specific assignment of the individual hemes within the structure is made by observing the interheme connectivities in longer mixing time NOESY spectra [27].

2.2.3.2 Ring-current shifts calculation

The heme substituent chemical shifts were calculated by correcting the heme proton reference shifts (9.36 ppm for heme meso protons, 6.13 ppm for heme thioether methines, 3.48 ppm for heme methyls, and 2.12 ppm for heme thioether methyls) with the ring current

shifts calculated from the crystal structures, following the procedure described by Turner *et al.* [27] and Messias *et al.* [22].

2.2.3.3 Identification of heme oxidation profiles

In a triheme cytochrome, three consecutive reversible steps of one-electron transfer convert the fully reduced state (stage 0, S_0) in the fully oxidized state (stage 3, S_3), and therefore four different redox stages can be defined. At each stage, microstates are grouped with the same number of oxidized hemes (Figure 2.2). Additionally, within each microstate, the group responsible for the redox-Bohr effect may be protonated or deprotonated, leading to a total of 16 microstates.

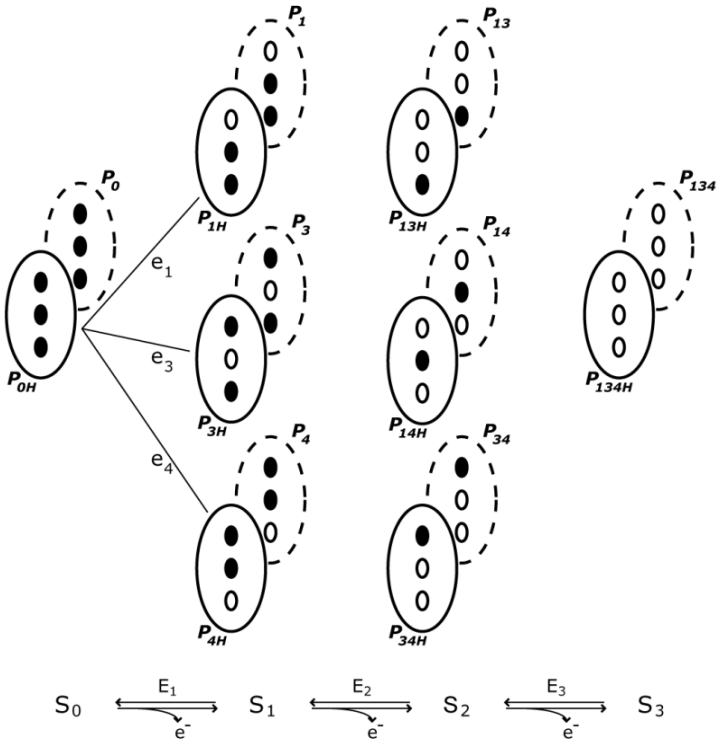

Figure 2.2 – Electronic distribution scheme for a triheme cytochrome with a proton-linked equilibrium, showing the 16 possible microstates. The three inner circles represent the hemes, which can be reduced (black) or oxidized (white). The outer circles with solid and dashed lines represent the protonated and deprotonated microstates, respectively. The microstates are grouped according to the number of oxidized hemes in four oxidation stages (S_{0-3}) connected by one electron step. E_S (S = 1–3) is the macroscopic reduction potential, *i.e.*, the solution potential at which the sum of the microstate populations in stage S equals the sum of the populations in stage S_{-1}. P_{0H} and P_0 represent the reduced protonated and deprotonated microstates, respectively. P_{ijkH} and P_{ijk} indicate the protonated and deprotonated microstates, respectively, where *i*, *j*, and *k* represent the heme(s) that are oxidized in that particular microstate. As an example, the transitions between the fully reduced protonated and the corresponding protonated microstate in oxidation stage S_1 are indicated with the corresponding microscopic reduction potentials.

When the interconversion between microstates within the same oxidation stage (intramolecular electron exchange) is fast on the NMR time scale and the interconversion between microstates belonging to different oxidation stages (intermolecular electron

exchange) is slow, the individual heme NMR signals can be discriminated [28,29]. Under these conditions, the distribution of paramagnetic shifts observed for each oxidation stage is governed by the relative microscopic reduction potentials of the heme groups, and thus provides information on the relative order of oxidation of the hemes. The substituents of each heme have different chemical shifts in the four macroscopic oxidation stages, and since these paramagnetic shifts are proportional to the degree of oxidation of that particular heme group, they can be used to monitor the oxidation of each heme throughout a redox titration. As the reoxidation of a multiheme protein proceeds, the heme methyl signals become much shifted from the diamagnetic region of the spectra. Thus, these are the most adequate heme substituents to monitor a reoxidation. This data can be obtained from 2D-EXSY NMR redox titrations by following the positions of the heme methyl signals from their position in the fully reduced protein to its final position in the fully oxidized protein (Figure 3.3 – Chapter 3) [28].

2.2.3.4 Assignment of protein backbone and side chain signals

After assigning the heme resonance signals, protein backbone and side chain resonances were assigned following conventional strategies [30].

For ^{15}N labeled proteins the starting point is the 2D-^{1}H-^{15}N-HSQC spectrum. This spectrum is a fingerprint of the protein and shows correlations between the amide proton (HN) and the nitrogen (N) for the backbone and side chains amide groups.

For ^{15}N labeled proteins, the 3D-^{1}H-^{15}N-TOCSY is used to identify the spin systems according to the pattern of the proton resonances observed for each HN strip (Figure 2.3), and sort them into classes of amino acids. Each cross-peak will represent a through-bond spin-spin coupling connectivity.

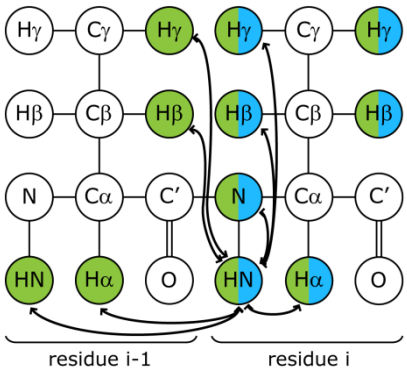

Figure 2.3 – Connectivities observed in tridimensional spectra for ^{15}N labeled proteins. 3D-^{1}H-^{15}N-TOCSY connectivities are represented in blue and 3D-^{1}H-^{15}N-NOESY connectivities in green.

The 3D-^{1}H-^{15}N-NOESY is then used for sequential assignment by identifying the connectivities between the HN^{i} and the protons in residue i-1 (Figure 2.3), since NOE cross-peaks originate from short through-space distances. The assignment is subsequently transposed to the 2D spectra and the side chain protons specifically assigned using the 2D-^{1}H-COSY and 2D-^{1}H-TOCSY spectra.

2.2.4 ^{15}N relaxation measurements

A series of ^{1}H-^{15}N HSQC spectra were measured at 800 MHz and at 600 MHz to obtain the ^{15}N longitudinal (T_1) and transverse (T_2) relaxation times in the same conditions used for structure calculations. For the determination of the longitudinal relaxation rate, a set of eight experiments was acquired with relaxation delays from 5 to 1200 ms, and for the transverse relaxation rate, eight experiments were recorded with relaxation delays between 16 to 130 ms. The intensities of the individual cross-peaks at each experiment were fitted to Equation 2.1 in order to obtain the values for the relaxation times (T) [31].

$$\mathrm{I} = \mathrm{I}_0 \mathrm{e}^{-\mathrm{t}/T} \qquad \textbf{Equation 2.1}$$

Heteronuclear ^{15}N{^{1}H}NOE measurements provide information about the motion of individual N-H bond vectors and were determined from the ratio of the intensities of the cross-peaks obtained for HSQC experiments with and without saturation of proton magnetization (Equation 2.2) [31].

$$\mathrm{NOE} = \frac{\mathrm{I}_{\mathrm{sat}}}{\mathrm{I}_{\mathrm{unsat}}} \qquad \textbf{Equation 2.2}$$

Experiments were acquired with a recycling delay of 5 s.

The data from the different spectra were treated as peak heights.

2.2.5 pH titrations

1D-^{1}H NMR spectra with a spectral width of 50 ppm were used to monitor the pH dependence of heme methyl substituents of PpcA, PpcB and PpcD in the fully oxidized state at 15 °C [4].

For PpcA, the effect of pH titration on the amide chemical shifts was determined by analyzing a series of 2D-^{1}H-^{15}N-HSQC spectra acquired in the pH range 5.5 to 9.5 in the reduced state. For studies in the reduced state, the pH was adjusted inside an anaerobic chamber (MBraun LABstar) to avoid sample oxidation. The average chemical shift differences ($\Delta\delta_{avg}$) of each backbone and side chain amide were calculated as

$$\Delta\delta_{\mathrm{average}} = \sqrt{\frac{\Delta\delta^2\mathrm{N}}{25} + \Delta\delta^2\mathrm{H}}{2} \qquad \textbf{Equation 2.3}$$

where $\Delta\delta$H and $\Delta\delta$N are the differences in the ^{1}H and ^{15}N chemical shifts, respectively [32].

2.3 Redox titrations followed by UV-visible spectroscopy

Redox titrations of the cytochromes using 18 μM protein solutions in 80 mM phosphate buffer (pH 7 and 8) with NaCl (250 mM final ionic strength) were performed inside an anaerobic chamber at 15 °C, as previously described [4,7], with redox mediators at a final concentration of 2 μM. The redox mediators were chosen according to the procedures defined in the literature [33]. A mixture of methylene blue, gallocyanine, indigo tetrasulfonate, indigo trisulfonate, indigo disulfonate, anthraquinone-2,7-disulfonate, 2-hydroxy-1,4-naphthoquinone, anthraquinone-2-sulfonate, safranine O, diquat, benzyl viologen, neutral red and methyl viologen was used in all the experiments. To check for hysteresis, each redox titration was performed in both oxidative and reductive directions, using sodium dithionite as the reductant, and potassium ferricyanide as the oxidant. The solution potentials were measured using a combined Pt/Ag/AgCl electrode, calibrated with the quinhydrone couple. UV-visible spectra were recorded in a Shimadzu UV-1203 spectrophotometer. The reduced fraction of the proteins was determined by integrating the area of the α-peak above the line connecting the flanking isosbestic points (to subtract the optical contribution of the redox mediators), as described by Paquete and co-workers [34] (Figure 3.4 – Chapter 3). The experiments were performed at least two times, and the reduction potentials (relative to SHE) were found to be reproducible within ±5 mV.

2.4 Thermodynamic model

The general theoretical framework that allows the thermodynamic properties of the redox centers in multiheme proteins to be studied in detail was previously described [35]. The thermodynamic model accounts for the pH dependence of the chemical shifts of the heme methyl groups during a reoxidation process monitored by NMR, and also for the pH dependence of the redox titrations followed by UV-visible spectroscopy.

The energies of the microstates described in Figure 2.2 may be expressed as the sums of terms for each center and the interactions between them [35]. Thus, three reduction potentials and one pK_a plus six two-center interaction energies (three heme-heme and three redox-Bohr) are sufficient to characterize the system across the full range of pH values and solution potentials, independently of any structural model. The total reduced heme in each triheme cytochrome, or the fractional oxidation of any heme at any stage of oxidation, is therefore a function of 10 energy parameters.

To obtain information about each microstate, it is necessary to monitor at different pH values the stepwise oxidation of each individual heme, which for the particular case of heme groups displaying identical optical properties can be obtained with confidence by NMR spectroscopy [28,29].

Since the intrinsic paramagnetic shifts of the heme methyls are proportional to the oxidation fraction of that particular heme, *m*, they can be used to obtain the relative microscopic reduction potentials of the hemes in each stage of oxidation *S*. However, this is

only valid if the extrinsic paramagnetic shifts, *i.e.* the contribution of the paramagnetic interactions with the other heme groups in the molecule, are negligible [29].

For each pH, the paramagnetic shifts of one methyl group of each heme in oxidation stages 1–2 relative to the fully oxidized form give the averaged oxidation fraction for each heme in each stage (Equation 2.4) [35].

$$\sum_{m=1}^{3} \frac{(\delta_{obs}^{m,S} - \delta_{obs}^{m,0})}{(\delta_{obs}^{m,3} - \delta_{obs}^{m,0})} = S \qquad \textbf{Equation 2.4}$$

The fact that each oxidation step involves a single electron means that the relative shifts of any two methyl groups determine that of the third according to Equation 2.4, and therefore there is redundancy when data for all three hemes are collected.

The observed chemical shift $\delta_{obs}^{m,S}$ depends on the populations of the microstates in which that heme is oxidized, averaged according to the populations of the protonated ($\sum P_H^{m,S}$) and deprotonated ($\sum P^{m,S}$) forms

$$\delta_{obs}^{m,S} = \frac{(\delta^{m,3} - \delta^{m,0}) \sum P^{m,S} + (\delta_H^{m,3} - \delta^{m,0}) \sum P_H^{m,S}}{\sum P^S} + \delta^{m,0} \qquad \textbf{Equation 2.5}$$

where $\delta^{m,0}$ is the observed chemical shift of methyl *m* in the fully reduced protein and $\delta^{m,3}$ and $\delta_H^{m,3}$ are those observed in the fully oxidized deprotonated and protonated protein, respectively. The chemical shift of the heme methyl in the fully reduced form is assumed to be independent of pH.

This equation can be used to simulate the pH dependence of the chemical shifts of the methyl groups in different redox stages.

However, NMR data only defines the relative heme reduction potentials and heme redox interactions. To determine the absolute potentials, the total reduced protein fractions need to be measured using redox titrations followed by UV-visible spectroscopy [35].

Taking as a reference the fully reduced and deprotonated state S_0, the energies for each microstate (G) in oxidations stages S_1, S_2 and S_3 can be determined according to the following equations:

S_1 $$G_i = g_i - E \qquad \textbf{Equation 2.6}$$

S_2 $$G_{ij} = g_i + g_j + g_{ij} - 2E \qquad \textbf{Equation 2.7}$$

S_3 $$G_{ijk} = g_i + g_j + g_k + g_{ij} + g_{ik} + g_{jk} - 3E \qquad \textbf{Equation 2.8}$$

where g_i, g_j and g_k are energies proportional to the individual heme redox potentials and g_{ij}, g_{ik} and g_{jk} are two-site redox interaction energies.

For the protonated microstates the ionization energy of the fully reduced protein g_H, which is related to the pK_a of the reference state through $pK_a = g_H F/[(\ln 10)RT]$, and the interactions between the oxidized hemes and the protonatable group have to be considered.

S_1 $$G_{iH} = G_i + g_H + g_{iH} - (\ln 10)\frac{RT}{F}pH$$ **Equation 2.9**

S_2 $$G_{ijH} = G_{ij} + g_H + g_{iH} + g_{jH} - (\ln 10)\frac{RT}{F}pH$$ **Equation 2.10**

S_3 $$G_{ijH} = G_{ij} + g_H + g_{iH} + g_{jH} + g_{kH} - (\ln 10)\frac{RT}{F}pH$$ **Equation 2.11**

The populations of each microstate can then be determined from Equation 2.12 [35].

$$P = e^{-GF/(RT)}$$ **Equation 2.12**

The total reduced fraction as a function of the solution potential for each pH value can be obtained from the relative populations weighted by the number of reduced hemes (Equation 2.13).

$$\text{reduced fraction} = \frac{3\sum P_0 + 2\sum P_i + \sum P_{ij}}{4\sum P^S}$$ **Equation 2.13**

The chemical shifts obtained from redox titrations followed by NMR and the reduced fractions obtained from UV-visible spectroscopy redox titrations for the different cytochromes were fitted simultaneously with the thermodynamic model. The experimental uncertainty of the NMR data was evaluated from the line width of each NMR signal at half height, and the UV-visible data points were given an uncertainty of 3% of the total optical signal.

2.5 NMR structure determination

2.5.1 Determination of restraints

For structure determination, the cross-peaks assigned in the 2D-^{1}H-NOESY spectra were integrated, since the intensity of the NOE cross-peaks is related to the distance between the two interacting spins.

Using the software Sparky, a Gaussian function was used for the integration of isolated peaks and sum data in a box surrounding the peak for overlapped ones. Cross-peaks due to protons separated by fixed distances and all intra-heme cross-peaks, except those involving the propionate groups, were not included.

Volumes for integrated cross-peaks were converted into volume restraints and used as input for the program PARADYANA [36]. Initial structures were calculated with a preliminary set of NOE data and the resulting conformers were then analyzed and used to assign additional peaks in the NOESY spectra. In the final stages of structure refinement, the calculated structures were checked for short (less than 2.5 Å) distances between assigned protons that should give rise to significant NOEs.

Non-standard residues were used for structure calculations: fast-flipping aromatic residues with pseudo-atoms to limit the orientations of the planes [22], proline residues with fixed upper limit distances for ring closure and flexible heme groups [36]. A set of 69 fixed upper limit distances (upl) associated with this type of residues was used as input for PARADYANA for calculations in the reduced state.

The program GLOMSA [37] was used for stereospecific assignment during the process of structure calculation.

2.5.2 Structure calculation and analysis

Structure calculation was performed with the program PARADYANA, a version of DYANA that takes peak volumes as input [36].

In each calculation 200 conformers were determined, from which the 10 structures with lowest target function value were selected for further analysis. In the final calculation, the 20 conformers with lowest target function value were selected. The software CHIMERA [38] was used for visual analysis during preliminary calculations and the software MOLMOL [39] was used for superimposition and identification of elements of secondary structure in the final set of conformers. Quality of the structures was analyzed with PROCHECK-NMR [40].

2.6 References

[1] YY Londer, PR Pokkuluri, DM Tiede, M Schiffer (2002) Production and preliminary characterization of a recombinant triheme cytochrome c_7 from *Geobacter sulfurreducens* in *Escherichia coli*, Biochim Biophys Acta 1554, 202-211.

[2] PR Pokkuluri, YY Londer, NE Duke, J Erickson, M Pessanha, CA Salgueiro, et al. (2004) Structure of a novel c_7-type three-heme cytochrome domain from a multidomain cytochrome *c* polymer, Protein Sci 13, 1684-1692.

[3] PR Pokkuluri, YY Londer, X Yang, NE Duke, J Erickson, V Orshonsky, et al. (2010) Structural characterization of a family of cytochromes c_7 involved in Fe(III) respiration by *Geobacter sulfurreducens*, Biochim Biophys Acta 1797, 222-232.

[4] L Morgado, M Bruix, V Orshonsky, YY Londer, NE Duke, X Yang, et al. (2008) Structural insights into the modulation of the redox properties of two *Geobacter sulfurreducens* homologous triheme cytochromes, Biochim Biophys Acta 1777, 1157-1165.

[5] E Arslan, H Schulz, R Zufferey, P Kunzler, L Thöny-Meyer (1998) Overproduction of the *Bradyrhizobium japonicum c*-type cytochrome subunits of the cbb_3 oxidase in *Escherichia coli*, Biochem Biophys Res Commun 251, 744-747.

[6] J Sambrook, DW Russell, Molecular Cloning: a laboratory manual, Cold Spring Harbor Laboratory Press, New York, 2001.

[7] L Morgado, M Bruix, M Pessanha, YY Londer, CA Salgueiro (2010) Thermodynamic characterization of a triheme cytochrome family from *Geobacter sulfurreducens* reveals mechanistic and functional diversity, Biophys J 99, 293-301.

[8] AP Fernandes, I Couto, L Morgado, YY Londer, CA Salgueiro (2008) Isotopic labeling of *c*-type multiheme cytochromes overexpressed in *E. coli*, Prot Expr Purif 59, 182-188.

[9] J Marley, M Lu, C Bracken (2001) A method for efficient isotopic labeling of recombinant proteins, J Biomol NMR 20, 71-75.

[10] PR Pokkuluri, YY Londer, NE Duke, WC Long, M Schiffer (2004) Family of cytochrome c_7-type proteins from *Geobacter sulfurreducens*: structure of one cytochrome c_7 at 1.45 Å resolution, Biochemistry 43, 849-859.

[11] M Pessanha, L Morgado, RO Louro, YY Londer, PR Pokkuluri, M Schiffer, et al. (2006) Thermodynamic characterization of triheme cytochrome PpcA from *Geobacter sulfurreducens*: evidence for a role played in e^-/H^+ energy transduction, Biochemistry 45, 13910-13917.

[12] S Seeliger, R Cord-Ruwisch, B Schink (1998) A periplasmic and extracellular *c*-type cytochrome of *Geobacter sulfurreducens* acts as a ferric iron reductase and as an electron carrier to other acceptors or to partner bacteria, J Bacteriol 180, 3686-3691.

[13] L Morgado, VB Paixao, M Schiffer, PR Pokkuluri, M Bruix, CA Salgueiro (2012) Revealing the structural origin of the redox-Bohr effect: the first solution structure of a cytochrome from *Geobacter sulfurreducens*, Biochem J 441, 179-187.

[14] DS Wishart, CG Bigam, J Yao, F Abildgaard, HJ Dyson, E Oldfield, et al. (1995) ^1H, ^{13}C and ^{15}N chemical shift referencing in biomolecular NMR, J Biomol NMR 6, 135-140.

[15] TD Goddard, DG Kneller, Sparky 3.114, University of California, San Francisco, USA, 2007.

[16] GP Moss (1988) Nomenclature of tetrapyrroles. Recommendations 1986 IUPAC-IUB Joint Commission on Biochemical Nomenclature (JCBN), Eur J Biochem 178, 277-328.

[17] M Pessanha, YY Londer, WC Long, J Erickson, PR Pokkuluri, M Schiffer, et al. (2004) Redox characterization of *Geobacter sulfurreducens* cytochrome c_7: physiological relevance of the conserved residue F15 probed by site-specific mutagenesis, Biochemistry 43, 9909-9917.

[18] IB Coutinho, DL Turner, J LeGall, AV Xavier (1993) Characterization of the structure and redox behaviour of cytochrome c_3 from *Desulfovibrio baculatus* by ^{1}H-nuclear-magnetic-resonance spectroscopy, Biochem J 294, 899-908.

[19] E Harada, Y Fukuoka, T Ohmura, A Fukunishi, G Kawai, T Fujiwara, et al. (2002) Redox-coupled conformational alternations in cytochrome c_3 from *D. vulgaris* Miyazaki F on the basis of its reduced solution structure, J Mol Biol 319, 767-778.

[20] E Harada, J Kumagai, K Ozawa, S Imabayashi, AS Tsapin, KH Nealson, et al. (2002) A directional electron transfer regulator based on heme-chain architecture in the small tetraheme cytochrome *c* from *Shewanella oneidensis*, FEBS Lett 532, 333-337.

[21] RO Louro, I Pacheco, DL Turner, J LeGall, AV Xavier (1996) Structural and functional characterization of cytochrome c_3 from *D. desulfuricans* ATCC 27774 by ^{1}H-NMR, FEBS Lett 390, 59-62.

[22] AC Messias, DH Kastrau, HS Costa, J LeGall, DL Turner, H Santos, et al. (1998) Solution structure of *Desulfovibrio vulgaris* (Hildenborough) ferrocytochrome c_3: structural basis for functional cooperativity, J Mol Biol 281, 719-739.

[23] PM Pereira, I Pacheco, DL Turner, RO Louro (2002) Structure-function relationship in type II cytochrome c_3 from *Desulfovibrio africanus*: a novel function in a familiar heme core, J Biol Inorg Chem 7, 815-822.

[24] M Pessanha, L Brennan, AV Xavier, PM Cuthbertson, GA Reid, SK Chapman, et al. (2001) NMR structure of the haem core of a novel tetrahaem cytochrome isolated from *Shewanella frigidimarina*: identification of the haem-specific axial ligands and order of oxidation, FEBS Lett 489, 8-13.

[25] MA Piçarra-Pereira, DL Turner, J LeGall, AV Xavier (1993) Structural studies on *Desulfovibrio gigas* cytochrome c_3 by two-dimensional ^{1}H-nuclear-magnetic-resonance spectroscopy, Biochem J 294, 909-915.

[26] RM Keller, K Wüthrich (1978) Assignment of the heme *c* resonances in the 360 MHz H NMR spectra of cytochrome *c*, Biochim Biophys Acta 533, 195-208.

[27] DL Turner, CA Salgueiro, J LeGall, AV Xavier (1992) Structural studies of *Desulfovibrio vulgaris* ferrocytochrome c_3 by two-dimensional NMR, Eur J Biochem 210, 931-936.

[28] CA Salgueiro, DL Turner, H Santos, J LeGall, AV Xavier (1992) Assignment of the redox potentials to the four haems in *Desulfovibrio vulgaris* cytochrome c_3 by 2D-NMR, FEBS Lett 314, 155-158.

[29] H Santos, JJ Moura, I Moura, J LeGall, AV Xavier (1984) NMR studies of electron transfer mechanisms in a protein with interacting redox centres: *Desulfovibrio gigas* cytochrome c_3, Eur J Biochem 141, 283-296.

[30] J Cavanagh, WJ Fairbrother, AG Palmer, III, M Rance, NJ Skelton, Protein NMR Spectroscopy: Principles and Practice, Elsevier Academic Press, 2007.

[31] Q Teng, Structural Biology: Practical NMR Applications Springer Science + Business Media Inc, New York, USA, 2005.

[32] DS Garrett, YJ Seok, A Peterkofsky, GM Clore, AM Gronenborn (1997) Identification by NMR of the binding surface for the histidine-containing phosphocarrier protein HPr on the N-terminal domain of enzyme I of the *Escherichia coli* phosphotransferase system, Biochemistry 36, 4393-4398.

[33] PL Dutton (1978) Redox potentiometry: determination of midpoint potentials of oxidation-reduction components of biological electron-transfer systems, Methods Enzymol 54, 411-435.

[34] CM Paquete, DL Turner, RO Louro, AV Xavier, T Catarino (2007) Thermodynamic and kinetic characterisation of individual haems in multicentre cytochromes c_3, Biochim Biophys Acta 1767, 1169-1179.

[35] DL Turner, CA Salgueiro, T Catarino, J LeGall, AV Xavier (1996) NMR studies of cooperativity in the tetrahaem cytochrome c_3 from *Desulfovibrio vulgaris*, Eur J Biochem 241, 723-731.

[36] DL Turner, L Brennan, SG Chamberlin, RO Louro, AV Xavier (1998) Determination of solution structures of paramagnetic proteins by NMR, Eur Biophys J 27, 367-375.

[37] P Güntert, W Braun, K Wüthrich (1991) Efficient computation of three-dimensional protein structures in solution from nuclear magnetic resonance data using the program DIANA and the supporting programs CALIBA, HABAS and GLOMSA, J Mol Biol 217, 517-530.

[38] EF Pettersen, TD Goddard, CC Huang, GS Couch, DM Greenblatt, EC Meng, et al. (2004) UCSF Chimera - a visualization system for exploratory research and analysis, J Comput Chem 25, 1605-1612.

[39] R Koradi, M Billeter, K Wüthrich (1996) MOLMOL: a program for display and analysis of macromolecular structures, J Mol Graph 14, 51-55, 29-32.

[40] RA Laskowski, JA Rullmannn, MW MacArthur, R Kaptein, JM Thornton (1996) AQUA and PROCHECK-NMR: programs for checking the quality of protein structures solved by NMR, J Biomol NMR 8, 477-486.

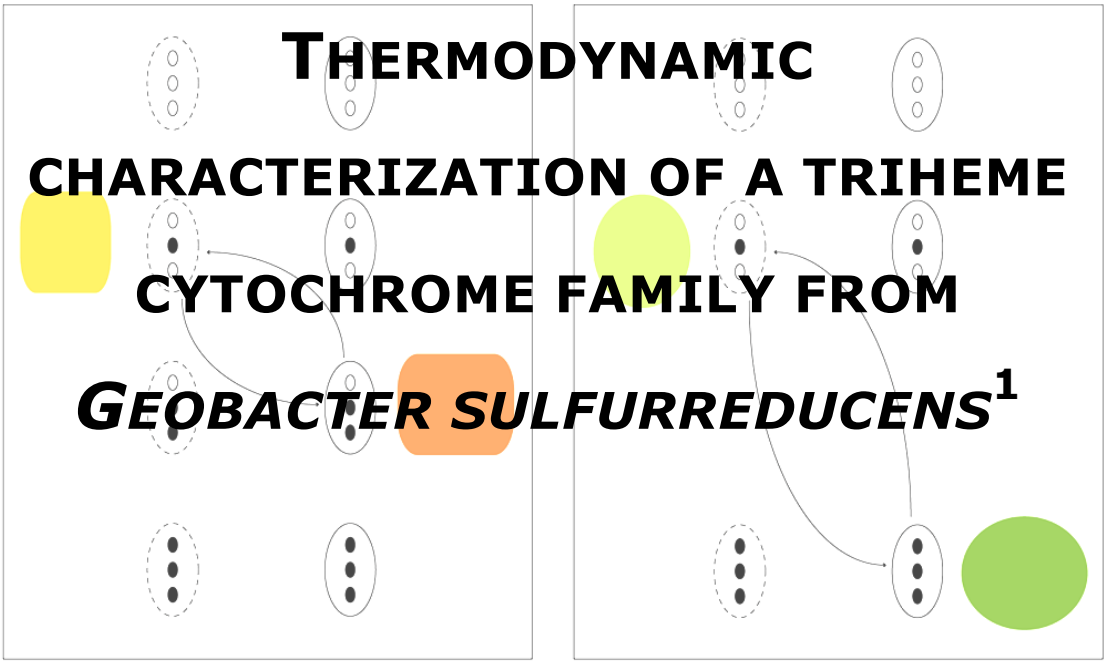

THERMODYNAMIC CHARACTERIZATION OF A TRIHEME CYTOCHROME FAMILY FROM *GEOBACTER SULFURREDUCENS*[1]

[1] Partially reproduced from L Morgado, M Bruix, V Orshonsky, YY Londer, NE Duke, X Yang, PR Pokkuluri, M Schiffer, CA Salgueiro (2008) Structural insights into the modulation of the redox properties of two *Geobacter sulfurreducens* homologous triheme cytochromes, Biochim Biophys Acta 1777, 1157-1165 (http://dx.doi.org/10.1016/j.bbabio.2008.04.043) and L Morgado, M Bruix, M Pessanha, YY Londer, CA Salgueiro (2010) Thermodynamic characterization of a triheme cytochrome family from *Geobacter sulfurreducens* reveals mechanistic and functional diversity, Biophys J 99, 293-301 (http://dx.doi.org/10.1016/j.bpj.2010.04.017), according to the Editors' Copyright Policy.

3. THERMODYNAMIC CHARACTERIZATION OF A TRIHEME CYTOCHROME FAMILY FROM *GEOBACTER SULFURREDUCENS*

A family of five periplasmic triheme cytochromes (PpcA-E) was identified in *Geobacter sulfurreducens*, where they play a crucial role by driving electron transfer from the cytoplasm to the cell exterior and assisting the reduction of extracellular acceptors.

The detailed thermodynamic characterization of PpcA, PpcB, PpcD, and PpcE under optimal experimental conditions was carried out. For PpcC, two different conformations were detected during the protein redox cycle, preventing its thermodynamic characterization.

The heme reduction potentials of PpcA, PpcB, PpcD, and PpcE are negative, differ from each other, and cover different functional ranges. These reduction potentials are strongly modulated by heme-heme interactions and by interactions with protonated groups (the redox-Bohr effect) establishing different cooperative networks for each protein, which indicates that they are designed to perform different functions in the cell. PpcA and PpcD appear to be optimized to interact with specific redox partners involving e^-/H^+ transfer via different mechanisms. Although no evidence of preferential electron transfer pathway or e^-/H^+ coupling was found for PpcB and PpcE, the difference in their working potential ranges suggests that they may also have different physiological redox partners. This is the first study to characterize homologous cytochromes from the same microorganism and provide evidence of their different mechanistic and functional properties.

3.1 Results

3.1.1 Assignment of the heme signals in the reduced form

The PpcA, PpcB, PpcD and PpcE heme proton resonances in the reduced form were identified by following the assignment strategy for heme protons in multiheme ferrocytochromes described by Turner *et al.* [1] and are indicated in Table A.1 in the Appendix.

As expected from the conserved heme disposition observed in all cytochromes (Figure 1.3 – Chapter 1) [2], the same type of heme I and IV substituents, which are more exposed to the solvent (2^1CH_3, 18^1CH_3, and 20H), display similar chemical shifts. On the other hand, the chemical shifts of heme III substituents are more spread due to the contribution of the ring current shifts of neighboring porphyrin rings. In fact, several heme III resonances (namely, those of $20H^{III}$, $2^1CH_3{}^{III}$, $7^1CH_3{}^{III}$, $18^1CH_3{}^{III}$, 3^1H^{III}, and $8^2CH_3{}^{III}$) are shifted downfield.

The heme proton assignments were assessed by comparing the observed heme proton chemical shifts with those calculated from the crystal structures. The shifts correlate quite well, even for the protons subject to the larger ring current effects (Figure 3.1).

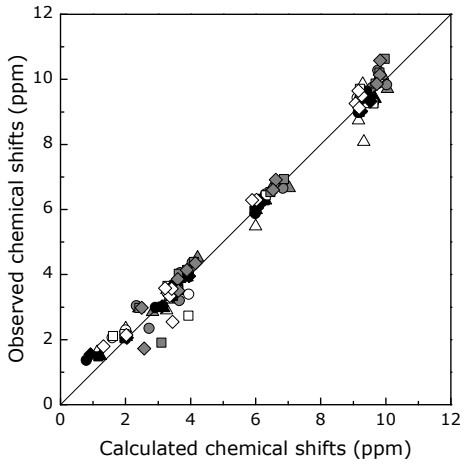

Figure 3.1 – Comparison between calculated and observed chemical shifts for the heme substituents in the reduced forms of PpcA (◇), PpcB (□), PpcD (△) and PpcE (○). White, gray and black symbols correspond to hemes I, III and IV, respectively. The solid line has a unit slope.

The assignment of the heme protons was further confirmed by the observation of the interheme connectivities in the NOESY NMR spectra for closest substituents (≤3.5 Å).

The correlation between the measured heme proton chemical shifts for the four cytochromes is indicated in Figure 3.2.

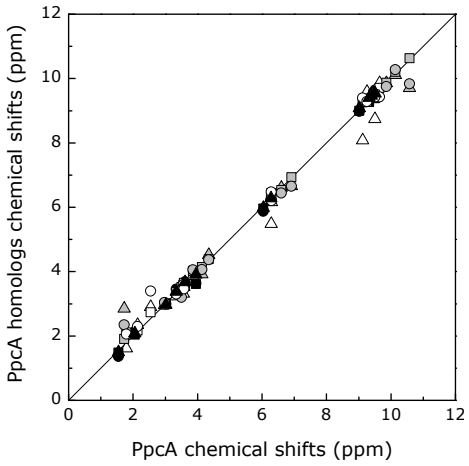

Figure 3.2 – Comparison between the observed heme proton chemical shifts of reduced PpcB (□), PpcD (△) and PpcE (○) with those of PpcA. White, gray and black symbols correspond to hemes I, III and IV, respectively. The solid line has a unit slope. The rmsd between the heme proton chemical shifts measured for PpcA and those of PpcB, PpcD and PpcE are 0.11, 0.37 and 0.26 ppm, respectively.

3.1.2 Thermodynamic characterization

The thermodynamic properties of PpcA were determined in an earlier study using NMR data obtained at 500 MHz and relatively high ionic strength (500 mM) to slow down the intermolecular electron exchange between the different oxidation stages [3]. These experimental conditions were identical to the ones used to characterize the triheme cytochrome isolated from *D. acetoxidans*, the only cytochrome c_7 reported in the literature at that time [4], and allowed a proper and detailed comparison of the redox properties of these two cytochromes [3]. Despite these particular conditions, signal broadness was observed for the connectivities between the heme methyl signals in the different oxidation stages. As expected from the structural similarities among the triheme cytochromes, comparable problems were found for the PpcA homologs. To overcome these difficulties, two-dimensional exchange spectroscopy (2D-EXSY) NMR spectra were acquired at 800 MHz to favor a slow intermolecular exchange regime on the NMR timescale. At this magnetic field, it was also possible to lower the ionic strength of the samples to match the physiological ionic strength recommended by the American Type Culture Collection (ATCC) for growth of *G. sulfurreducens* [5]. Under these experimental conditions, well-resolved 2D-EXSY NMR spectra were obtained for PpcA, PpcB, PpcD, and PpcE, and discrete NMR signals connecting the different oxidation stages were observed for each heme methyl. The only exception was found for PpcC, which presents different conformations at intermediate stages of oxidation. This leads to splitting and excessive broadening of the NMR signals, preventing the thermodynamic characterization of this protein [6].

The heme methyl groups $12^1CH_3^I$, $7^1CH_3^{III}$, and $12^1CH_3^{IV}$ (PpcA and PpcB); $18^1CH_3^I$, $7^1CH_3^{III}$, and $18^1CH_3^{IV}$ (PpcD); and $18^1CH_3^I$, $12^1CH_3^{III}$, and $12^1CH_3^{IV}$ (PpcE) were used to monitor the stepwise oxidation of each heme at each pH. As an example, the stepwise oxidation of the PpcA, PpcB, PpcD, and PpcE heme groups followed by 2D-EXSY NMR is illustrated in Figure 3.3.

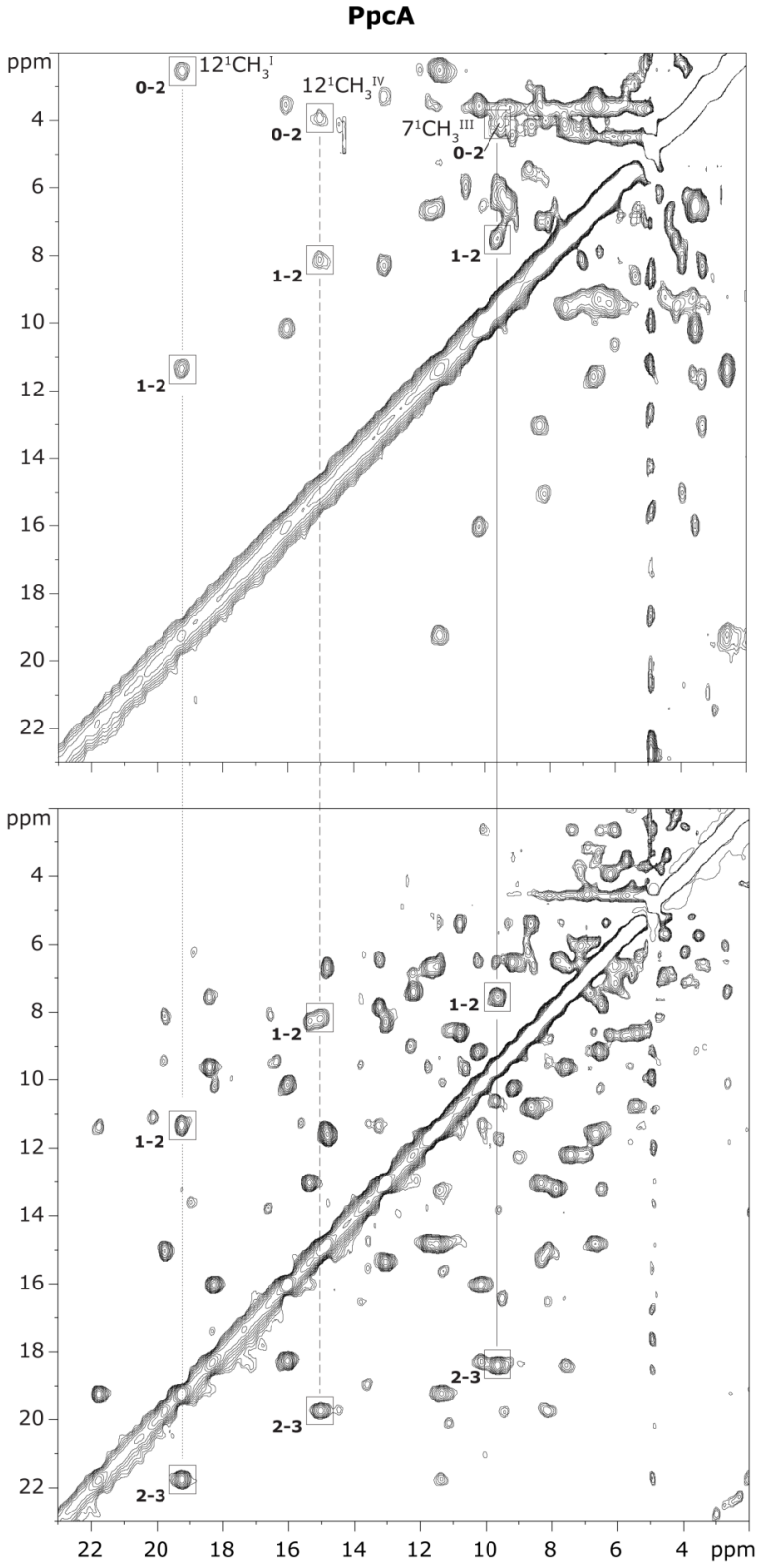

Figure 3.3 – Expansions of 2D-EXSY NMR spectra obtained at 15 °C and pH 8 for PpcA, PpcB, PpcE and PpcD at different degrees of oxidation. Cross-peaks resulting from intermolecular electron transfer between the different stages are indicated for the selected heme methyls of each heme: heme I (dotted lines), heme III (solid lines) and heme IV (dashed lines). The Roman and Arabic numbers indicate the hemes and the oxidation stages, respectively. In some experiments, when heme methyl connectivities were already well defined in F_2 dimension, less than 256 increments were acquired. In such cases, the heme methyl connectivities show a broader component in F_1 dimension.

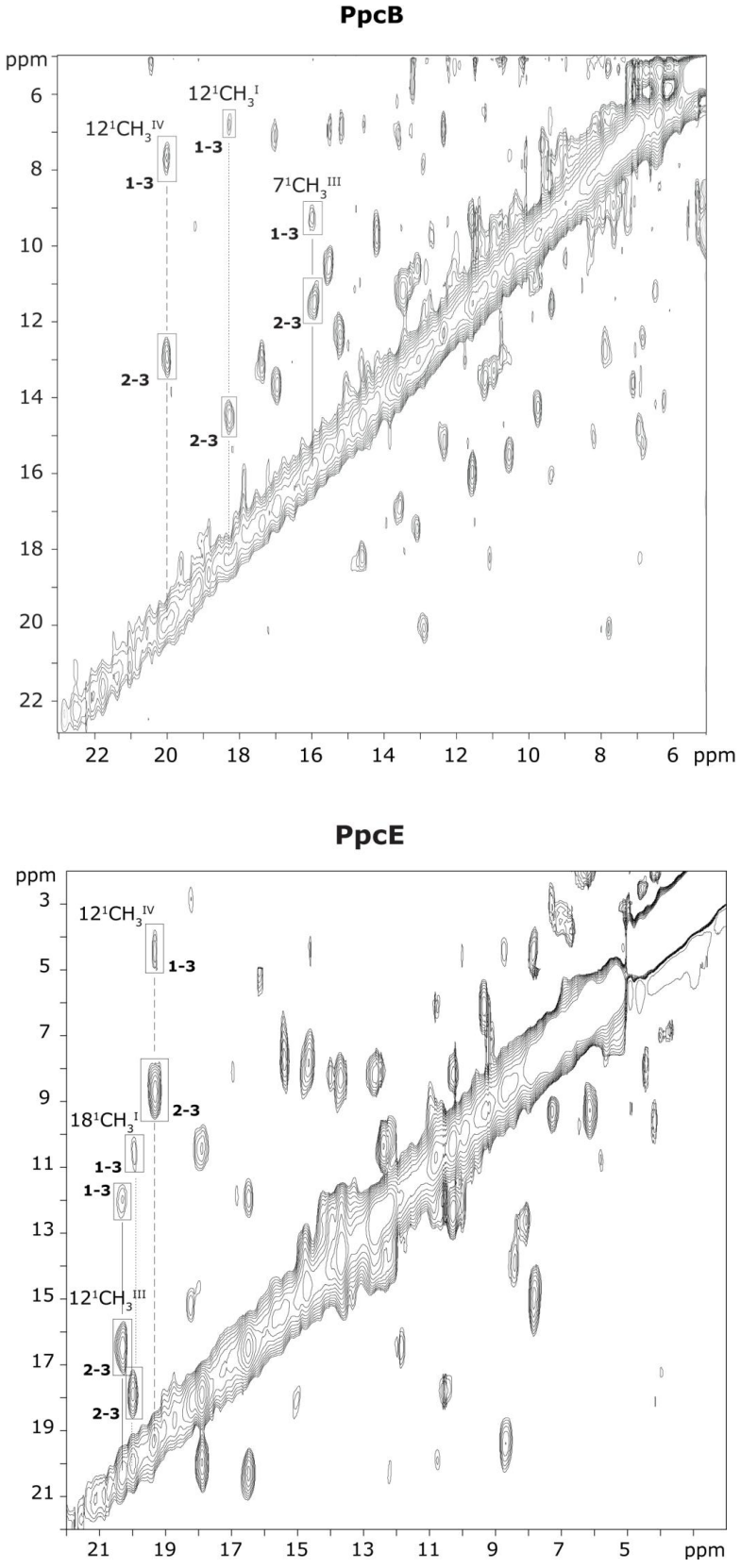

Figure 3.3 (cont) – Expansions of 2D-EXSY NMR spectra obtained at 15 °C and pH 8 for PpcA, PpcB, PpcE and PpcD at different degrees of oxidation.

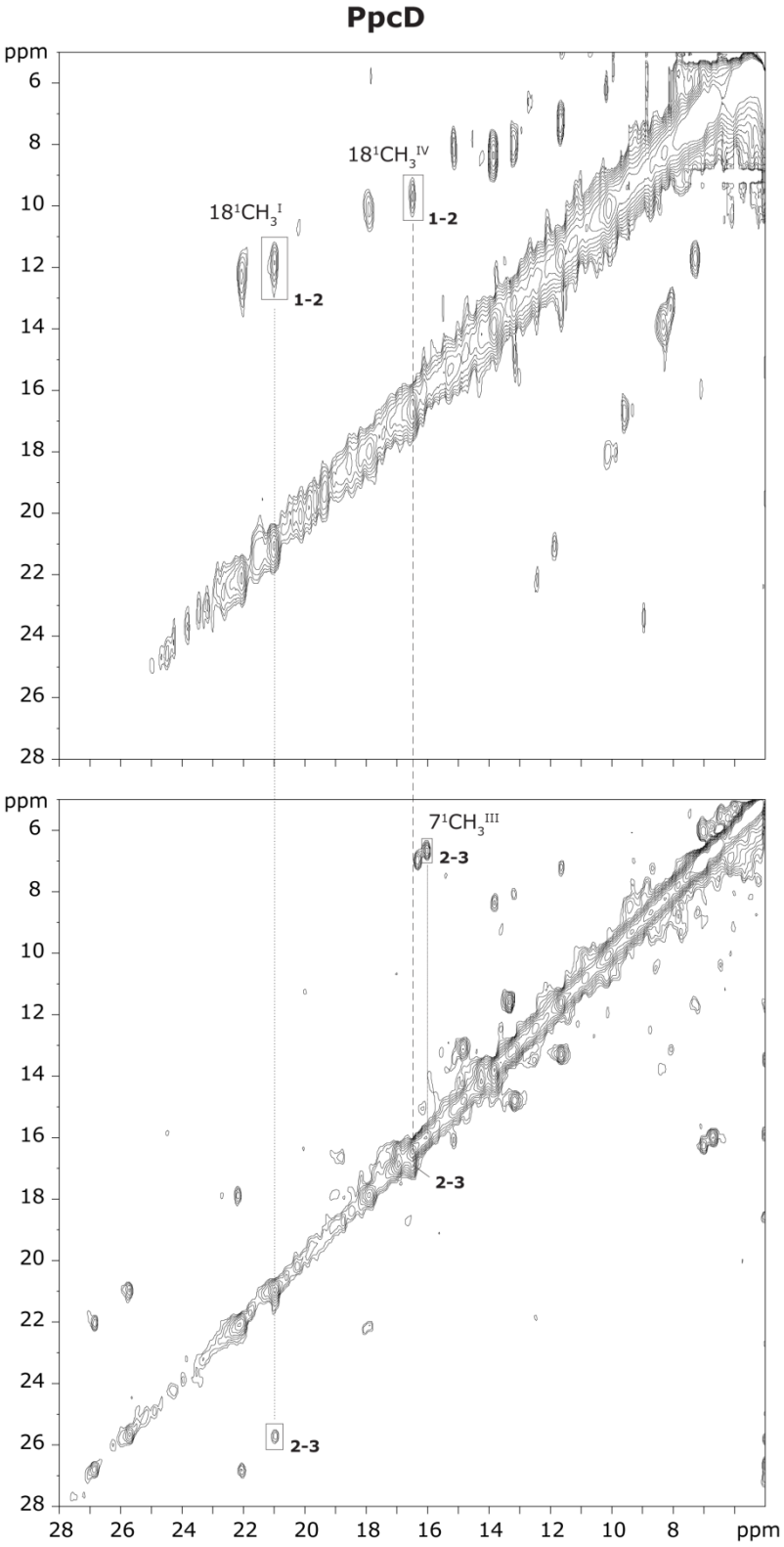

Figure 3.3 (cont) – Expansions of 2D-EXSY NMR spectra obtained at 15 °C and pH 8 for PpcA, PpcB, PpcE and PpcD at different degrees of oxidation.

From this type of experiments, it is possible to obtain the chemical shifts of each methyl in all oxidation stages. The heme fractions of oxidation x_i can be calculated according to Equation 3.1

$$x_i = \frac{(\delta_i - \delta_0)}{(\delta_3 - \delta_0)} \qquad \textbf{Equation 3.1}$$

where δ_i, δ_0, and δ_3 are the observed chemical shift of the heme methyl in oxidation stage *i*, 0, and 3, respectively.

The chemical shifts of the heme methyls in the different oxidation stages at pH 8.0, as well as the correspondent heme oxidation fractions, are listed in Table 3.1.

Table 3.1 – Redox-dependent heme methyl chemical shifts of PpcA, PpcB, PpcD and PpcE at pH 8. The value indicated in parenthesis was obtained from the fitting of the thermodynamic model.

PpcA	**Chemical shift (ppm)**			x_i			$\sum x_i$
Oxidation stage	$12^1CH_3^I$	$7^1CH_3^{III}$	$12^1CH_3^{IV}$	$12^1CH_3^I$	$7^1CH_3^{III}$	$12^1CH_3^{IV}$	
0	2.55	4.14	3.95	0	0	0	0
1	11.22	7.38	8.44	0.45	0.23	0.28	0.96
2	19.25	9.40	15.31	0.87	0.37	0.72	1.95
3	21.79	18.42	19.81	1	1	1	3
PpcB	**Chemical shift (ppm)**			x_i			$\sum x_i$
Oxidation stage	$12^1CH_3^I$	$7^1CH_3^{III}$	$12^1CH_3^{IV}$	$12^1CH_3^I$	$7^1CH_3^{III}$	$12^1CH_3^{IV}$	
0	2.73	4.14	3.60	0	0	0	0
1	6.94	9.35	7.74	0.27	0.44	0.25	0.97
2	14.58	11.55	12.87	0.76	0.63	0.57	1.96
3	18.26	15.91	19.98	1	1	1	3
PpcD	**Chemical shift (ppm)**			x_i			$\sum x_i$
Oxidation stage	$18^1CH_3^I$	$7^1CH_3^{III}$	$18^1CH_3^{IV}$	$18^1CH_3^I$	$7^1CH_3^{III}$	$18^1CH_3^{IV}$	
0	3.23	3.92	3.38	0	0	0	0
1	11.85	(6.03)	9.48	0.38	0.17	0.45	1.01
2	20.92	6.66	16.45	0.79	0.23	0.97	1.98
3	25.69	15.98	16.92	1	1	1	3
PpcE	**Chemical shift (ppm)**			x_i			$\sum x_i$
Oxidation stage	$18^1CH_3^I$	$12^1CH_3^{III}$	$12^1CH_3^{IV}$	$18^1CH_3^I$	$12^1CH_3^{III}$	$12^1CH_3^{IV}$	
0	3.30	3.20	3.63	0	0	0	0
1	10.80	11.29	4.83	0.46	0.47	0.07	1.00
2	17.53	15.89	9.11	0.88	0.74	0.35	1.97
3	19.56	20.27	19.17	1	1	1	3

Analysis of this table confirms that the extrinsic shifts for the methyls selected are not significant, since the sums of the oxidation fraction at each oxidation stage are close to integers, and therefore each methyl reflects the averaged oxidation state of its heme in each stage [7-9].

The redox titrations followed by UV-visible take advantage of the spectroscopic properties of cytochromes. In Figure 3.4, the UV-visible spectra of PpcA in the oxidized and reduced states are shown. Characteristic absorption bands are observed for PpcA at 408 (Soret) and 530 nm in the oxidized state, and at 417, 522 (β-band) and 552 nm (α-band) in the reduced state.

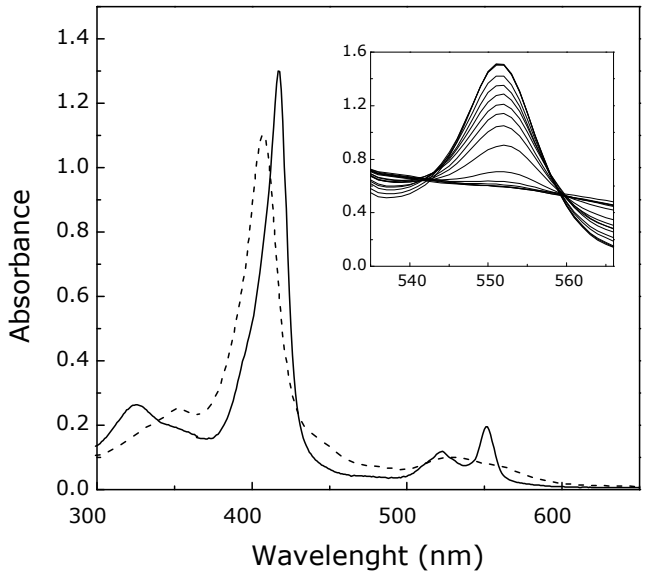

Figure 3.4 – UV–visible spectra of PpcA in the fully oxidized (dashed line) and fully reduced (solid line) states. The inset shows the α-band region of the visible spectra in the redox titration of PpcA at pH 8 and 15 °C.

During the redox titration, the spectrum of the α-band is recorded at different solution potentials (inset in Figure 3.4). The reduced fraction of the protein at each solution potential is then determined by the normalized area of the peak.

To determine the thermodynamic parameters of PpcA, PpcB, PpcD and PpcE, the pH dependence of the paramagnetic chemical shifts of each heme methyl, in the pH range 5.7–9.1, was fitted to the model described in Chapter 2, together with the data from redox titrations followed by UV-visible spectroscopy (Figure 3.5).

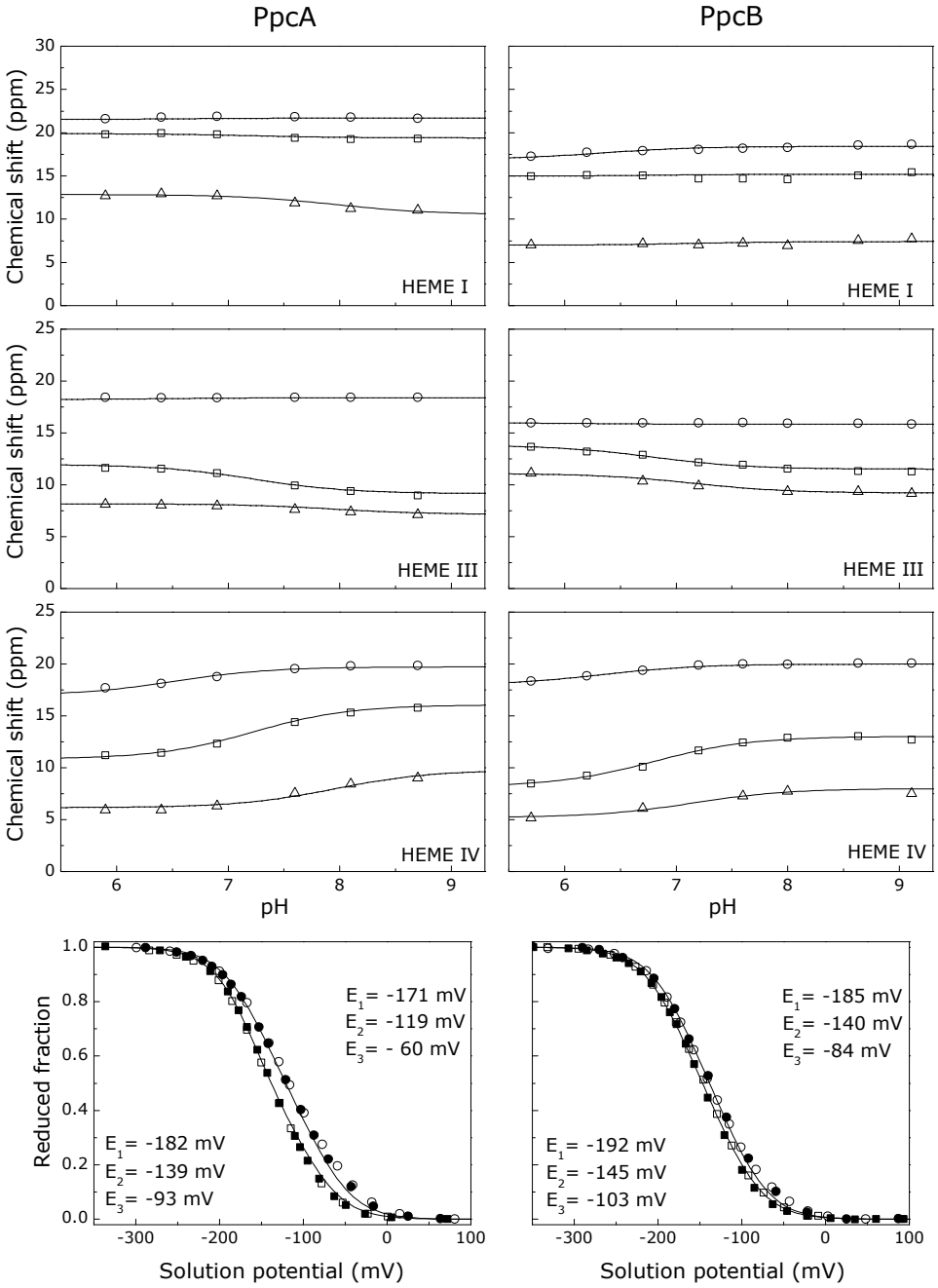

Figure 3.5 – Fitting of the thermodynamic model to the experimental data for PpcA, PpcB, PpcD, and PpcE. The solid lines are the result of the simultaneous fitting of the NMR and UV-visible data. The upper figures show the pH dependence of heme methyl chemical shifts at oxidation stages 1 (△), 2 (□), and 3 (○). The chemical shifts of the heme methyls in the fully reduced stage (stage 0) are not plotted, because they are unaffected by the pH. The last figure in each panel corresponds to the reduced fractions of the various cytochromes, determined by UV-visible spectroscopy at pH 7 (○) and pH 8 (□). The open and solid symbols represent the data points in the reductive and oxidative titrations, respectively. The macroscopic reduction potentials at pH 7 (right) and pH 8 (left) are indicated. The dashed line in the PpcE bottom panel represents a standard n = 1 Nernst curve.

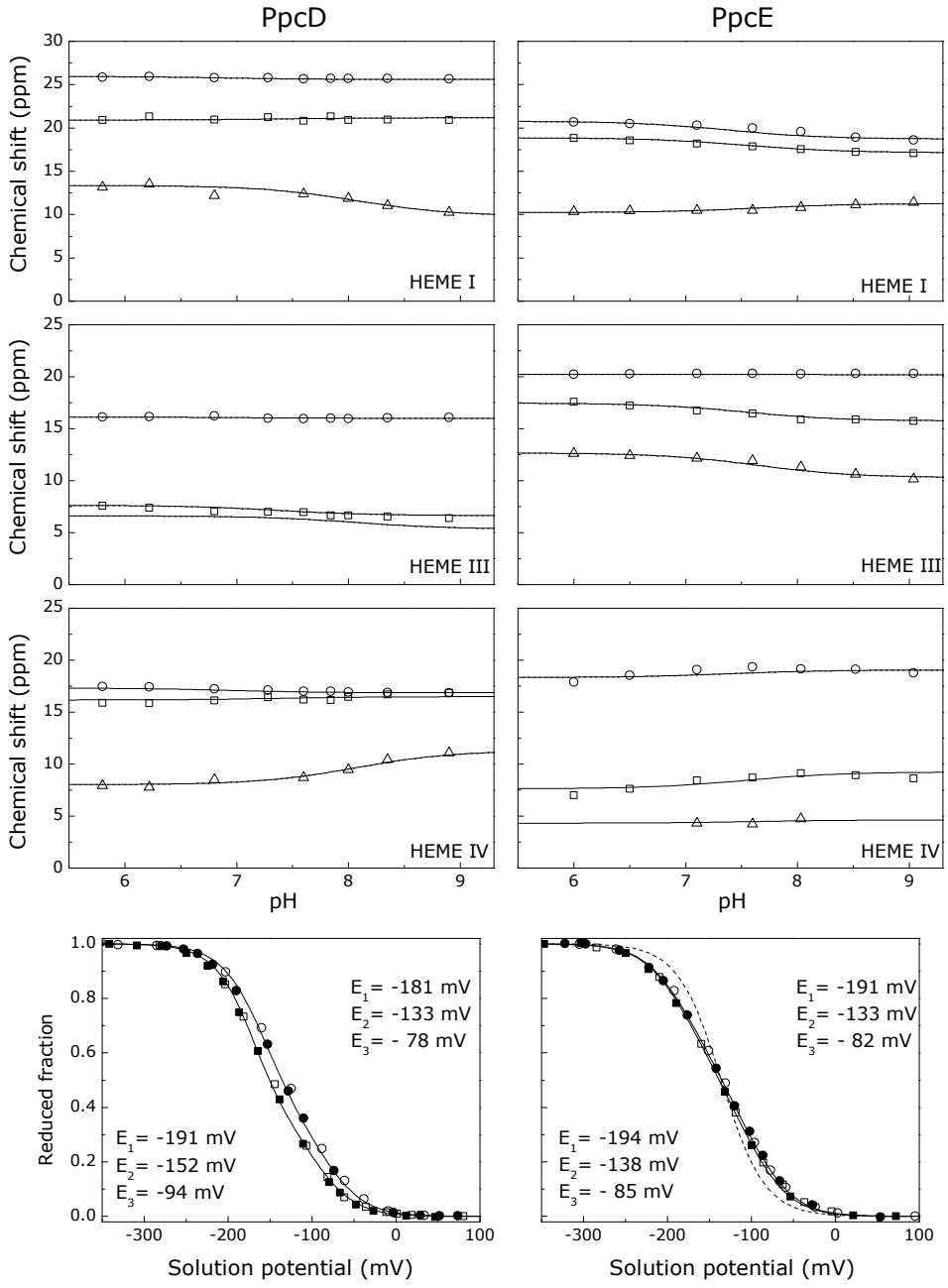

Figure 3.5 (cont.) – Fitting of the thermodynamic model to the experimental data for PpcA, PpcB, PpcD, and PpcE.

The thermodynamic parameters and the macroscopic pK_a values associated with the four stages of oxidation are indicated in Table 3.2 and Table 3.3, respectively.

Table 3.2 – Energy parameters (meV) for PpcA, PpcB, PpcD, and PpcE. Diagonal terms (in boldface type) represent the oxidation energies of the three hemes and the deprotonating energy of the redox-Bohr center (g_H) in the fully reduced and protonated proteins. Off-diagonal values are the redox (heme-heme) and redox-Bohr (heme-proton) interaction energies. The standard errors are given in parentheses. Following the nomenclature for the pairwise interacting centers model [8], the pK_a of the reduced proteins is given by $\boldsymbol{g_H F/([ln10]RT)}$ and the pK_a of the oxidized ones is given by $\boldsymbol{(g_H + \sum g_{iH})F/([ln10]RT)}$.

	Energy (meV)			
PpcA	**Heme I**	**Heme III**	**Heme IV**	**Redox-Bohr center**
Heme I	**-154 (5)**	27 (2)	16 (3)	-32 (4)
Heme III		**-138 (5)**	41 (3)	-31 (4)
Heme IV			**-125 (5)**	-58 (4)
Redox-Bohr center				**495 (8)**
PpcB	**Heme I**	**Heme III**	**Heme IV**	**Redox-Bohr center**
Heme I	**-150 (3)**	17 (2)	8 (2)	-16 (4)
Heme III		**-166 (3)**	32 (2)	-9 (4)
Heme IV			**-125 (3)**	-38 (4)
Redox-Bohr center				**426 (8)**
PpcD	**Heme I**	**Heme III**	**Heme IV**	**Redox-Bohr center**
Heme I	**-156 (6)**	46 (3)	3 (4)	-28 (6)
Heme III		**-139 (6)**	14 (4)	-23 (6)
Heme IV			**-149 (6)**	-53 (6)
Redox-Bohr center				**501 (8)**
PpcE	**Heme I**	**Heme III**	**Heme IV**	**Redox-Bohr center**
Heme I	**-167 (4)**	27 (3)	5 (3)	-12 (4)
Heme III		**-175 (4)**	22 (3)	2 (4)
Heme IV			**-116 (5)**	-13 (4)
Redox-Bohr center				**445 (10)**

Table 3.3 – Macroscopic pK_a values of the redox-Bohr center for PpcA, PpcB, PpcD, and PpcE at each stage of oxidation. The values were calculated from the redox-Bohr center parameters indicated in Table 3.2.

Oxidation stage	**pK_a**			
	PpcA	**PpcB**	**PpcD**	**PpcE**
0	8.6	7.4	8.7	7.7
1	8.0	7.1	8.1	7.6
2	7.2	6.8	7.4	7.5
3	6.5	6.3	6.9	7.4
ΔpK_a	2.1	1.1	1.8	0.3

The quality of the fittings obtained for the pH dependence of the paramagnetic chemical shifts and for the UV-visible redox titrations clearly shows that the thermodynamic properties of all cytochromes are well described by the model used. In particular, the pH dependence of the paramagnetic shifts in the three oxidation stages (data points in Figure 3.5) are dominated by a single pK_a in each stage of oxidation, and thus there is no justification to

consider more than one ionizable center within the framework of the thermodynamic model [8].

When the results previously reported for PpcA at 500 mM and 500 MHz [3] are compared with those obtained under these new conditions, it was verified that there is no significant difference in the parameters. However, the errors associated with the parameters are smaller under the new conditions.

3.2 Discussion

NMR and UV-visible spectroscopy techniques were used to probe the structure and thermodynamic properties of a family of four triheme cytochromes (PpcA, PpcB, PpcD, and PpcE) from *G. sulfurreducens*. The first step was to assign the proton signals of each heme substituents in the fully reduced state in the NMR spectra. This allowed to compare the structural features of the heme core architectures of all cytochromes and to demonstrate their structural similarity in solution. The NMR spectra were also used as a starting point for the thermodynamic studies because these spectra allow to follow the behavior of representative heme methyl signals through the oxidation of the proteins at different pH values. The experimental data obtained, together with data obtained from UV-visible redox titrations, were fitted with the thermodynamic model that considers four interacting charged centers (three hemes and one protonatable center). This permitted to determine the thermodynamic parameters for the four triheme cytochromes, and the specific mechanistic and functional properties of each protein.

3.2.1 Structural characterization of the heme core architecture in solution

The heme proton signals of PpcA, PpcB, PpcD and PpcE were assigned (Table A.1). The assignments were confirmed by examining the interheme NOE connectivities measured from the 2D-NOESY NMR spectra acquired at different mixing times. The NOE connectivities expected to be observed on the basis of their crystal structures were observed in the 100 ms 2D-NOESY NMR spectra for PpcB, PpcD and PpcE, indicating that the heme core structures in crystal and in solution are similar. However, for PpcA additional heme NOE connectivities to those expected based on the crystal structure were observed in solution, suggesting that the crystal and solution heme core structures are not the same. The unexpected connectivities were observed between hemes I and III substituents: $12^1CH_3^I$ - $3^2CH_3^{III}$, $12^1CH_3^I$ - 3^1H^{III}, and $10H^I$ - $3^2CH_3^{III}$ (Figure 3.6).

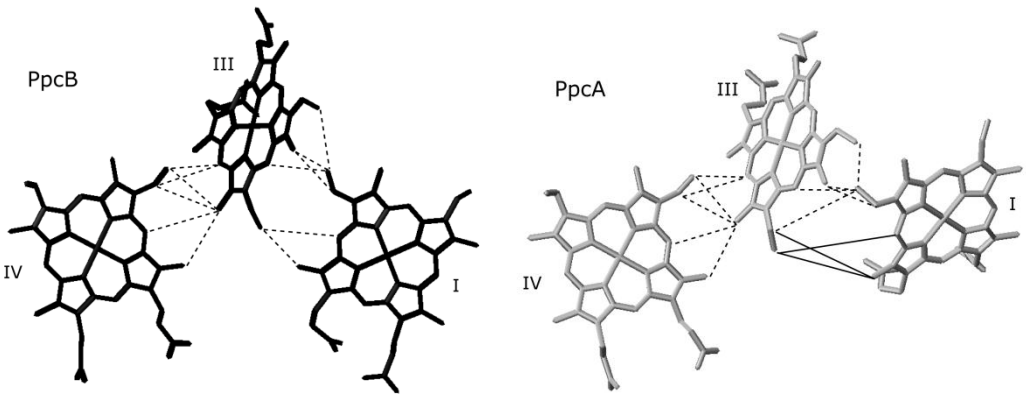

Figure 3.6 – Heme cores of PpcB and PpcA as observed in their crystal structures. The interheme NOE connectivities observed in the 2D-^{1}H-NOESY spectra are illustrated. The dashed lines correspond to the expected connectivities based on the distances obtained from the crystal structures and the solid lines correspond to the unexpected ones.

The observation of these connectivities in solution indicates that these protons are closer (<3.5 Å) than in the crystal structure (5 to 6.5Å). Therefore, the relative orientation and position of hemes I and III of PpcA in solution differ from those observed in the crystal. This suggests that the presence of the deoxycholic acid molecule used in the crystallization of PpcA is affecting its crystal structure. The set of NOE connectivities observed for both PpcA and PpcB clearly show that the heme core architectures of the two cytochromes in solution are very similar.

The good correlation obtained between the heme proton chemical shifts measured for PpcA and those of PpcB (rmsd = 0.11 ppm), PpcD (rmsd = 0.37 ppm), and PpcE (rmsd = 0.26 ppm) confirms the similarity of the heme core solution structures of the four cytochromes (Figure 3.2). Cytochromes PpcD and PpcE showed the largest deviations for some of the heme protons, which is not unexpected since these homologs have lower sequence identity with PpcA (Figure 1.2 – Chapter 1). The best correlation was obtained for the heme IV protons, corroborating the finding that the structure of this heme and its surroundings is the most conserved feature among the four cytochromes [2].

3.2.2 Thermodynamic characterization

The analysis of the thermodynamic parameters of the four *G. sulfurreducens* cytochromes (Table 3.2) shows that, in the fully reduced and protonated state, the reduction potentials of the hemes are negative and different from each other. Although the heme core arrangement is well conserved among these cytochromes, as it is the tertiary structure of the proteins, local structural differences, such as charge and/or solvent exposure variation, were observed [2]. These have been described as important factors in controlling the redox properties of the heme groups [10], and a simple correlation between the structures and the heme reduction potentials is not straightforward, particularly for multiheme proteins with interacting redox centers. The four cytochromes studied differ in 41 out of ~70 amino acids, further complicating such a correlation.

The thermodynamic characterization of the four triheme cytochromes showed that the redox interactions (between each pair of hemes) are positive, indicating that the oxidation of a particular heme renders the oxidation of its neighbors more difficult. The strongest redox interactions are observed between the closest pairs of heme groups: I–III and III–IV. Although they are not identical, the distances between the heme iron atoms and the angles of the heme porphyrin ring planes showed that the heme core arrangement of the hemes is well conserved among these cytochromes [2]. However, the magnitude of the redox interactions varies in each protein, particularly in PpcD and PpcE, which show higher values between hemes I–III. The structural comparison among this family of cytochromes revealed that PpcD and PpcE have one fewer residue before the heme III binding motif [2]. The residue Lys^{49} appears to be conserved in the four proteins, but the structural comparisons suggest that this residue is equivalent to Gly^{48} in PpcA and PpcB. Thus, with one fewer residue at this site, PpcD and PpcE can form regular helices, whereas the other two homologs have a hump in the α-helix in this position. Structural rearrangements that include subtle movements of charged groups and variations in local dielectric constants might

explain these differences, making the correlation between the heme iron atoms' distances highly approximate [11]. The same features have also been observed in tetraheme cytochromes c_3, where, despite a conserved heme core, the pairwise heme-heme interactions differ largely for the various proteins [12].

3.2.3 Structural map of the redox-Bohr center

The redox-Bohr interactions (between the hemes and the redox-Bohr center) are negative, *i.e.*, the oxidation of the hemes facilitates the deprotonation of the acid-base center and *vice versa*. This is designated redox-Bohr effect by analogy with the Bohr effect observed in hemoglobin [13].

The redox-Bohr interactions for PpcA and PpcD are higher than those of PpcB and PpcE (Table 3.2). The magnitude of the redox-Bohr effect at physiological pH can be easily inferred from the separation of the nonstandard n = 1 Nernst redox curves carried out at pH 7 and 8, which describe a $3e^-/H^+$ process for each protein (Figure 3.5). The different degree of the redox-Bohr effect is also reflected in the macroscopic pK_a values of the redox-Bohr center at each oxidation stage (Table 3.3). The larger redox-Bohr effect ($\Delta pK_a = pK_a^{red} - pK_a^{ox}$) is observed for PpcA and PpcD, 2.1 and 1.8 pH units, respectively. The ΔpK_a value is lower for PpcB and much smaller for PpcE (1.1 and 0.3 pH units, respectively). For the cytochromes with a nonnegligible redox-Bohr effect (PpcA, PpcB, and PpcD), heme IV shows the highest redox-Bohr interaction (Table 3.2), suggesting that in all proteins the redox-Bohr center is located in the vicinity of this heme. The differences in the magnitude of the redox-Bohr effect observed for the cytochromes in this study may be a consequence of the combined contributions of fractional protonation of several acid-base groups [14].

In order to confirm this, the pH dependence of the paramagnetic shift of heme IV methyl groups in PpcA, PpcB and PpcD was analyzed. For PpcD it was not possible to follow the resonances of all the methyls from heme IV due to broadness of the signals.

For PpcA and PpcB the results showed that $12^1CH_3^{IV}$ is the most affected during pH titration (Figure 3.7) and, consequently, is sensing a protonation in its close vicinity.

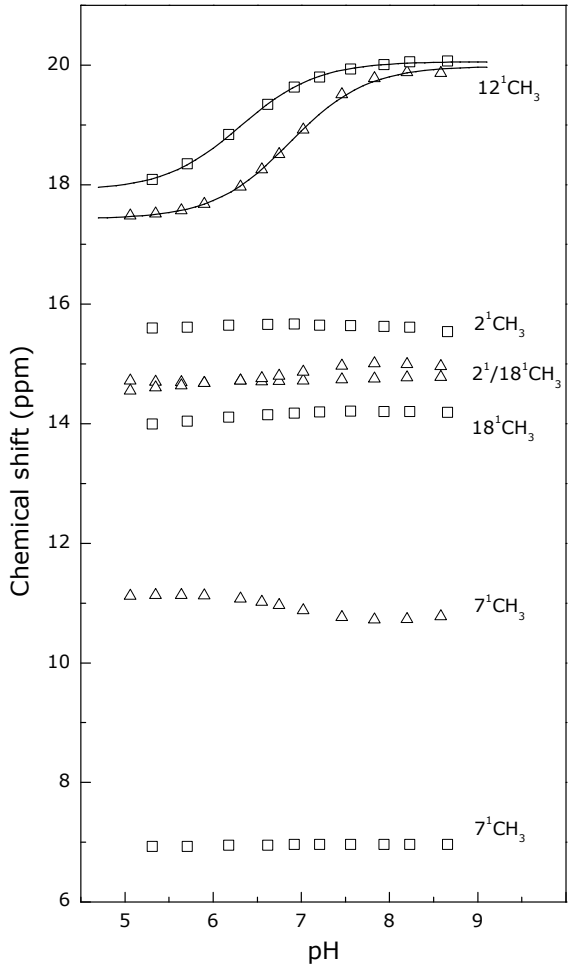

Figure 3.7 – pH dependence for PpcB (□) and PpcA (△) heme IV methyl group paramagnetic shifts. Solid lines were obtained by using the least-squares fitting to Henderson-Hasselbalch equation $\boldsymbol{\delta_{obs} = \delta_A + (\delta_B - \delta_A)\frac{10^{pH-pKa}}{1+10^{pH-pKa}}}$, where δ_{obs}, δ_A, and δ_B are the observed, protonated, and deprotonated chemical shifts, respectively.

Analysis of the PpcB structure (PDB 3BXU [15]) shows that, apart from His and Cys residues which are involved in binding the hemes, all the remaining residues with protonatable groups (Glu, Asp, Lys, N-terminus, and C-terminus) are distant and pointing away from $12^1CH_3{}^{IV}$ and thus cannot explain such pH dependence. Consequently, the best candidate to be responsible for the redox-Bohr effect is the carboxylate group of heme IV propionate 13 ($P_{13}{}^{IV}$, according to the IUPAC Nomenclature [16], Figure 2.1 – Chapter 2). The paramagnetic chemical shift of a heme substituent has two components: (i) the contact shift, which is a through-bond effect and depends on the heme unpaired electronic distribution; and (ii) the pseudocontact shift which is a spatial effect. The magnitude of the observed paramagnetic shifts is mostly dominated by the contact contribution [17]. From all heme IV methyl substituents, $12^1CH_3{}^{IV}$ showed the largest paramagnetic shift (Figure 3.7). This indicates that the heme molecular orbitals that contain most of the unpaired electron density are oriented towards the heme substituents $12^1CH_3{}^{IV}$ and $P_{13}{}^{IV}$. The paramagnetic shift of a heme substituent is unlikely to be strongly affected by the through-space electric field of a charge. However, due to the orientation of the heme molecular orbitals in PpcB, the

protonation of P_{13}^{IV} carboxylate group can be indirectly measured on the paramagnetic chemical shift of the closest heme methyl substituent. The pK_a value of 6.3 obtained from the $12^1CH_3^{IV}$ chemical shifts pH dependence is significantly higher in comparison with those of free carboxylic acids (pK_a~4), indicating that P_{13}^{IV} carboxylate group is partially shielded from the solvent.

In PpcA, heme methyl $12^1CH_3^{IV}$ is also the one most affected by the pH of the solution (Figure 3.7). From the fitting of the pH dependence of its paramagnetic chemical shift, a pK_a value of 6.9 was obtained. The unusual pK_a value of the P_{13}^{IV} carboxylate group obtained for both cytochromes correlates well with the fact that this propionate chain is partially buried in the protein core.

3.2.4 Order of oxidation of the heme groups

The relative order of oxidation of the heme groups in the fully protonated and reduced proteins can be obtained from the microscopic reduction potentials listed in Table 3.2: I-III-IV for PpcA, III-I-IV for PpcB and PpcE, and I-IV-III for PpcD. However, the reduction potential of each heme is affected by the oxidation state of neighboring ones and by the pH. This effect is reflected on the individual oxidation profiles of the hemes shown in Figure 3.8.

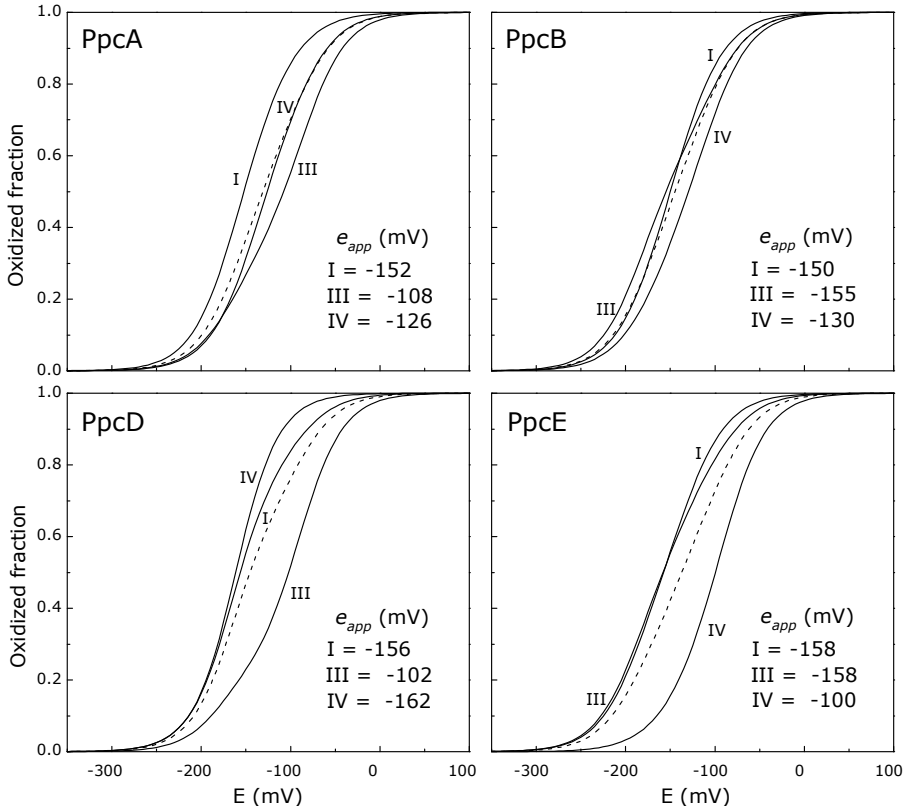

Figure 3.8 – Individual heme oxidation fractions (labeled with Roman numerals) for PpcA, PpcB, PpcD, and PpcE (solid lines). The dashed line indicates the global oxidation fraction of each protein. The curves were calculated as a function of the solution reduction potential at pH 7.5 using the parameters listed in Table 3.2. The midpoint reduction potentials (e_{app}) of the individual hemes are also indicated.

These curves are substantially different from a pure Nernst curve, and the several crossovers clearly indicate that the electron affinity of each heme is tuned by the redox interactions. Thus, during the oxidation of each protein, the affinity of each redox center is modulated such that their apparent midpoint reduction potentials e_{app} (*i.e.*, the point at which the oxidized and reduced fractions of each heme group are equally populated) are different in relation to those in the fully reduced protein (*cf.* Table 3.2 and Figure 3.8). Consequently, the actual order of the midpoint reduction potentials at physiological pH is I-IV-III for PpcA, (III,I)-IV for PpcB and PpcE, and (IV,I)-III for PpcD. This shows how structural related proteins can specifically fine-tune their redox centers, a feature that cannot be envisaged from the macroscopic redox curves (dashed lines in Figure 3.8).

3.2.5 Relevant microstates in solution

In order to analyze the functional mechanism of PpcA, PpcB, PpcD, and PpcE at physiological pH, the molar fractions of the 16 microstates were obtained from the thermodynamic parameters listed in Table 3.2 (Figure 3.9).

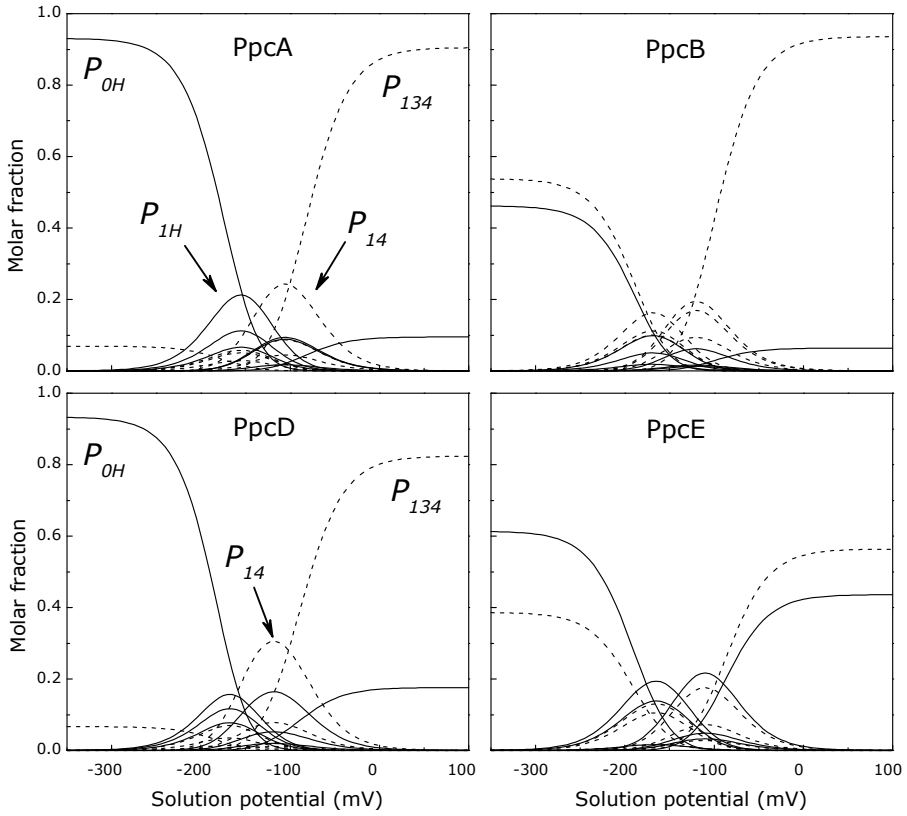

Figure 3.9 – Molar fractions of the 16 individual microstates (described in Figure 2.5 – Chapter 2) of PpcA, PpcB, PpcD, and PpcE at pH 7.5. The curves were calculated as a function of the solution reduction potential using the parameters listed in Table 3.2. Solid and dashed lines indicate the protonated and deprotonated microstates, respectively. For clarity, only the relevant microstates are labeled.

From the analysis of Figure 3.9 it is clear that the dominant microstates are different in each protein. In the case of PpcA, oxidation stages 0 and 1 are dominated by the protonated forms P_{0H} and P_{1H}, respectively, while the redox-Bohr center is kept protonated. Stage 2 is dominated by the oxidation of heme IV and deprotonation of the redox-Bohr center (P_{14}), which remains deprotonated in stage 3 (P_{134}). Therefore, a route is defined for the electrons within PpcA: $P_{0H} \rightarrow P_{1H} \rightarrow P_{14} \rightarrow P_{134}$. In the case of PpcD, a different profile for electron transfer is observed. Oxidation stage 0 is dominated by the protonated form P_{0H}. However, the microstates of oxidation stage 1 are overcome by the P_{0H} curve, which earlier intercepts the P_{14} curve. This microstate (P_{14}) dominates oxidation stage 2, whereas P_{134} dominates stage 3. Thus, for this cytochrome, a different preferential route for electrons is established, favoring a proton-coupled $2e^-$ transfer step between oxidation stages 0 and 2: $P_{0H} \rightarrow P_{14} \rightarrow P_{134}$. The small redox interaction between hemes I and IV, and the proximity of their reduction potentials in PpcD, in comparison with those of PpcA, favors a $2e^-$ transfer step in PpcD. Since the redox-Bohr parameters of both proteins are of similar magnitude, it can also be inferred that the redox-Bohr center does not control this pathway.

In the case of PpcB and PpcE, several microstates are significantly populated in oxidation stages 1 and 2, and therefore no preferential pathway for electron transfer can be established.

These observations, together with the order of the midpoint reduction potentials, suggest that heme III might play a key regulatory role in the functional mechanism of each cytochrome by controlling the microscopic redox states that the protein can access during the redox cycle and thus establishing preferential pathways for electron transfer. Indeed, the relative value of the reduction potential of heme III seems to be a crucial factor in allowing these proteins to couple electron transfer with deprotonation of the acid-base center. In fact, only PpcA and PpcD, for which heme III has the highest reduction potential, have preferential pathways for electron transfer with e^-/H^+ coupling being established.

3.3 Functional implications

Optimal growth of *G. sulfurreducens* occurs at pH 7–8 (K.P. Nevin, University of Massachusetts, personal communication, 2009) and is severely limited at pH 6 [18]. A direct measurement of the periplasmic pH in the Gram-negative bacterium *E. coli* showed that the periplasmic pH remains at or near to the pH of the external medium [19]. Thus, it is reasonable to assume that in the Gram-negative *G. sulfurreducens*, the periplasmic pH would also be closer to that of the external medium, with optimal growth conditions ranging from pH 7 to 8. Therefore, in this work a pH value of 7.5 was chosen to discuss the functional consequences of the thermodynamic properties of the cytochromes. Additionally, cyclic voltammetry experiments on *G. sulfurreducens* biofilms have shown that the reduction potential of the *G. sulfurreducens* cells is 150 mV [20]. Thus, as can be seen from Figure 3.8 and Table 3.3, under these conditions of physiological redox potential (150 mV) and pH (7.5), the cytochromes studied are not fully oxidized or fully reduced, and thus are functionally active (*i.e.*, capable of receiving and donating electrons).

From the thermodynamic properties determined, it is clear that, despite the high degree of sequence and structural homology, the *G. sulfurreducens* periplasmic triheme cytochromes behave quite differently. For PpcA and PpcD, dominant microstates emerge during protein oxidation (Figure 3.9). In both cases, the oxidation progresses from particular protonated redox-microstates to particular deprotonated redox-microstates, showing how dominant microstates can confer the directionality of events (Figure 3.10).

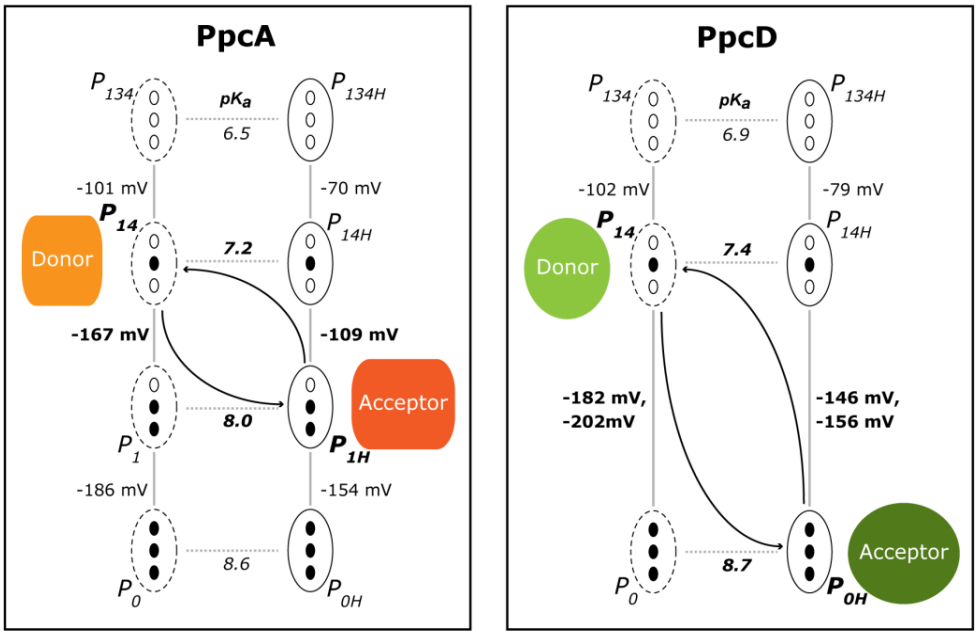

Figure 3.10 – Thermodynamic and mechanistic bases for energy transduction by PpcA (left) and PpcD (right). The functional pathway involving the significantly populated microscopic redox states in Figure 3.9 is indicated by arrows in each scheme. The microstates are labeled as in Figure 2.5 – Chapter 2. The pK_a values are those listed in Table 3.3, and the reduction potentials were calculated from the values indicated in Table 3.2. As a concrete example, the redox potential for the equilibrium involving the protonated microstates P_{1H} and P_{14H} for PpcA (-109 mV) is obtained by the sum of the energy terms corresponding to heme IV oxidation (-125 mV) and I-IV redox interaction (16 mV).

At the physiological redox potential and pH, PpcA can uptake a strongly reducing electron (-167 mV) and a weakly acidic proton (pK_a 8.0) from the donor associated with the cytoplasmic membrane. When it meets its physiological downstream redox partner, PpcA donates de-energized electrons (-109 mV) and a more acidic proton (pK_a 7.2), that is now sufficiently acidic to be released into the periplasm.

PpcD can also couple the transfer of electrons and protons, though by a different mechanism and covering a different redox potential range (Figure 3.10). Indeed, the relevant microstates that are involved in the energy transduction in PpcA work in the range of -167 to -109 mV, whereas those of PpcD work in the range of -202 to -146 mV.

It is quite interesting that PpcA and PpcD can perform e^-/H^+ energy transduction in addition to their role in the electron transfer pathways that lead to the reduction of extracellular electron acceptors. This may represent additional mechanisms contributing to the proton electrochemical potential gradient across the periplasmic membrane that drives ATP synthesis. The use of extracellular electron acceptors by *G. sulfurreducens*, in comparison with the use of fumarate, leads to a decrease in biomass production because of dissipation of the membrane potential by cytoplasm acidification [21]. In contrast, the cytoplasmic protons produced from acetate oxidation are consumed in the cytoplasm when fumarate is the terminal electron acceptor. In metabolic modeling studies, Mahadevan *et al.* [21] showed that cellular growth in the presence of insoluble electron acceptors is possible only when additional e^-/H^+ coupling mechanisms (compared to those used in fumarate respiration) are present. The authors suggested that the most likely mechanism for generating additional membrane potential is the coupling of electron transfer to periplasmic cytochromes with proton translocation, so that additional membrane potential can be generated for ATP production. Thus, it can be proposed that PpcA and PpcD contribute to an additional transmembrane pH gradient by receiving weakly acidic protons (pK_a > 8.0) and electrons from donors associated with the cytoplasmic membrane. These protons will then be released in the more-acidic periplasmic space with a lower pK_a (<7.5) upon electron transfer to the acceptor.

On the other hand, PpcB and PpcE appear to be designed to perform different cellular functions, since no evidence for coupling of e^-/H^+ transfer was observed. Furthermore, the observation of different working potential ranges for these cytochromes suggests that they may have physiological redox partners distinct from those of PpcA and PpcD.

The distinct functional properties described here for the four *G. sulfurreducens* triheme cytochromes correlate with previous proteomics and knockout mutant studies of *G. sulfurreducens* [22,23]. Those studies showed that PpcA and PpcD play a significant role in the respiration of iron oxides. Their different detailed functional mechanisms with respect to reduction potentials and pK_a values suggest that they interact with distinct partners. These differences provide an excellent example of how structurally related proteins from the same microorganism can interact with different physiological partners, and establish a rationalization for the coexistence of five homologous periplasmic triheme cytochromes in *G. sulfurreducens*. This work provides the first step in unraveling the organization of the complex network of redox proteins found in the periplasmic space of the bacterium *G. sulfurreducens*.

3.4 References

[1] DL Turner, CA Salgueiro, J LeGall, AV Xavier (1992) Structural studies of *Desulfovibrio vulgaris* ferrocytochrome c_3 by two-dimensional NMR, Eur J Biochem 210, 931-936.

[2] PR Pokkuluri, YY Londer, X Yang, NE Duke, J Erickson, V Orshonsky, et al. (2010) Structural characterization of a family of cytochromes c_7 involved in Fe(III) respiration by *Geobacter sulfurreducens*, Biochim Biophys Acta 1797, 222-232.

[3] M Pessanha, L Morgado, RO Louro, YY Londer, PR Pokkuluri, M Schiffer, et al. (2006) Thermodynamic characterization of triheme cytochrome PpcA from *Geobacter sulfurreducens*: evidence for a role played in e^-/H^+ energy transduction, Biochemistry 45, 13910-13917.

[4] IJ Correia, CM Paquete, RO Louro, T Catarino, DL Turner, AV Xavier (2002) Thermodynamic and kinetic characterization of trihaem cytochrome c_3 from *Desulfuromonas acetoxidans*, Eur J Biochem 269, 5722-5730.

[5] ATCC, American Type Culture Collection recommendation for *Geobacter* growth media 51573™ (www.atcc.org).

[6] L Morgado, M Bruix, YY Londer, PR Pokkuluri, M Schiffer, CA Salgueiro (2007) Redox-linked conformational changes of a multiheme cytochrome from *Geobacter sulfurreducens*, Biochem Biophys Res Commun 360, 194-198.

[7] CA Salgueiro, DL Turner, H Santos, J LeGall, AV Xavier (1992) Assignment of the redox potentials to the four haems in *Desulfovibrio vulgaris* cytochrome c_3 by 2D-NMR, FEBS Lett 314, 155-158.

[8] DL Turner, CA Salgueiro, T Catarino, J LeGall, AV Xavier (1996) NMR studies of cooperativity in the tetrahaem cytochrome c_3 from *Desulfovibrio vulgaris*, Eur J Biochem 241, 723-731.

[9] L Morgado, AP Fernandes, YY Londer, PR Pokkuluri, M Schiffer, CA Salgueiro (2009) Thermodynamic characterization of the redox centres in a representative domain of a novel *c*-type multihaem cytochrome, Biochem J 420, 485-492.

[10] P Voigt, EW Knapp (2003) Tuning heme redox potentials in the cytochrome *c* subunit of photosynthetic reaction centers, J Biol Chem 278, 51993-52001.

[11] RO Louro, T Catarino, CM Paquete, DL Turner (2004) Distance dependence of interactions between charged centres in proteins with common structural features, FEBS Lett 576, 77-80.

[12] CM Paquete, DL Turner, RO Louro, AV Xavier, T Catarino (2007) Thermodynamic and kinetic characterisation of individual haems in multicentre cytochromes c_3, Biochim Biophys Acta 1767, 1169-1179.

[13] MF Perutz, AJ Wilkinson, M Paoli, GG Dodson (1998) The stereochemical mechanism of the cooperative effects in hemoglobin revisited, Annu Rev Biophys Biomol Struct 27, 1-34.

[14] BM Fonseca, IH Saraiva, CM Paquete, CM Soares, I Pacheco, CA Salgueiro, et al. (2009) The tetraheme cytochrome from *Shewanella oneidensis* MR-1 shows thermodynamic bias for functional specificity of the hemes, J Biol Inorg Chem 14, 375-385.

[15] L Morgado, M Bruix, V Orshonsky, YY Londer, NE Duke, X Yang, et al. (2008) Structural insights into the modulation of the redox properties of two *Geobacter sulfurreducens* homologous triheme cytochromes, Biochim Biophys Acta 1777, 1157-1165.

[16] GP Moss (1988) Nomenclature of tetrapyrroles. Recommendations 1986 IUPAC-IUB Joint Commission on Biochemical Nomenclature (JCBN), Eur J Biochem 178, 277-328.

[17] CA Salgueiro, DL Turner, AV Xavier (1997) Use of paramagnetic NMR probes for structural analysis in cytochrome c_3 from *Desulfovibrio vulgaris*, Eur J Biochem 244, 721-734.

[18] AE Franks, KP Nevin, H Jia, M Izallalen, TL Woodard, DR Lovley (2009) Novel strategy for three-dimensional real-time imaging of microbial fuel cell communities: monitoring the inhibitory effects of proton accumulation within the anode biofilm, Energy Environ Sci 2, 113-119.

[19] JC Wilks, JL Slonczewski (2007) pH of the cytoplasm and periplasm of *Escherichia coli*: rapid measurement by green fluorescent protein fluorimetry, J Bacteriol 189, 5601-5607.

[20] H Richter, KP Nevin, H Jia, DA Lowy, DR Lovley, LM Tender (2009) Cyclic voltammetry of biofilms of wild type and mutant *Geobacter sulfurreducens* on fuel cell anodes indicates possible roles of OmcB, OmcZ, type IV pili, and protons in extracellular electron transfer, Energy Environ Sci 2, 506-516.

[21] R Mahadevan, DR Bond, JE Butler, A Esteve-Núñez, MV Coppi, BO Palsson, et al. (2006) Characterization of metabolism in the Fe(III)-reducing organism *Geobacter sulfurreducens* by constraint-based modeling, Appl Environ Microbiol 72, 1558-1568.

[22] YH Ding, KK Hixson, MA Aklujkar, MS Lipton, RD Smith, DR Lovley, et al. (2008) Proteome of *Geobacter sulfurreducens* grown with Fe(III) oxide or Fe(III) citrate as the electron acceptor, Biochim Biophys Acta 1784, 1935-1941.

[23] ES Shelobolina, MV Coppi, AA Korenevsky, LN Didonato, SA Sullivan, H Konishi, et al. (2007) Importance of *c*-type cytochromes for U(VI) reduction by *Geobacter sulfurreducens*, BMC Microbiol 7, 16.

STRUCTURAL STUDIES ON PPCA[2]

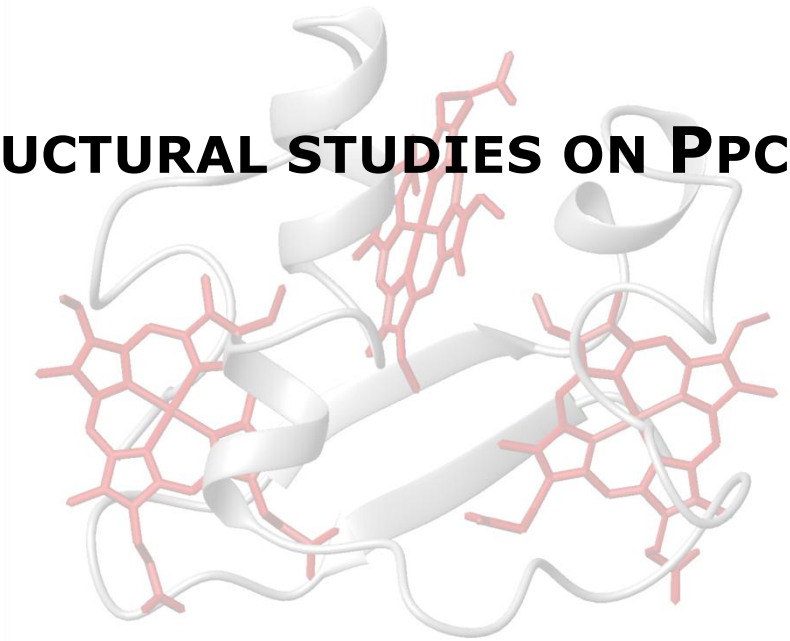

[2] Partially reproduced from: L Morgado, VB Paixão, CA Salgueiro, M Bruix (2011) Backbone, side chain and heme resonance assignments of the triheme cytochrome PpcA from *Geobacter sulfurreducens*, Biomol NMR Assign 5, 113-116 (http://dx.doi.org/10.1007/s12104-010-9280-3) and L Morgado, VB Paixao, M Schiffer, PR Pokkuluri, M Bruix, CA Salgueiro (2012) Revealing the structural origin of the redox-Bohr effect: the first solution structure of a cytochrome from *Geobacter sulfurreducens*, Biochem J 441, 179-187 (http://dx.doi.org/10.1042/BJ20111103), according to the Editors' Copyright Policy.

4. STRUCTURAL STUDIES ON PPCA

G. sulfurreducens' genome encodes for 111 cytochromes and despite their abundance and key functional roles, to date there is no structural information for these proteins in solution. Structural information on these systems is crucial to understand their functional mechanisms.

NMR spectroscopy was used to determine PpcA solution structure in the fully reduced state, its backbone dynamics and the pH-dependent conformational changes. In order to avoid different levels of protonation of the groups involved in the redox-Bohr effect, and a concomitant broadening of the signals, the PpcA solution structure was determined at pH 7.1, which is more than one pH unit lower than the redox-Bohr center pK_a in the reduced protein (Chapter 3).

The structure obtained is well defined, with an average pairwise rmsd of 0.25 Å for the backbone atoms and 0.99 Å for all heavy atoms, and constitutes the first solution structure of a *G. sulfurreducens* cytochrome. The redox-Bohr center responsible for controlling the e^-/H^+ transfer was identified, as well as the putative interacting regions between PpcA and its redox partners. The solution structure of PpcA constitutes the foundations for studies aiming to map out in detail these interacting regions.

4.1 Results

4.1.1 Backbone, side chain and heme resonance assignments in the reduced state

Protein solution structure determination relies on distance restraints that are obtained from the measurement of the intensity of the NOEs signals between atoms in close spatial proximity. These restraints are obtained from the analysis of 2D-NOESY NMR spectra, for which an unambiguous assignment of the protein signals is essential.

In addition to the three *c*-type heme groups, PpcA contains an unusually high content (24%) of lysine residues [1]. In comparison with non-heme proteins, the presence of numerous proton-containing groups in the heme co-factors causes additional challenges to the full protein assignment. Also, the number of structural restraints associated with the heme signals are, in average, four times higher than those involving any protein residue and their assignment is critical to the accomplishment of a high resolution structure.

For the determination of PpcA solution structure in the reduced state, uniformly ^{15}N labeled and unlabeled PpcA were produced as described in Chapter 2.

All heme proton signals in the reduced protein span the same region of the polypeptide signals and, consequently, NOEs belonging to the heme are obscured by the NOE connectivity's involving the amino acids signals. In order to unambiguously assign the heme proton signals, 2D-NMR spectra were acquired for a non-labeled PpcA sample in D_2O. These spectra were used to assign all the heme proton signals following the strategy described by Turner *et al.* [2].

After assigning the 60 heme proton signals, all backbone amide, except for the two first residues, were assigned using spectra acquired for a ^{15}N labeled PpcA sample and following the strategy described in Chapter 2. Figure 4.1 shows the ^{1}H-^{15}N HSQC NMR spectrum of labeled PpcA with the backbone nitrogen resonances assigned as well as those of the side chains of Asn^{10}, Gln^{21} and the six axial histidines (His^{17}, His^{20}, His^{31}, His^{47}, His^{55} and His^{69}).

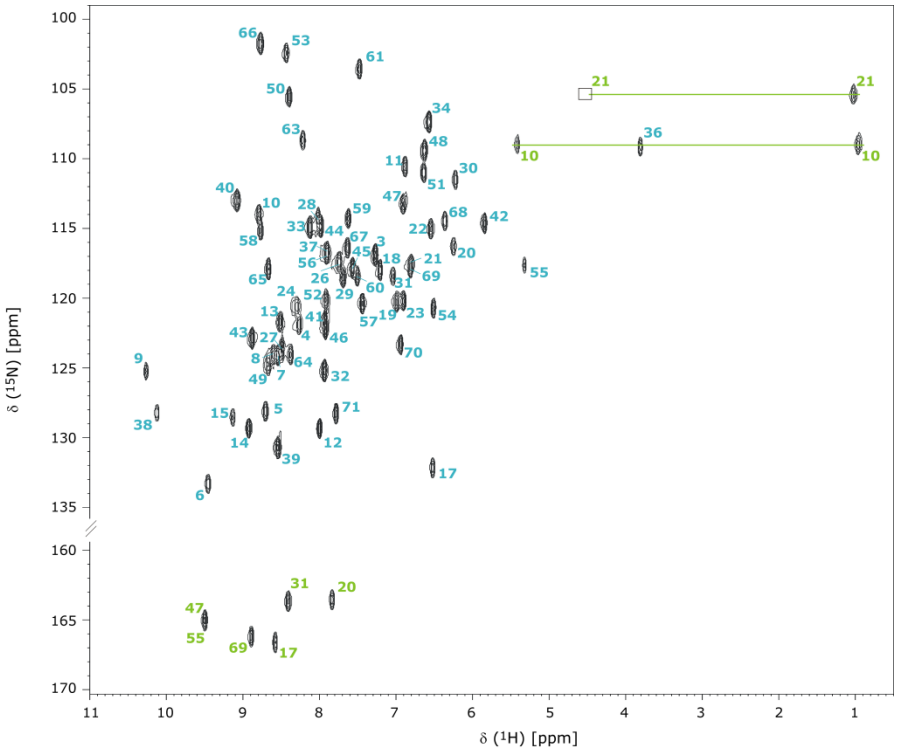

Figure 4.1 – ^{1}H-^{15}N HSQC spectrum of fully reduced PpcA (1 mM protein in 45 mM sodium phosphate buffer pH 7.1, 25 °C). Blue and green labels represent ^{1}H-^{15}N connectivity's for backbone and side-chains groups (Nδ_2 of Asn^{10}, Nε_2 of Gln^{21} and Nδ_1 of axial histidines), respectively.

The ring-current effects generated by each of the three heme groups are extremely strong in comparison with those produced by the amino acid aromatic side chains. Consequently, the nuclei located in close proximity to the heme groups are subject to a strong ring-current contribution on their observed shifts. The more affected nuclei are those belonging to the axial histidines. In fact, the ring proton signals (Hδ_2 and Hε_2) are strongly up-field shifted appearing in the -0.50 to 1.60 ppm range. This clearly contrasts with the typical positions found for these signals in non-heme proteins (in the range 7 to 8 ppm). The effect of the ring current shifts is also extended to the nitrogen atoms (Nδ_1) of the axial histidine side chains, which appear in very characteristic positions (160 to 170 ppm) in the ^{1}H-^{15}N HSQC NMR spectrum (Figure 4.1). The chemical shifts of other nuclei located in the neighborhoods of the heme groups are also significantly affected as it is the case of the Hα of Pro^{35} (0.74 ppm), Lys^{43} (2.43 ppm) and Gly^{61} (1.15 and 2.56 ppm).

In addition to the axial histidines, PpcA contains two free aromatic phenylalanine residues, Phe^{15} and Phe^{41}. The aromatic ring protons of these two residues are in distinct chemical exchange regime in the NMR time scale: the five aromatic protons of Phe^{15} originate five discrete resonances (slow chemical exchange) whereas those of Phe^{41} only originate three resonances (fast chemical exchange). These results show that Phe^{15} aromatic ring in solution is immobilized in the hydrophobic core of the protein.

The total extent of the assignment is 93%, excluding carboxyl, amino and hydroxyl groups and has been deposited in the Biological Magnetic Resonance Data Bank (BMRB, http://www.bmrb.wisc.edu) under BMRB accession number 16842 (Table A.2 – Appendix).

4.1.2 Structure calculations

The 2D-NOESY NMR spectrum acquired in H_2O was assigned and cross-peaks were integrated and converted into volume restraints, resulting in 1115 lower limits for volumes (lov) and 1434 upper limits (upv) (Table 4.1). These were used as input for the program PARADYANA [3] together with a set of 69 fixed upper limit distances. The preliminary structures were analysed using the program GLOMSA [4], modified to take NOE volumes as input, and 32 stereospecific assignments were made for diastereotopic pairs of protons or methyl groups.

Table 4.1 – Summary of restraint violations and quality analysis for the final families of structures for PpcA.

Parameter	
Type of distance restraint	
Intra-residue	879
Sequential	550
Medium range ($2 \leq \|i - j\| < 5$)	501
Long range ($\|i - j\| \geq 5$)	619
Total	2549
	(1115 lov + 1434 upv)
Upper distance limit violations	
Average maximum (Å)	0.19 ± 0.01
Number of consistent violations (>0.2Å)	0
Lower distance limit violations	
Average maximum (Å)	0.20 ± 0.01
Number of consistent violations (>0.2Å)	0
Van de Waals violations	
Average maximum (Å)	0.17 ± 0.01
Number of consistent violations (>0.2Å)	0
Ramachandran Plot (%) [a]	
Most favoured regions	70.4
Additionally allowed regions	29
Generously allowed regions	0.5
Disallowed regions	0.2
Stereospecific Assignments [b]	32
Precision	
Average pairwise rmsd backbone (Å)	0.25 ± 0.07
Average pairwise rmsd heavy atoms (Å)	0.99 ± 0.10

[a] Values obtained with PROCHECK-NMR

[b] Analysis with GLOMSA

The effect of spin diffusion introduces an uncertainty into the conversion of experimental data to distance constraints. This effect was simulated by complete relaxation matrix calculations based on the initial protein structures and, accordingly, a parameter was set in the program PARADYANA to loosen all distance restraints by 5%.

An average of 36 NOE restraints per amino acid residue (16 lovs and 20 upvs) and 170 per heme residue (74 lovs and 96 upvs) was used for the final calculation (Figure 4.2). The distribution of the number of constraints is not uniform along the protein sequence, as heme groups attached to positions 30, 54 and 68 show many long distance contacts.

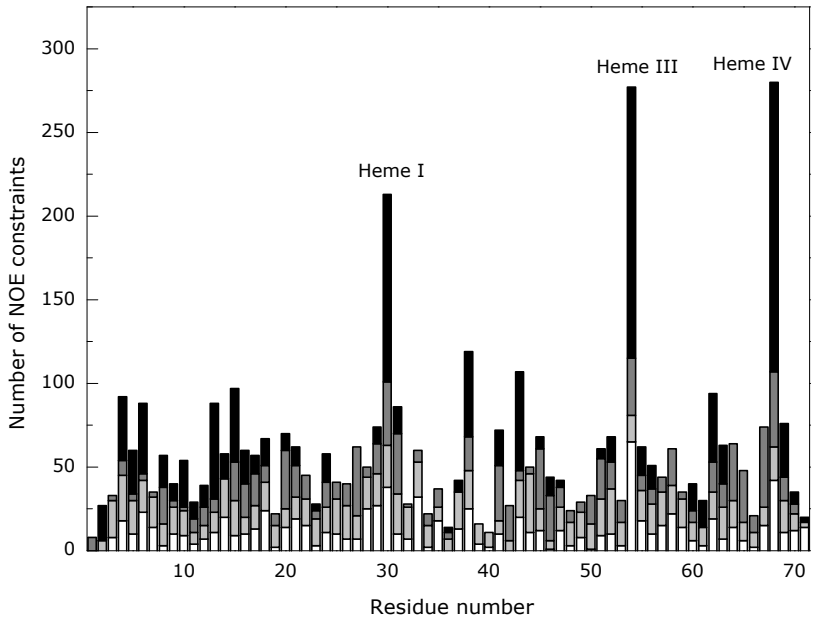

Figure 4.2 – Number of constraints per residue used for the calculation of the structure of PpcA. Bars are white, light gray, dark gray and black for intra residue, sequential, medium and long range restraints, respectively. Residues 30, 54 and 68 also include restraints to hemes I, III and IV, respectively.

4.1.3 Quality and analysis of the structures

The twenty structures with the lowest target function values (from 1.94 $Å^2$ to 2.16 $Å^2$, average value 2.07 $Å^2$, 11% range from the lowest value) were selected as representative of the solution structure of the protein and were deposited in the Protein Data Bank under accession code 2LDO (Figure 4.3).

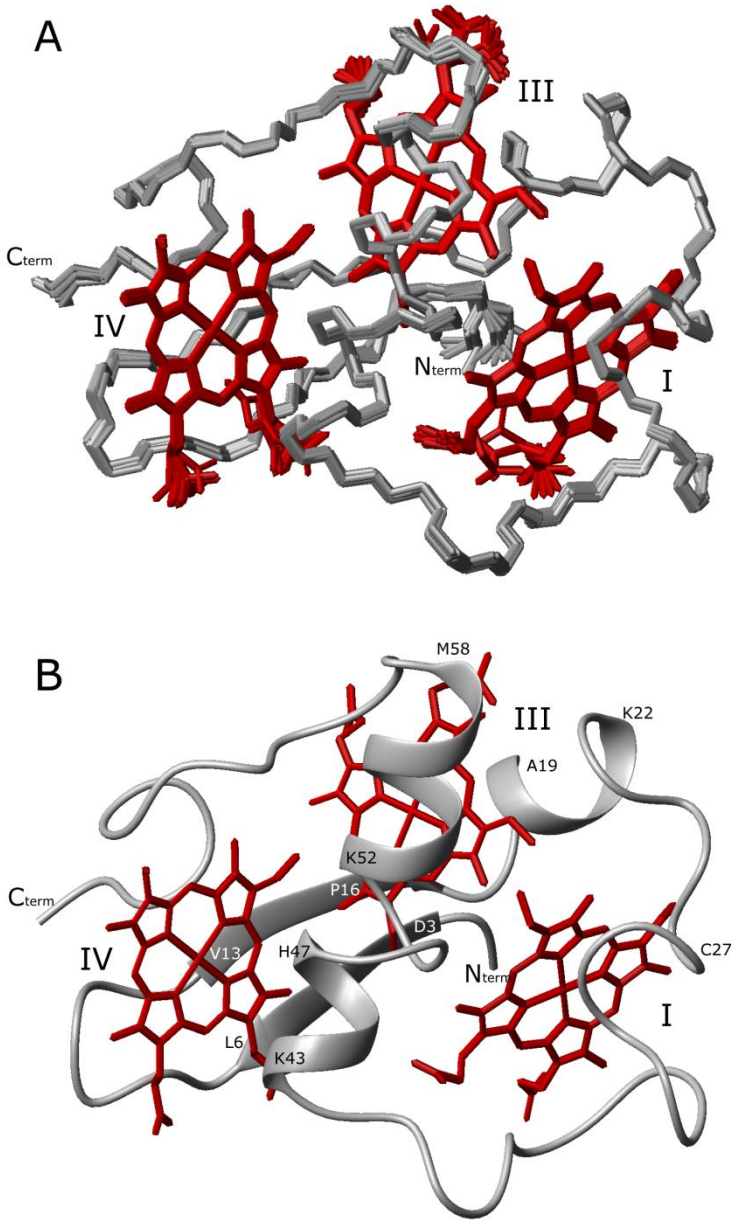

Figure 4.3 – PpcA solution structure. (A) Overlay of the 20 lowest energy NMR structures of PpcA at pH 7.1. Superimposition was performed using all the heavy-atoms. The peptide chain and the hemes are colored gray and red, respectively. (B) Ribbon diagram of PpcA lowest energy structure. Figures were produced using MOLMOL [5].

The structures superimpose with an average pairwise backbone (N-Cα-C') rmsd of 0.25 Å and a heavy atom rmsd of 0.99 Å (Figure 4.4). Thus, the backbone is very well defined and the amino acid side chains showing larger conformational variability correspond to regions with higher solvent exposure. In particular, the N- and the C-terminal ends are disordered.

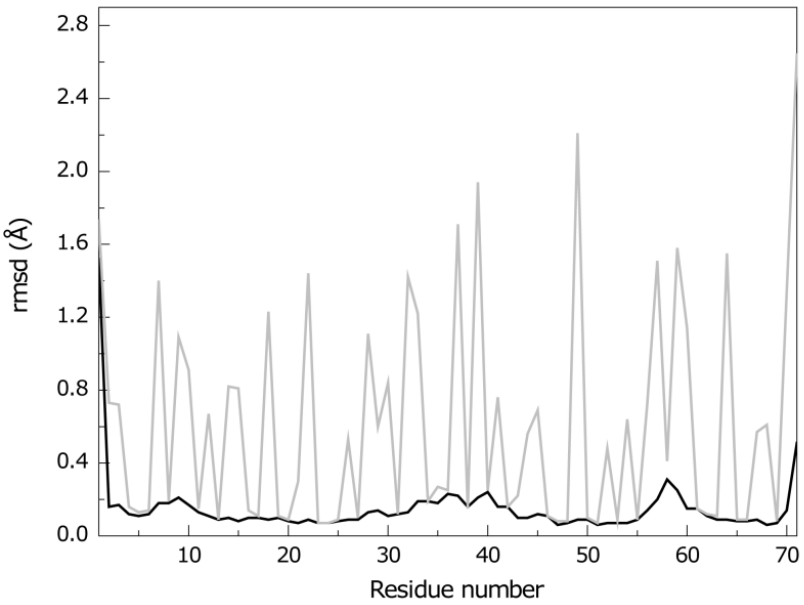

Figure 4.4 – Average pairwise backbone (gray) and heavy atom (black) rmsd values per residue of the family of 20 conformers obtained for PpcA solution structure.

The statistics for this family of structures is shown in Table 4.1. The Ramachandran plot shows 70.4% of the residues in the most favoured regions and 29% in the additionally allowed. A total of 35 hydrogen bonds were identified in the family of 20 structures with the software MOLMOL [5], 23 of which were present in at least 50% of the structures.

4.1.4 ^{15}N relaxation measurements

^{15}N NMR relaxation has been used to characterize the dynamic properties of reduced PpcA in solution. The relaxation parameters T_1, T_2 and NOE were determined at 600 and 800 MHz (Figure 4.5).

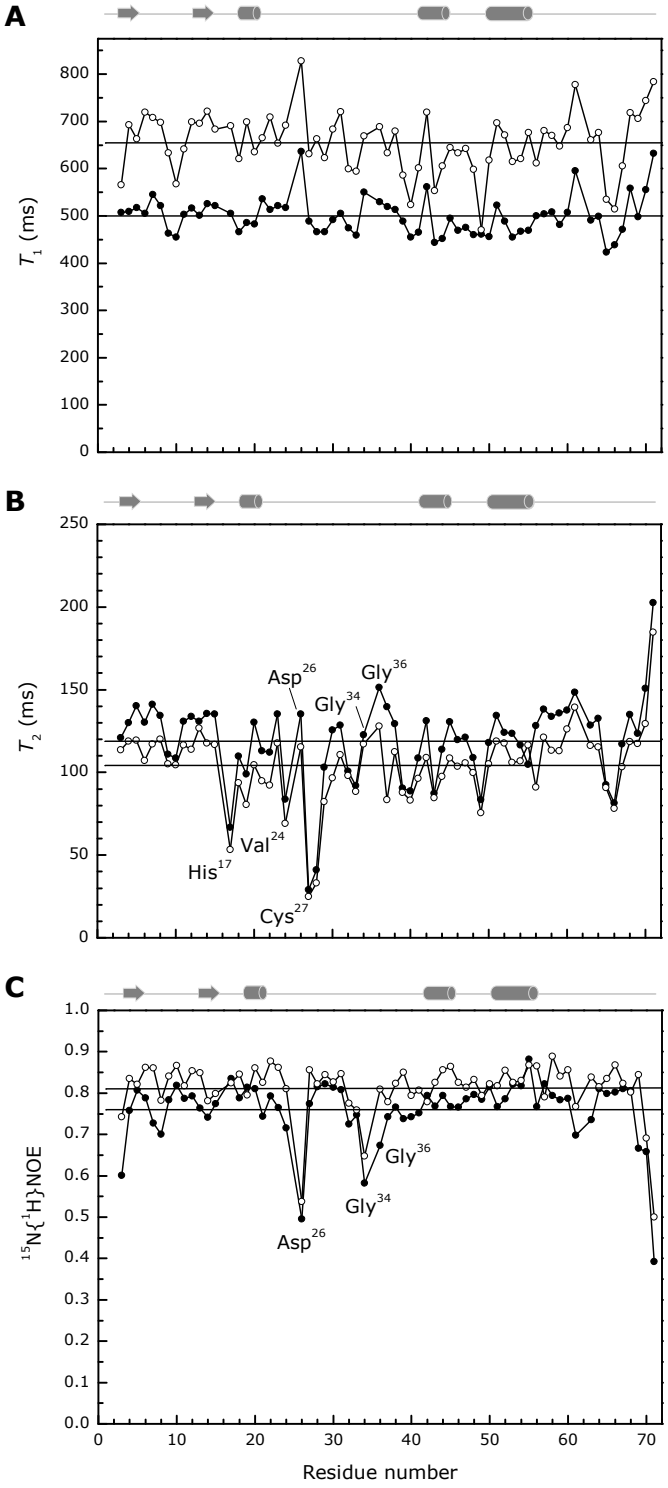

Figure 4.5 – ^{15}N relaxation parameters for PpcA backbone in the reduced state. (A) longitudinal T_1 relaxation times, (B) transverse T_2 relaxation times, and (C) ^{1}H-^{15}N heteronuclear NOEs. Solid straight lines represent the average T_1, T_2 and NOE at the respective magnetic field; open circles 800 MHz and closed circles 600 MHz. Secondary structure elements are shown as arrows (β-strands) and cylinders (α-helices).

Relaxation data were obtained for all residues except for proline residues (positions 16, 25, 35 and 62) and the two N-terminal amino acids Ala^{1} and Asp^{2}. The average values for T_1 are 500 and 655 ms and for T_2 values are 119 and 104 ms, at 600 and 800 MHz, respectively. The average NOE value is 0.76 at 600 MHz and 0.81 at 800 MHz. Good correlation was observed between structure and experimental relaxation data. Most residues in regular secondary structure elements exhibit heteronuclear NOE values close to the theoretical maximum indicating high rigidity in these regions (Figure 4.5). The overall differences in the T_1 values are not significant. Higher variability was clearly observed in the NOE and T_2 data. High T_2 values correlate with a decrease in the NOE ratio in positions Asp^{26}, Gly^{34}, Gly^{36} and the three residues at the C-terminus (positions His^{69}, Lys^{70} and Lys^{71}), which is in agreement with motions in the ns-ps time scale. Other regions of PpcA with low or average NOE values present lower T_2 values with respect to the mean. These correspond to residues His^{17}, Val^{24} and Cys^{27}, indicating that these residues are affected by conformational exchange processes in the μs-ms time scale.

4.1.5 pH titration

The pH titration of PpcA was carried out by ^{1}H-^{15}N HSQC NMR in the pH range 5.5-9.5 and all ^{1}H and ^{15}N chemical shifts of the polypeptide backbone (except for residues 1 and 2) and side chains were measured. To estimate the effects of pH changes on the PpcA solution structure, the average chemical shift differences ($\Delta\delta_{avg}$) of each amide were calculated as described by Garret and co-workers [6] (Figure 4.6).

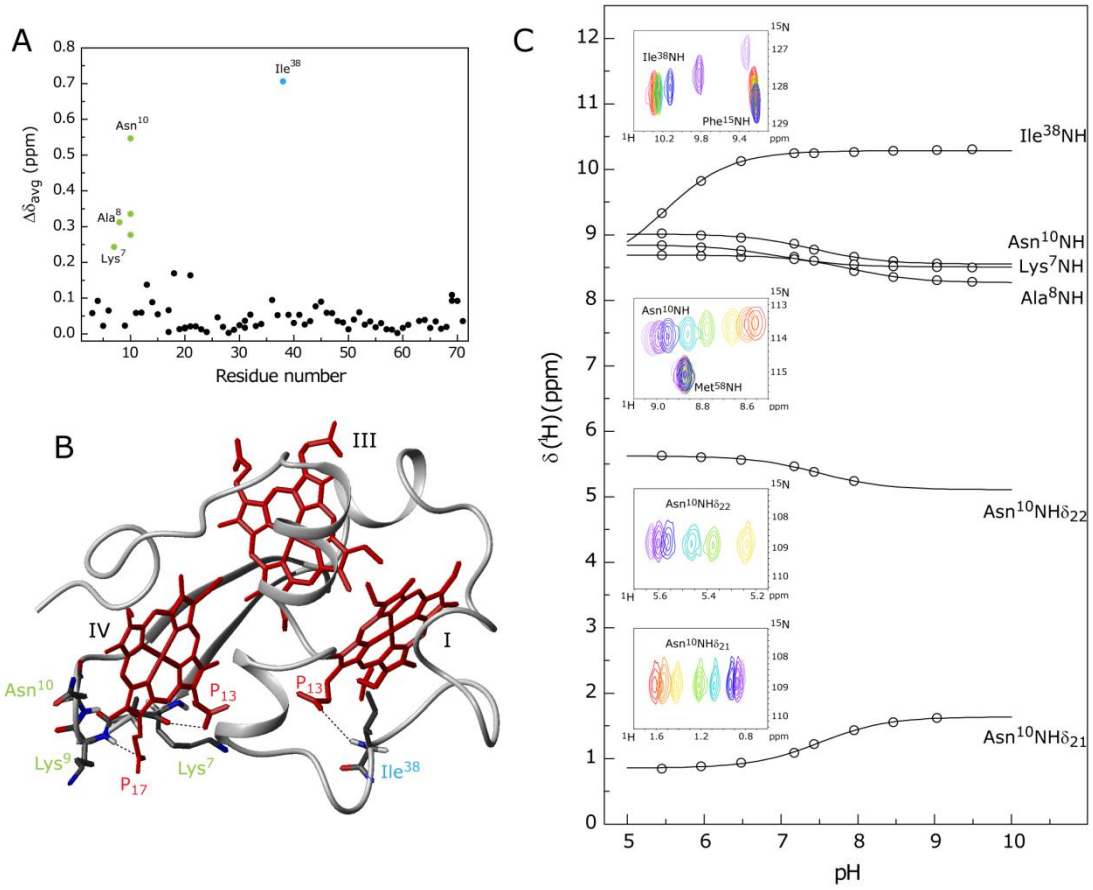

Figure 4.6 – pH-linked conformational changes in PpcA. (A) Weighted average of ^{1}H and ^{15}N chemical shifts ($\Delta\delta_{avg}$) between pH 5.5 and 9.5. (B) Mapping of the residues showing large pH-dependent shifts on PpcA solution structure. Residues that are close to the heme IV are indicated in green while Ile^{38} that forms a conserved hydrogen bond with P_{13}^{I} carboxyl oxygen is indicated in blue. Hemes groups are colored red. Dashed lines indicate hydrogen bonds. (C) pH titration data of the most affected PpcA amide signals. In the expansion of each ^{1}H-^{15}N-HSQC NMR spectrum pH increases from violet to pink. Lys^{7} and Ala^{8} backbone amide signals are not shown since they appear in a very crowded region of the spectra.

The residues whose NH signals indicated larger differences ($\Delta\delta_{avg}$ > 0.2 ppm) were from Lys^{7}, Ala^{8}, Asn^{10} and Ile^{38} backbone and also from Asn^{10} side chain (Figure 4.6A). These residues were mapped on the structure indicated in Figure 4.6B. The pH titration of the amide signals of Lys^{7}, Ala^{8}, Asn^{10} and Ile^{38} are indicated in Figure 4.6C. The NH signals of Lys^{7}, Ala^{8} and Asn^{10} have basic pK_a values of 7.0, 7.9 and 7.5 respectively, whereas that of Ile^{38} has a much more acidic pK_a (5.5). These pK_a values show that the pH-linked conformational changes have different origins.

4.2 Discussion

4.2.1 Comparison of PpcA solution structure with *Gsc*$_7$ crystal structures

In solution, the structure of the triheme cytochrome PpcA folds in a two-strand β-sheet at the N-terminus formed by Asp^3-Leu^6 and Val^{13}-Pro^{16} strands, followed by three α-helices between residues Ala^{19}-Lys^{22}, Lys^{43}-His^{47}, and Lys^{52}-Met^{58}. The three bis-histidinyl heme groups are arranged in a triangular way with hemes I and IV almost parallel with each other and both nearly perpendicular to heme III (Figure 4.3). This structure was compared with the crystal structures available for the *Gsc*$_7$ [1,7,8] and the solution structure of *Dac*$_7$ in the reduced state [9]. The parameters describing the heme geometry of PpcA in solution along with equivalent values for *Gsc*$_7$ crystal structures and cytochrome c_7 from *D. acetoxidans* (*Dac*$_7$) are presented in Table 4.2.

Table 4.2 – Heme geometry for *G. sulfurreducens* cytochromes c_7. The values for PpcA NMR reduced structure were obtained for the lowest energy structure. The values for the NMR solution structure of *Dac*$_7$ in the reduced state [9] are also included for the sake of completeness and are not discussed.

	NMR	Crystal structures[a]					NMR
	PpcA	**PpcA[b]**	**PpcB[c]**	**PpcC**	**PpcD[c]**	**PpcE**	**Dac$_7$[d]**
				Heme Fe-Fe distance (Å)			
I-III	11.7	11.2	11.7 (11.5)	11.2	11.2 (11.3)	11.8	11.9
I-IV	19.0	20.8	18.2 (18.8)	18.5	18.2 (18.2)	18.2	18.9
III-IV	12.6	12.6	12.6 (12.8)	12.6	12.6 (12.6)	12.4	12.5
				Angle between heme planes (°)			
I-III	82	86	73 (72)	81	78 (76)	71	41
I-IV	27	35	20 (16)	18	25 (24)	22	11
III-IV	74	69	70 (71)	75	72 (70)	72	56
				Angle between His planes (°)			
I	50	57	79 (88)	52	12 (3)	77	55
III	23	22	35 (36)	38	38 (22)	34	27
IV	80	89	75 (81)	86	85 (84)	89	53

[a] The values were taken from [8].

[b] The crystal structure of PpcA between hemes I and III is altered in comparison with the other *G. sulfurreducens* cytochromes c_7 due to the presence of the additive deoxycholate used in crystallization. It should not be used for structural comparisons.

[c] PpcB and PpcD cytochromes present two monomers in the crystal. The values corresponding to monomer B are given in parentheses.

[d] *Dac*$_7$ shares 46% sequence identity with PpcA and was extensively studied by Assfalg and co-workers [9,10] and Czjzek and co-workers [11].

With exception of the crystal structure of PpcA, for which the Fe-Fe distances and angles between the heme planes in the PpcA crystal structure are different due to the binding of the additive deoxycholate [8], the general fold and the relative positions of the three hemes are similar, with a good agreement between the consensus secondary structure elements identified in the NMR and crystal structures. The average Fe-Fe distances found among the crystal structures of PpcB, PpcC, PpcD and PpcE differ by less than 4% compared to those of PpcA solution structure (Table 4.2). Differences between the heme core in PpcA

solution and crystal structures were previously anticipated from the analysis of NOE interheme connectivities between hemes III and IV. Indeed, several unexpected connectivities were observed on basis of the distances taken from PpcA crystal structure (Chapter 3). The differences between the solution and crystal structures of PpcA are not just limited to the heme core but extend beyond. In particular, significant differences are observed in the polypeptide region between His^{17} and Glu^{39} that surrounds heme I.

On the other hand, the patterns of interheme NOE connectivities were identical to those observed for PpcB, which has the highest sequence identity with PpcA (77%), suggesting the same heme core arrangement for both proteins in solution. The comparison between the solution structure of PpcA and PpcB crystal structures (Figure 4.7) showed that the global rmsd values of the lowest energy NMR structure to molecule A and molecule B of PpcB in the unit cell are 1.22 Å and 1.12 Å for backbone atoms, respectively. These values are much lower than those found for the PpcA crystal structure, which are 2.25 Å for backbone and 3.10 Å for heavy atoms. The residual rmsd values between the mean solution structure and the crystal structures are plotted along the sequence in Figure 4.7A, showing the dissimilarity between the solution and crystal structures of PpcA.

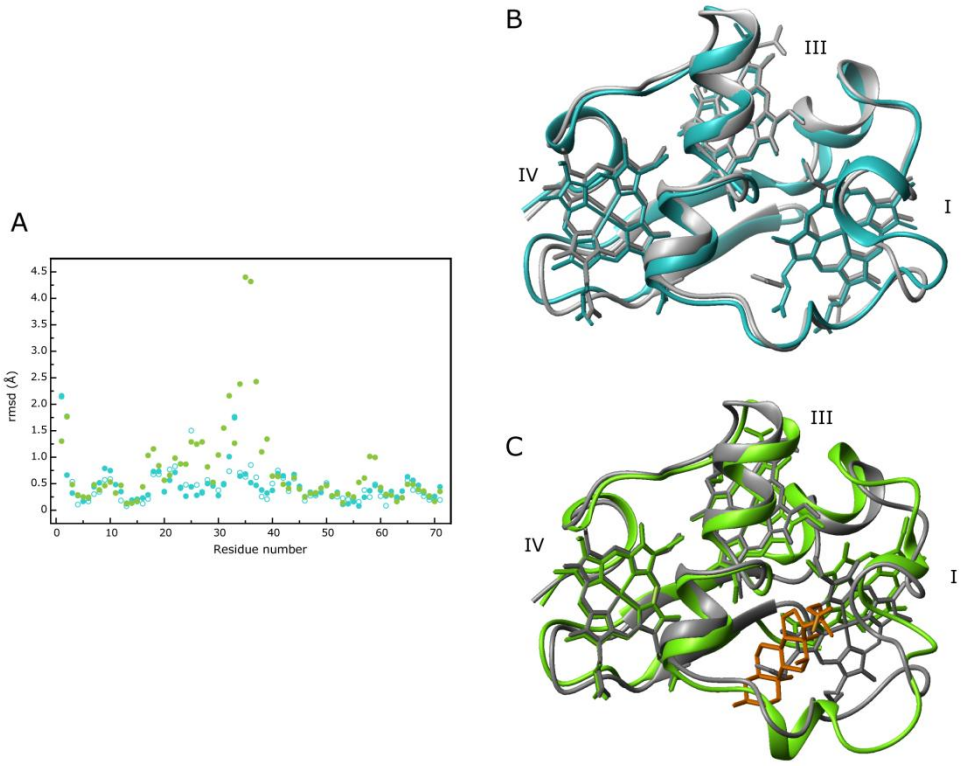

Figure 4.7 – Comparison of PpcA lowest energy solution structure with PpcA (PDB 1OS6) and PpcB crystal structures (monomers A and B, PDB 3BXU). Structures were superimposed in MOLMOL [5] using backbone atoms. (A) Average rmsd between each pair of structures. Green symbols represent PpcA crystal structure, and blue closed and open symbols represent PpcB monomers A and B, respectively. (B) PpcA solution structure *versus* PpcB crystal structure (monomer B). PpcA solution structure is colored light gray, and PpcB crystal structure is blue. (C) PpcA solution structure *vs.* PpcA crystal structure. PpcA solution structure is colored light gray, and PpcA crystal structure is green. The deoxycholate molecule used in the crystallization is represented in orange.

Among the four PpcA homologue crystal structures, significant structural differences were noted by Pokkuluri and co-workers [8], in particular, on the axial ligand orientations of heme I and the polypeptide region surrounding heme I (residues 16-40). The region around heme I is also where the sequences of Gsc_7 homologues differ the most suggesting a functional significance. In this region, the PpcA solution structure showed a non-regular helix forming a bulge between the two helical regions comprised of residues Lys^{43}-His^{47} and Lys^{52}-Met^{58}. This structural feature is similar to the crystal structures of PpcB and PpcC but not to those of PpcD and PpcE where a regular helix is formed in this region.

4.2.2 Backbone dynamics

The backbone dynamics obtained for PpcA corroborates the ordered nature of the protein, and confirms that the less defined regions of the molecule are the result of their intrinsic flexibility. The ^{15}N NMR relaxation experiments showed that the polypeptide segment between His^{17} and Cys^{27} that surrounds heme I has a dynamic behaviour that differs from rest of the protein. Interestingly, T_2 values in this region (below the mean value) point to the occurrence of exchange processes in the μs-ms time regime (Figure 4.5). Dynamics in this time scale have been postulated to be essential for the recognition and interaction between protein molecules [12], what suggests that this could be an interaction surface of PpcA with other proteins. In fact, the detailed thermodynamic characterization of PpcA hinted that heme I and IV might have a role in recognition of PpcA redox partners [13]. The proposed functional redox-cycle for PpcA involves two dominant microstates: a microstate in the one-electron oxidized protein with heme I oxidized while keeping the redox-Bohr center protonated (P_{1H}) and another in the two-electron oxidized protein with hemes I and IV oxidized and deprotonated redox-Bohr center (P_{14}). Since heme I is oxidized in the two functional microstates, it is most likely that the heme I region of PpcA interacts with its electron acceptor. Heme IV, which alters its oxidation state between the one-and two-electron oxidized protein, is very likely the interaction region with the electron donor. However, in contrast with the region around heme I, no backbone dynamics effects were detected around heme IV. This behavior is not completely unexpected as there are some examples of rigid protein recognition sites [14,15]. The lack of dynamics has been suggested as a requisite for the selective sequence recognition. Structurally, heme IV is stabilized by hydrogen bonds to both propionate groups (see below), restricting the backbone dynamics around this heme. This is in line with the fact that, in the crystal structures of the entire family of Gsc_7 [8], the region around heme I varies significantly but that around heme IV is highly conserved, probably reflecting the higher structural rigidity in this region.

4.2.3 Heme reduction potentials and redox interactions

The detailed thermodynamic properties of PpcA redox centers were determined (Chapter 3) and are summarized in Table 4.3.

Table 4.3 – Heme reduction potentials and pairwise interactions (mV) of the fully reduced and protonated forms of PpcA. The standard errors are given in parentheses.

Heme redox potentials			Redox interactions			Redox-Bohr interactions		
I	III	IV	I-III	I-IV	III-IV	I-H	III-H	IV-H
-154(5)	-138(5)	-125(5)	27(2)	16(3)	41(3)	-32(4)	-31(4)	-58(4)

The solution structure determined allowed addressing the structural basis for PpcA redox properties. The heme negative reduction potentials are expected for relatively exposed *c*-type hemes with bis-histidine axial coordination. The heme solvent exposures are 231.7, 215.8, and 171.3 $Å^2$ for hemes I, III and IV respectively, and the reduction potential values of the heme groups correlate with their solvent exposure. In fact, the more exposed hemes (heme I and III) have more negative reduction potentials (-154 and -138 mV, respectively) whereas the least exposed one (heme IV) has the least negative reduction potential value (-125 mV). The higher reduction potential of the latter is also reinforced by its substantial positive environment due to the presence of several neighboring lysine residues that stabilize the reduced state of heme IV.

The heme reduction potentials are also modulated by heme-heme redox interactions. The positive values obtained for these interactions suggest that they are dominated by electrostatic effects, rather than conformational changes between redox stages. This is confirmed by the fact that the highest (41 mV) and the lowest (16 mV) redox interaction are observed between the closest (III-IV) and furthest (I-IV) pair of heme groups.

4.2.4 Structural close-up on PpcA redox-Bohr center: pH-linked conformational changes

In addition to the heme-heme redox interactions, the heme reduction potentials are modulated by redox-Bohr interactions. The redox-Bohr interaction for heme IV is twice as high as compared to that of the other two hemes (Table 4.3), suggesting that the redox-Bohr center is located in the vicinity of heme IV. In fact, the redox-Bohr center was previously assigned to heme IV propionate 13 (Chapter 3). The redox-Bohr effect, as observed for PpcA, is crucial for coupling electron and proton transfer at physiological pH. The detailed thermodynamic characterization of this triheme cytochrome indicated that such coupling involves the two microstates P_{1H} and P_{14} [13]. Thus, a fraction of the energy associated with electrons received from the donor by microstate P_{1H} is used by the protein to lower the pK_a value of the redox-Bohr center so that protons can be released in the periplasm at physiological pH. This mechanism would imply structural conformational changes in the neighborhood of the redox-Bohr center.

The solution structure determined confirms P_{13}^{IV} as the redox-Bohr center and allows for the first time mapping the pH-linked conformational changes associated with the protonation/deprotonation of this center. The backbone NH signals of Lys^{7}, Ala^{8}, Asn^{10} and Ile^{38}, and from Asn^{10} side chain are the most affected by the protonation/deprotonation of the redox-Bohr center (Figure 4.6). Residues 7, 8 and 10 are part of the β-turn segment connecting the two-strand β-sheet near heme IV, whereas Ile^{38} is a fully conserved residue within the family of Gsc_7 and protects heme I and axial His^{31} from solvent exposure.

The amide proton of Ile^{38} forms a conserved hydrogen bond with the carboxyl oxygen of P_{13}^{I} in the crystal structures of the entire family of Gsc_7 [8]. This hydrogen bond is not seen in PpcA solution structure probably due to the flexibility of the propionate groups of heme I. However, at lower pH values, the proton chemical shift of the Ile^{38} NH signal decreases significantly suggesting the disruption of a hydrogen bond formed between the amide proton of Ile^{38} and the carboxyl oxygen of P_{13}^{I} upon protonation of the latter (Figure 4.6C).

The pK_a values obtained for the NH signals of Lys^{7}, Ala^{8} and Asn^{10} correlate with the pK_a value of the redox-Bohr center (8.6) previously determined for the fully reduced and protonated protein (Chapter 3), and is likely to be caused by the protonation/deprotonation of the redox-Bohr center (P_{13}^{IV}). The differences of the pK_a values obtained for the redox-Bohr center and those described from the analysis of the amide backbone NMR signals of Lys^{7}, Ala^{8}, Asn^{10} are expected since the former value was derived from the global thermodynamic analysis of the properties of the redox-centers and may reflect the combined contribution of fractional protonation of several acid-base groups [16].

Although being also part of the β-turn segment connecting the two-strand β-sheet, no significant changes on the NH backbone signal were observed for residue Lys^{9}. The most likely explanation for this resides is the conserved hydrogen bond between the Lys^{9} backbone NH and the O2 atom of P_{17}^{IV}. Indeed, P_{17}^{IV} is exposed to surface (44.1 $Å^2$ for carboxyl oxygens) and would have nearly the same pK_a of a free propionate group (~4.0). Therefore, in the pH range studied it remains deprotonated and forms the hydrogen bond with Lys^{9} backbone NH.

The pH-linked conformational changes observed in the neighborhood of P_{13}^{IV} and the structural features around this group help to rationalize the redox-Bohr effect observed in PpcA. P_{13}^{IV} is considerably less exposed to solvent than P_{17}^{IV} (16.3 $Å^2$ and 44.1 $Å^2$, respectively) and thus would be very sensitive to the conformation of the protein surroundings depending on its protonation state. Being shielded from the solvent, the protonated form is stabilized which explains the pK_a of the redox-Bohr center well above its expected pK_a in free solution (~4.0). Furthermore, in the solution structure of PpcA, the carbonyl oxygen of Lys^{7} in the β-turn (residues 7-12) is within hydrogen bonding distance from P_{13}^{IV} (2.6 Å between Lys^{7}O and heme IV P_{13} O1 in the lowest energy structure). Thus, deprotonation of the propionate P_{13}^{IV} disrupts the hydrogen bond with Lys^{7} leading to structural changes in the neighborhood as a function of pH. This is likely to be the origin of pH-linked conformational changes in the β-turn as the above mentioned contact is not favoured when this buried propionate is deprotonated.

4.3 Conclusions

The structure of PpcA constitutes the first solution structure of a cytochrome from *G. sulfurreducens*. The polypeptide fragment formed by residues 17-27 located near heme I of PpcA was identified as the most dynamic segment by analysis of the ^{15}N relaxation parameters obtained for the backbone. This segment may be involved in interaction with other molecules. The analysis of the chemical shift variation of the backbone and side chain amide signals with pH allowed mapping the pH-linked conformational changes caused by protonation/deprotonation of the redox-Bohr center, which is now confirmed to be the heme propionate P_{13}^{IV}. The redox-Bohr effect of PpcA is a crucial property that allows it to perform a concerted e^-/H^+ transfer and to contribute to the proton electrochemical gradient across the bacterial cytoplasmic membrane that drives ATP synthesis.

It was confirmed that the crystal structure of PpcA in the oxidized state is affected by the presence of the deoxycholate molecule used in the crystallization. Therefore, in order to study possible redox-linked conformational changes, the PpcA solution structure in the oxidized state should be determined.

The solution structure of PpcA will also be used to assist in the rational design of mutants and in the mapping of interaction sites with redox partners, an essential step towards engineering variants of *G. sulfurreducens* with increased respiratory rates and the concomitant improvement in their biotechnological applications.

4.4 References

[1] PR Pokkuluri, YY Londer, NE Duke, WC Long, M Schiffer (2004) Family of cytochrome c_7-type proteins from *Geobacter sulfurreducens*: structure of one cytochrome c_7 at 1.45 Å resolution, Biochemistry 43, 849-859.

[2] DL Turner, CA Salgueiro, J LeGall, AV Xavier (1992) Structural studies of *Desulfovibrio vulgaris* ferrocytochrome c_3 by two-dimensional NMR, Eur J Biochem 210, 931-936.

[3] DL Turner, L Brennan, SG Chamberlin, RO Louro, AV Xavier (1998) Determination of solution structures of paramagnetic proteins by NMR, Eur Biophys J 27, 367-375.

[4] P Güntert, W Braun, K Wüthrich (1991) Efficient computation of three-dimensional protein structures in solution from nuclear magnetic resonance data using the program DIANA and the supporting programs CALIBA, HABAS and GLOMSA, J Mol Biol 217, 517-530.

[5] R Koradi, M Billeter, K Wuthrich (1996) MOLMOL: a program for display and analysis of macromolecular structures, J Mol Graph 14, 51-55, 29-32.

[6] DS Garrett, YJ Seok, A Peterkofsky, GM Clore, AM Gronenborn (1997) Identification by NMR of the binding surface for the histidine-containing phosphocarrier protein HPr on the N-terminal domain of enzyme I of the *Escherichia coli* phosphotransferase system, Biochemistry 36, 4393-4398.

[7] L Morgado, M Bruix, V Orshonsky, YY Londer, NE Duke, X Yang, PR Pokkuluri, M Schiffer, CA Salgueiro (2008) Structural insights into the modulation of the redox properties of two *Geobacter sulfurreducens* homologous triheme cytochromes, Biochim Biophys Acta 1777, 1157-1165.

[8] PR Pokkuluri, YY Londer, X Yang, NE Duke, J Erickson, V Orshonsky, G Johnson, M Schiffer (2010) Structural characterization of a family of cytochromes c_7 involved in Fe(III) respiration by *Geobacter sulfurreducens*, Biochim Biophys Acta 1797, 222-232.

[9] M Assfalg, L Banci, I Bertini, M Bruschi, MT Giudici-Orticoni, P Turano (1999) A proton-NMR investigation of the fully reduced cytochrome c_7 from *Desulfuromonas acetoxidans*. Comparison between the reduced and the oxidized forms, Eur J Biochem 266, 634-643.

[10] M Assfalg, L Banci, I Bertini, M Bruschi, P Turano (1998) 800 MHz ^{1}H NMR solution structure refinement of oxidized cytochrome c_7 from *Desulfuromonas acetoxidans*, Eur J Biochem 256, 261-270.

[11] M Czjzek, P Arnoux, R Haser, W Shepard (2001) Structure of cytochrome c_7 from *Desulfuromonas acetoxidans* at 1.9 Å resolution, Acta Crystallogr D Biol Crystallogr 57, 670-678.

[12] AM Mandel, M Akke, AG Palmer, 3rd (1995) Backbone dynamics of *Escherichia coli* ribonuclease HI: correlations with structure and function in an active enzyme, J Mol Biol 246, 144-163.

[13] L Morgado, M Bruix, M Pessanha, YY Londer, CA Salgueiro (2010) Thermodynamic characterization of a triheme cytochrome family from *Geobacter sulfurreducens* reveals mechanistic and functional diversity, Biophys J 99, 293-301.

[14] JM Pérez-Cañadillas, M Guenneugues, R Campos-Olivas, J Santoro, A Martinez del Pozo, JG Gavilanes, M Rico, M Bruix (2002) Backbone dynamics of the cytotoxic ribonuclease α-sarcin by ^{15}N NMR relaxation methods, J Biomol NMR 24, 301-316.

[15] D Fushman, S Cahill, D Cowburn (1997) The main-chain dynamics of the dynamin pleckstrin homology (PH) domain in solution: analysis of ^{15}N relaxation with monomer/dimer equilibration, J Mol Biol 266, 173-194.

[16] BM Fonseca, IH Saraiva, CM Paquete, CM Soares, I Pacheco, CA Salgueiro, RO Louro (2009) The tetraheme cytochrome from *Shewanella oneidensis* MR-1 shows thermodynamic bias for functional specificity of the hemes, J Biol Inorg Chem 14, 375-385.

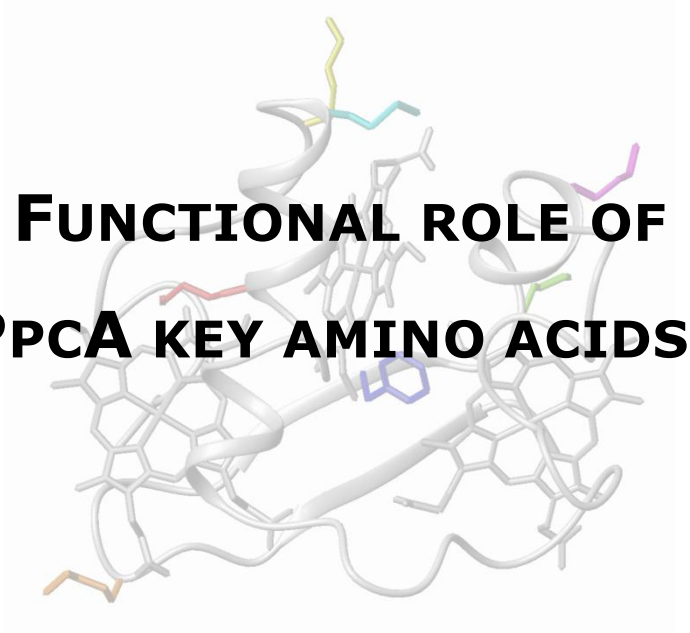

FUNCTIONAL ROLE OF PPCA KEY AMINO ACIDS[3]

[3] Partially reproduced from JM Dantas, L Morgado, YY Londer, AP Fernandes, RO Louro, PR Pokkuluri, M Schiffer, CA Salgueiro (2012) Pivotal role of the strictly conserved aromatic residue F15 in the cytochrome c_7 family, J Biol Inorg Chem 17, 11-24(http://dx.doi.org/10.1007/s00775-00011-00821-00778), according to the Editor's Copyright Policy.

5. FUNCTIONAL ROLE OF PPCA KEY AMINO ACIDS

PpcA is a member of the *G. sulfurreducens* cytochrome c_7 family that has the necessary thermodynamic properties to perform e^-/H^+ energy transduction in addition to the electron transfer that leads to the reduction of extracellular electron acceptors.

To elucidate the physiologic function of PpcA individual key residues, a family of mutants covering the entire protein was prepared using site-directed mutagenesis.

The redox properties of PpcA mutants were characterized using NMR and UV-visible spectroscopy. The comparison of the results obtained for the wild-type and mutant proteins showed that the fine tuning of PpcA redox networks is crucial to the energy transduction mechanism.

5.1 Results and discussion

As discussed in Chapter 3, several factors affect and control the reduction potentials of heme groups in a multiheme protein [1-3]. Besides the nature of the heme axial ligands, the solvent exposure, as well as the size, polarity and charge of neighboring residues are also important factors for the regulation of heme reduction potentials [4].

In order to monitor in detail the function of individual residues in PpcA, a collection of single-mutated proteins was prepared. The PpcA mutants collection comprises 17 single-mutated proteins, which were expressed and purified as the wild-type protein (Chapter 2).

The mutant proteins belong to three different structural classes: (i) conserved hydrophobic residue Phe^{15}; (ii) residue Met^{58} that protects heme III from solvent exposure; and (iii) lysine residues near the hemes (conserved Lys^{18} between hemes I and III, Lys^{22} also between hemes I and III, Lys^{60} near heme III, and Lys^{9} and Lys^{52} near heme IV). No mutations were performed in the position of the axial ligands.

The mutated residues are mapped in PpcA solution structure model depicted in Figure 5.1.

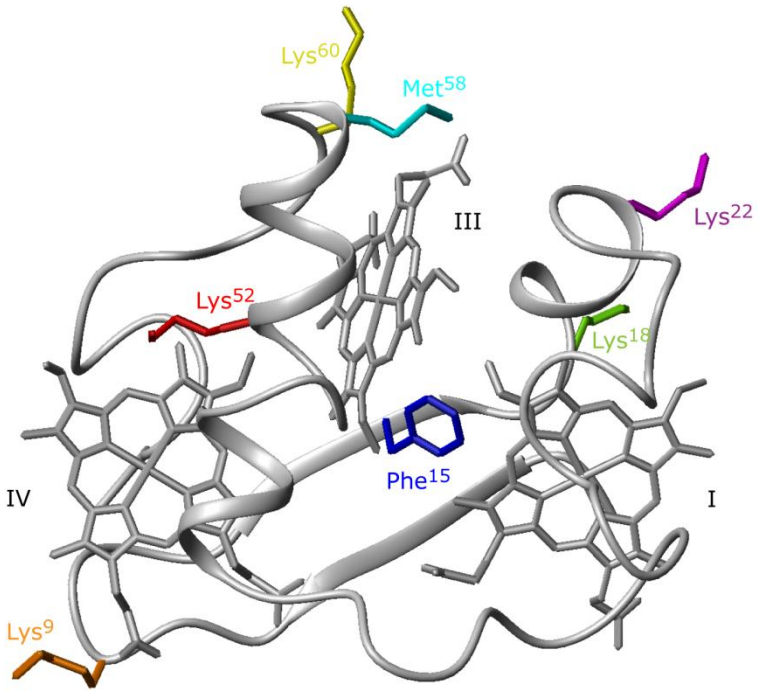

Figure 5.1 – Spatial localization of the mutated residues in PpcA solution structure (PDB 2LDO [5]). Backbone ribbon and heme groups are represented in gray. Mutated residues are highlighted and labeled in different colors.

For each mutant, the heme signals in the reduced state were identified and the heme oxidation profiles screened by 2D-EXSY NMR at pH 6 and pH 8. For those that showed significant differences when compared with the wild-type, the detailed thermodynamic characterization was carried out as described for the wild-type protein (Chapter 3).

5.1.1 Conserved Phe^{15} residue

A particular structural arrangement is formed by heme I, heme III, and the amino acid phenylalanine 15 (Phe^{15}) and is present in all cytochromes c_7 (Figure 1.2 – Chapter 1). An equivalent arrangement is also observed in tetraheme cytochromes c_3 [6], as well as in cytochrome c_7-type domains [7]. Therefore, the nature of this amino acid side chain and its particular spatial location might have an important structural/functional role within these proteins.

In PpcA, the residue Phe^{15} is located in a hydrophobic region between hemes I and III, with the aromatic ring located close to heme I and almost parallel to the ring plane of this heme. The Phe^{15} ring plane is also parallel to the imidazole ring of heme III axial histidine (His^{20}) and perpendicular to heme III (Figure 5.2). The conserved Phe^{15} residue is immobilized between hemes I and III, and therefore its free rotation is impaired. Consequently, the aromatic ring has a conserved orientation within this structural motif.

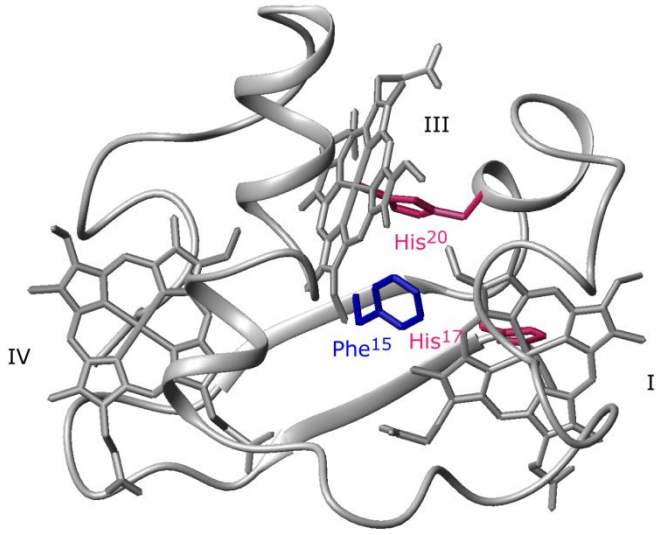

Figure 5.2 – Spatial localization of residue Phe^{15} in PpcA solution structure. The side chains of heme I and III axial histidines His^{17} and His^{20} are also represented.

In a previous study, the Phe^{15} residue was replaced by the aromatic tryptophan and tyrosine residues using site-directed mutagenesis and their effect on the global (macroscopic) redox properties of the *G. sulfurreducens* cytochrome c_7 PpcA were evaluated [6]. However, the severe broadness of the NMR signals in tyrosine (PpcAF15Y) and tryptophan (PpcAF15W) mutants prevented the study of the individual heme redox properties. In fact, the 1D-^{1}H NMR features of PpcAF15Y and PpcAF15W showed major differences in relation to those of the wild-type protein. In the case of PpcAF15Y, the 1D-^{1}H NMR spectrum obtained for the fully oxidized protein showed extremely broad signals, whereas for PpcAF15W signal broadness is observed in both reduced and oxidized 1D-^{1}H NMR spectra (Figure 5.3).

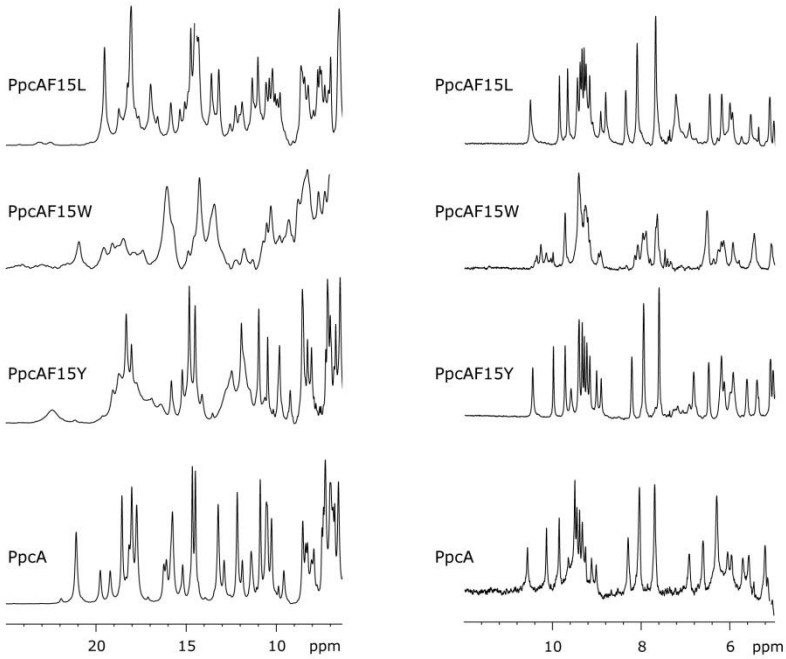

Figure 5.3 – Expansions of the 1D-^{1}H-NMR low-field regions obtained for PpcA and PpcA mutants. Left and right panels correspond to the oxidized and reduced forms, respectively.

The NMR signal broadness observed in the two mutants is very likely a consequence of the coexistence of more than one protein conformation in solution. These NMR features indicate that the location of Phe^{15} in the 3D structure imposes severe restrictions on the nature of the residues by which it can be replaced. In fact, the larger volume of the tryptophan residue (228 Å^3), compared with the phenylalanine volume (190 Å^3), and the side-chain polar character of a residue with similar size, which is the case for tyrosine (194 Å^3), leads to important conformational heterogeneity in solution of PpcAF15Y and PpcAF15W mutants. This is also in line with the fact that these mutants could not be crystallized despite extensive efforts (Pokkuluri and Schiffer unpublished results). In such conditions, exchange connectivities between all redox stages of the protein were not detected in the 2D-EXSY NMR spectra, preventing monitoring the stepwise oxidation of PpcAF15Y and PpcAF15W individual hemes and therefore their detailed thermodynamic characterization.

Thus, to probe the role of Phe^{15}, the mutant where this residue was replaced by the amino acid leucine was studied. Although both phenylalanine and leucine residues are hydrophobic and of similar size, they have different properties: phenylalanine is an aromatic residue, while leucine is aliphatic. In contrast to the mutants PpcAF15Y and PpcAF15W, in the case of PpcAF15L, the 1D-^{1}H NMR spectra are well resolved both for the reduced form and for the oxidized form (Figure 5.3). Thus, no evidence was found for the presence of multiple conformations. A direct comparison of the 1D-^{1}H NMR spectra obtained for PpcAF15L and the wild-type proteins showed that the distributions of the signals in the reduced spectra are similar, whereas in the oxidized state they are considerably different (Figure 5.3). This is particularly noticeable in the low-field region of the spectra (22–10 ppm), where signals of several heme methyl groups can be identified.

5.1.1.1 Heme core architecture and overall structure in the reduced form

^{1}H-^{15}N-HSQC NMR experiments were used to fingerprint the overall structure of PpcAF15L and to evaluate the impact of the mutation on the protein conformation. All backbone amide residues, except for the first two residues, were assigned for the wild-type protein (Chapter 4) and the same method was used to assist in the assignment of PpcAF15L signals. Comparison of the ^{1}H-^{15}N-HSQC NMR spectra obtained for wild-type and mutant proteins shows that the overall fold is maintained in the mutant (Figure 5.4).

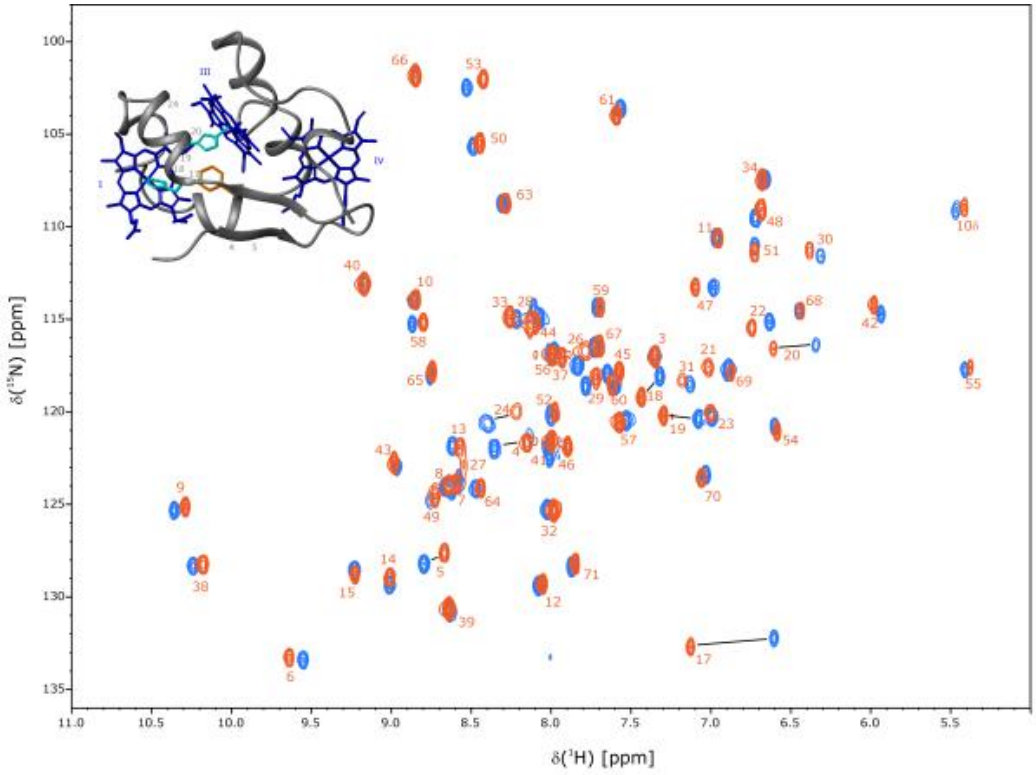

Figure 5.4 – Expansion of 2D ^{1}H-^{15}N HSQC NMR spectra of PpcAF15L (orange contours) and PpcA (blue contours) in the reduced form. The most affected amide signals are linked by a straight line in the spectrum and the position of the corresponding residues is indicated on the structure in the inset.

The backbone amide signal of residue 15 in both proteins overlaps, indicating that no changes in the protein backbone were introduced by the mutation. The most affected signal corresponds to the amide signal of His^{17}, followed by that of His^{20}. These residues are the distal axial ligands of hemes I and III and form, together with the residue 15 side chain, the hydrophobic region between these heme groups (Figure 5.1). The signals of Ile^{4}, Val^{5}, Lys^{18}, Ala^{19}, and Val^{24} were also affected, although to a smaller extent (Figure 5.4). The polypeptide segment between His^{17} and His^{20} is part of the α-helix located between hemes I and III (Figure 5.2), whereas Val^{24} is placed in a turn immediately after the α-helix. Residues Ile^{4} and Val^{5} are opposite to residue 15 in the two-stranded antiparallel β-sheet at the N-terminus formed by Asp^{3}-Leu^{6} and Val^{13}-Pro^{16} strands. Thus, the substitution of the Phe^{15} residue by a leucine has a local effect by rearranging the neighboring residues without affecting the global fold of the protein.

The evaluation of the impact of the replacement of the Phe[15] residue by a leucine was further extended to the study of the heme core architecture. 2D-^{1}H-NOESY and TOCSY data were acquired to assist in the assignment of the PpcAF15L heme proton signals, to identify the interheme NOE connectivities, and to probe the heme core architecture in solution. The assignment of the heme signals in PpcAF15L (Table A.3 – Appendix) was obtained using the same method as described for PpcA. This assignment was further confirmed by examining the interheme NOE connectivities measured from the 2D-^{1}H-NOESY NMR spectra acquired at different mixing times. The same set of interheme NOE connectivities between heme substituents of the closest heme groups observed in the wild-type cytochrome were identified in the mutant, which indicates that the heme core architecture is conserved in both proteins (Figure 5.5).

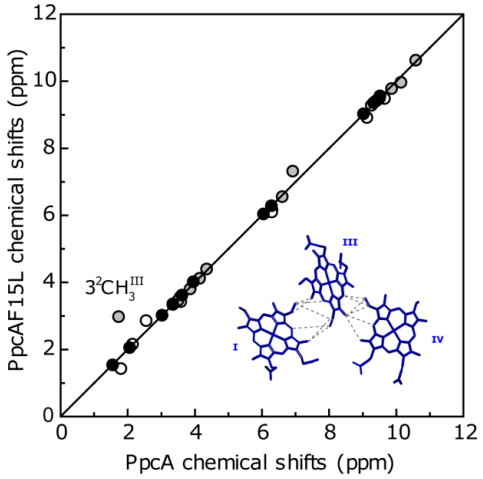

Figure 5.5 – Comparison of the observed heme proton chemical shifts of reduced PpcAF15L and those of PpcA at pH 8 and 15 °C. White, gray, and black circles correspond to hemes I, III, and IV, respectively. The solid line has a unit slope. The rmsd between the chemical shifts measured for PpcAF15L and those of PpcA are 0.18 (heme I), 0.39 (heme III), and 0.03 ppm (heme IV). The interheme NOE connectivities are indicated by dashed lines in the inset.

Also, a good correlation was obtained between the proton chemical shifts of the heme substituents measured for PpcAF15L and for PpcA, further confirming that the solution structures of the heme cores are similar (Figure 5.5). With the exception of the group $3^2CH_3^{III}$, which in PpcA is close to the aromatic ring of Phe[15] and hence subject to additional ring-current effects on its chemical shift, all other signals are essentially unaffected in the mutated protein. The best correlation was obtained for the heme IV protons, which is expected since heme IV is farthest from Phe[15] (Figure 5.2).

5.1.1.2 Preliminary screening of the heme oxidation profiles

As a first approach, the redox properties of the mutated protein were studied by 2D-EXSY NMR at pH 6 and pH 8 for the same set of heme methyls used in the wild-type protein

($12^{1}CH_3^{I}$, $7^{1}CH_3^{III}$ and $12^{1}CH_3^{IV}$). The results obtained for PpcAF15L are presented in Figure 5.6.

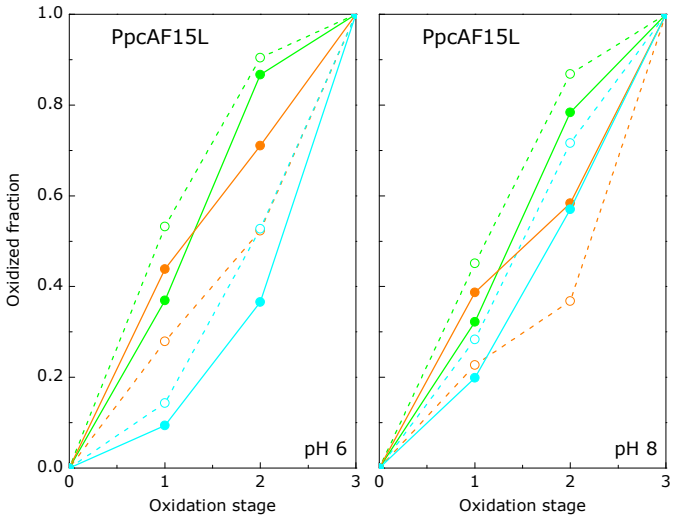

Figure 5.6 – Oxidation fraction of PpcAF15L (solid symbols and lines) and PpcA (open symbols and dashed lines) at pH 6 and pH 8. Heme I, III and IV data are colored in green, orange and blue, respectively. The heme oxidation fractions were calculated according to Equation 3.1 (Chapter 3).

In these plots, the lines with larger slope connecting two consecutive oxidation stages correspond to the heme that dominates the protein oxidation in that oxidation step. For the wild-type protein, at pH 6 the two first oxidation stages are dominated by the oxidation of heme I, while hemes III and IV are oxidized to a similar extent in the last step (dashed lines on the left panel of Figure 5.6). At pH 8 the order of heme oxidation for PpcA is I-IV-III (dashed lines on the right panel of Figure 5.6). In the mutated protein, hemes III and I dominate the first oxidation stage with similar oxidation fractions at both pH values (solid lines on Figure 5.6). Heme IV is the last to oxidize in the mutated protein, in contrast with what is shown for the wild-type protein. As a consequence of the replacement of Phe^{15} by a lysine residue significant changes were observed and thus, PpcAF15L was thermodynamically characterized in detail.

5.1.1.3 Thermodynamic characterization of PpcAF15L

To probe the functional role of residue Phe[15] in the control of the heme reduction potentials and in the global network of cooperativities of the wild-type protein, 2D-EXSY NMR spectra were obtained for PpcAF15L. The NMR spectra were obtained at different pH values and the chemical shifts of heme methyls $12^1CH_3^I$, $7^1CH_3^{III}$, and $12^1CH_3^{IV}$ were measured for oxidation stages 1–3 (Figure 5.7).

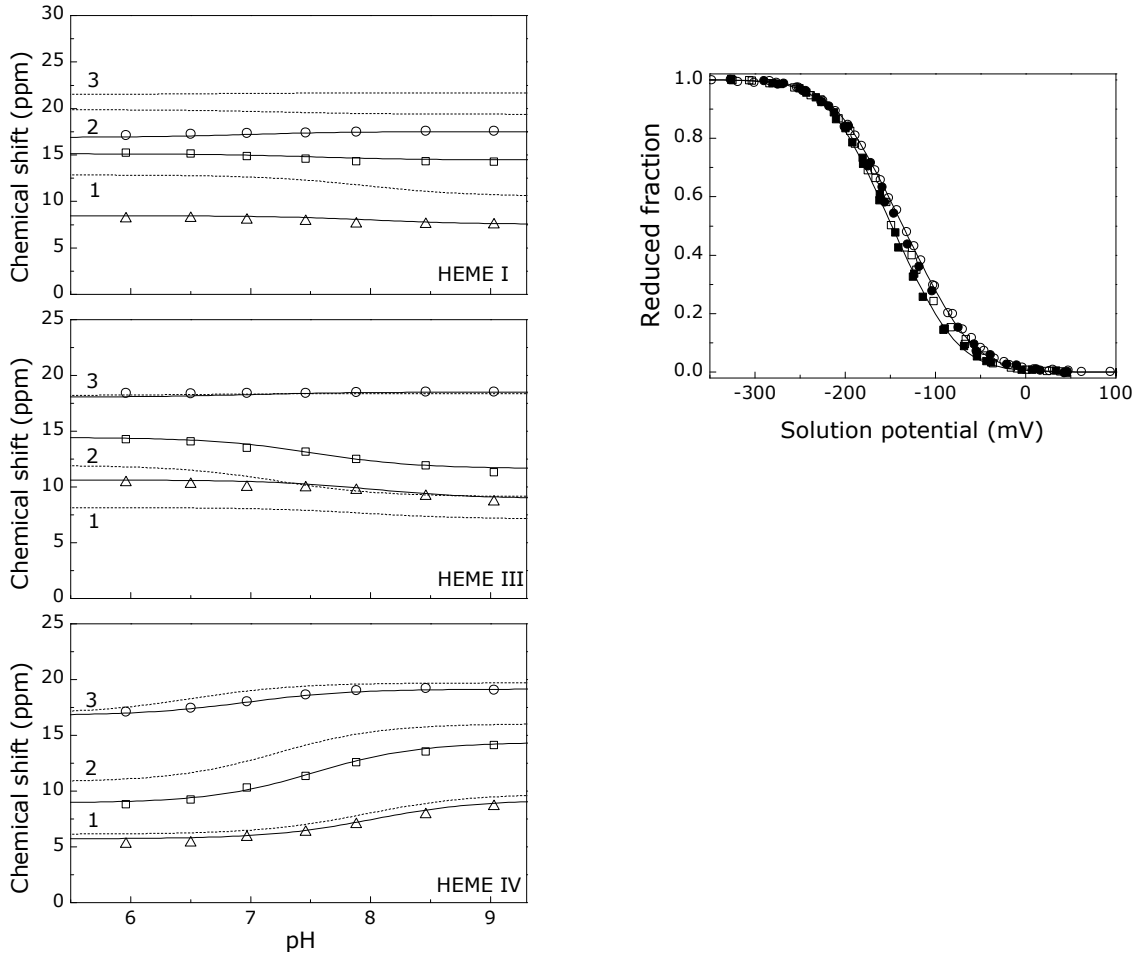

Figure 5.7 – Fitting of the thermodynamic model to the experimental data for PpcAF15L. The solid lines are the result of the simultaneous fitting of the NMR and UV-visible data. The three left panels show the pH dependence of heme methyl chemical shifts at oxidation stages 1 (△), 2 (□), and 3 (○). The chemical shifts of the heme methyls in the fully reduced stage (stage 0) are not plotted since they are unaffected by the pH. The dashed lines in each panel represent the best fit for the wild-type protein and the nearest label (1, 2, 3) indicates the oxidation stage represented by the curve. The right panel corresponds to the reduced fractions determined by UV-visible spectroscopy at pH 7.0 (○) and pH 8.0 (□). The open symbols and the filled symbols represent the data points in the reductive and oxidative titrations, respectively.

The chemical shifts of PpcAF15L heme methyl $12^1CH_3^I$ are considerably smaller in oxidation stages 1, 2, and 3, and are essentially unaffected in the reduced state (2.86 and 2.55 ppm in the mutant and wild-type protein, respectively). However, such variations do not translate into significant changes in heme I oxidation fractions, as they are determined in relation to the chemical shift in oxidation stage 3. Although to a much smaller extent, the

same situation was observed for heme methyl $12^{1}CH_3^{IV}$. In contrast, the chemical shifts of heme methyl $7^{1}CH_3^{III}$ are essentially unaffected in oxidation stage 3 but are considerably affected in oxidation stages 1 and 2, which indicates important changes in the oxidation fractions of heme III, *i.e.*, in its reduction potential. To exemplify this, the heme oxidation fractions obtained for all the hemes at pH 8.0 for PpcAF15L and PpcA are indicated in Table 5.1, showing that indeed those of heme III are the most affected.

Table 5.1 – Calculated oxidation fractions x_i for each heme group in each oxidation stage at pH 8.0 for PpcAF15L and wild-type cytochromes. The heme oxidation fractions x_i in each stage of oxidation were calculated according to Equation 3.1 (Chapter 3). Values indicated in parenthesis are those for the wild-type cytochrome.

Oxidation stage	x_i		
	Heme I	**Heme III**	**Heme IV**
0	0.00 (0.00)	0.00 (0.00)	0.00 (0.00)
1	0.35 (0.48)	0.40 (0.25)	0.23 (0.27)
2	0.81 (0.88)	0.58 (0.40)	0.60 (0.73)
3	1.00 (1.00)	1.00 (1.00)	1.00 (1.00)

As for the wild-type cytochrome, the thermodynamic model was used to fit the pH dependence of the observed chemical shifts of the heme methyls, together with data from UV-visible redox titrations obtained at pH 7.0 and 8.0. The thermodynamic parameters and the macroscopic pK_a values associated with the four stages of oxidation are indicated in Table 5.2 and Table 5.3, respectively.

Table 5.2 – Energy parameters (meV) of PpcAF15L and PpcA. Diagonal terms (in boldface type) represent the oxidation energies of the three hemes and the deprotonating energy of the redox-Bohr center (g_H) in the fully reduced and protonated proteins. Off-diagonal values are the redox (heme-heme) and redox-Bohr (heme-proton) interactions energies. The standard errors are given in parenthesis. Following the nomenclature for the pairwise interacting centers model, the pK_a of the reduced proteins is given by g_HF/[(ln10)RT] and the pK_a of the oxidized ones is given by ($g_H + \Sigma g_{iH}$)F/[ln(10)RT].

	Energy (meV)			
PpcA	**Heme I**	**Heme III**	**Heme IV**	**Redox-Bohr center**
Heme I	**-154 (5)**	27 (2)	16 (3)	-32 (4)
Heme III		**-138 (5)**	41 (3)	-31 (4)
Heme IV			**-125 (5)**	-58 (4)
Redox-Bohr center				**495 (8)**
PpcAF15L	**Heme I**	**Heme III**	**Heme IV**	**Redox-Bohr center**
Heme I	**-164 (4)**	24 (2)	14 (2)	-20 (4)
Heme III		**-168 (4)**	36 (2)	-17 (4)
Heme IV			**-136 (5)**	-49 (4)
Redox-Bohr center				**485 (8)**

Table 5.3 – Macroscopic pK_a values of the redox-Bohr center for PpcAF15L and wild-type cytochromes. The values were calculated from the parameters listed in Table 5.2.

Oxidation stage	pK_a	
	PpcAF15L	PpcA
0	8.5	8.6
1	8.0	8.0
2	7.5	7.2
3	7.0	6.5
ΔpK_a	1.5	2.1

The quality of the fittings obtained for the pH dependence of the paramagnetic chemical shifts and for the UV-visible redox titrations (Figure 5.7) clearly shows that the experimental data are well described by the model considering one protonatable center. The strongest redox interactions are observed between the closest pair of heme groups (I–III and III–IV). As expected, considering that the geometry of the heme core is conserved in the mutant, the pairwise heme redox interactions are maintained. However, important changes were observed in the reduction potentials and redox-Bohr interactions. All reduction potentials are more negative in the mutant and the redox-Bohr interactions are weaker (Table 5.2). These experimental observations, in the context of an undisturbed heme core as shown above, indicate that the hemes are slightly more solvent-exposed in the mutant. This effect is larger for heme III as can be seen from the more pronounced decrease in the reduction potential and redox-Bohr interaction, and most probably has its origin in the local rearrangements in the α-helix located between hemes I and III caused by the removal of the aromatic phenyl ring at position 15 (Figure 5.4). In PpcAF15L the strongest redox-Bohr effect remains associated with heme IV as observed in the native protein.

5.1.1.4 Role of Phe^{15} in the functional mechanism of PpcA

The replacement of Phe^{15} by a leucine residue had the effect of lowering the reduction potentials of the hemes and reducing the macroscopic redox-Bohr effect. However, such results *per se* do not give any insight into the mutation effect on the functional mechanism of the protein. Mechanistic information about the electron transfer pathways in multiheme proteins can only be obtained from a detailed thermodynamic characterization of the redox centers. Indeed, from the thermodynamic parameters listed in Table 5.2, it is possible to evaluate the contribution of each of the 16 microstates during the oxidation of PpcA or PpcAF15L at physiological pH. Such a study was previously done for the wild-type protein and a coherent electron transfer pathway coupled to proton transfer was established (Chapter 3). The relative variation of the microstates in PpcA is depicted in Figure 5.8 together with the relative variations obtained for PpcAF15L.

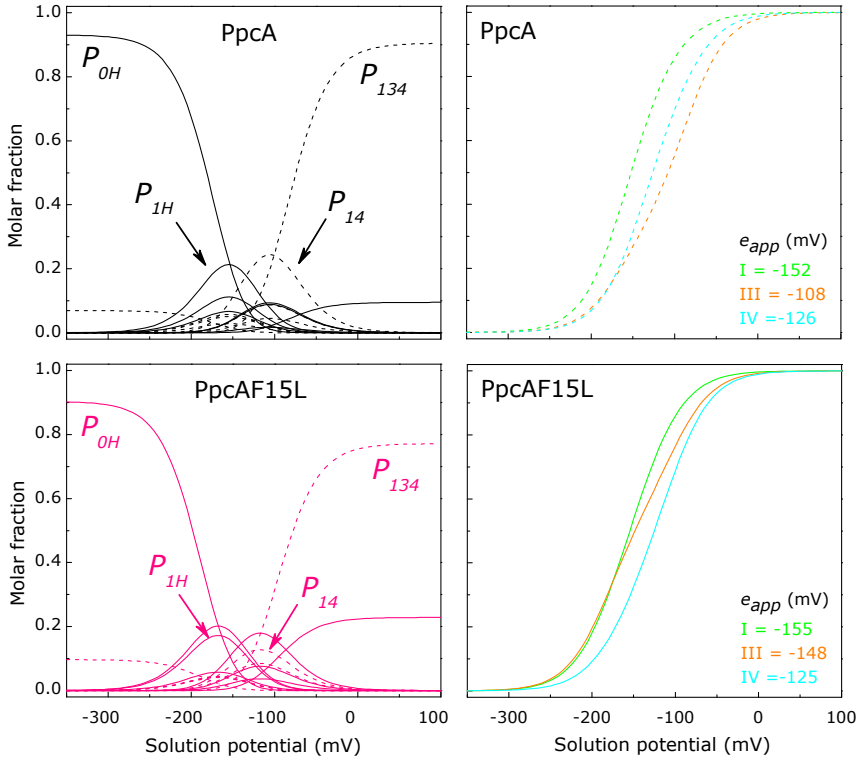

Figure 5.8 – Molar fractions of the 16 individual microstates (left panels) and oxidation fractions of individual hemes (right panels) in PpcAF15L and wild-type cytochromes. The curves were calculated at pH 7.5 as a function of the solution reduction potential using the parameters listed in Table 5.2. In the left panels, solid lines and dashed lines indicate the protonated and deprotonated microstates (described in Figure 2.5 – Chapter 2), respectively.

Whereas in the wild-type protein a concerted e^-/H^+ transfer occurs between oxidation stages 1 and 2, it is clear that the relative contributions of different microstates to the overall population in each stage are dramatically changed in the mutated protein. In fact, in the wild-type cytochrome oxidation stage 0 is dominated by the fully reduced and protonated form P_{0H} and stage 1 is dominated by the oxidation of heme I (P_{1H}) while keeping the acid–base center protonated. Oxidation stage 2 is dominated by the oxidation of hemes I and IV and deprotonation of the acid–base center (P_{14}), which remains deprotonated in stage 3 upon full oxidation of heme III (P_{134}). Therefore, a route is defined for electron transfer in PpcA: $P_{0H} \rightarrow P_{1H} \rightarrow P_{14} \rightarrow P_{134}$, which is disrupted in the mutant (Figure 5.8). The concerted e^-/H^+ transfer performed by PpcA derives from the higher reduction potential of heme III compared with the reduction potentials of hemes I and IV, ensuring that oxidation stages 1 and 2 are dominated essentially by particular microstates (P_{1H} and P_{14}). The F15L mutation brings closer the midpoint reduction potential values of all heme groups (right panels in Figure 5.8 for wild-type and mutant proteins) and concomitantly the intermediate oxidation stages are no longer dominated by single microstates. Consequently, no preferential pathway is established for electron transfer in the mutant protein. In addition, the coupled e^-/H^+ transfer observed between oxidation stages 1 and 2 in the native protein is also lost in the mutated cytochrome.

These observations suggest that Phe^{15} has an important structural role in preserving the required geometry of those axial ligands, and in fine-tuning the reduction potentials of the hemes.

5.1.1.5 Comparison with tetraheme cytochromes c_3

The conserved structural motif formed by Phe^{15} and hemes I and III is also present in tetraheme cytochromes c_3, in which Phe^{20} occupies an equivalent position. In the particular cases of *Desulfovibrio vulgaris* tetraheme cytochrome c_3 isolated from the strains Hildenborough ($DvHc_3$) and Miyazaki ($DvMc_3$), biochemical studies using Phe^{20} mutants have been performed [8-10]. However, the redox characterization of these mutants was limited to a quantitative macroscopic redox study for $DvHc_3$ and a partial microscopic characterization of the redox centers for $DvMc_3$, which restricted the determination of the heme reduction potentials in the first and last oxidation steps [10]. Consequently, in the absence of a detailed thermodynamic characterization of the Phe^{20} mutants of cytochromes c_3, a comparison of the role of Phe^{15} in the cytochrome c_7 family and that of Phe^{20} in the tetraheme c_3 family cannot be made. Nevertheless, a qualitative analysis of the individual heme oxidation patterns of an equivalent mutant (F20I) in the tetraheme cytochrome c_3 from $DvHc_3$ [9] showed that the order of the heme oxidation is unaltered, suggesting a specific role of the conserved residue within each family of cytochromes.

5.1.2 Met^{58} protects heme III from solvent exposure

The residue Met^{58} is located in the end of the α-helix near heme III, and protects this heme from solvent exposure (Figure 5.9).

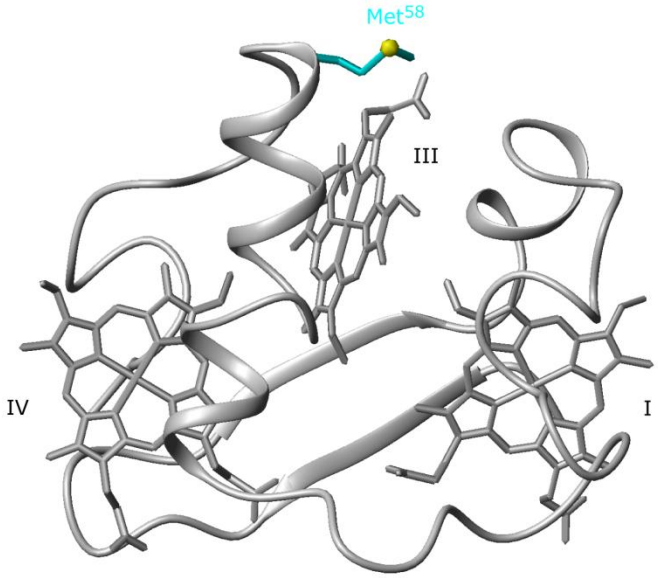

Figure 5.9 – Spatial localization of residue Met^{58} in PpcA solution structure. The sulphur atom of the methionine side chain is represented in yellow.

In the mutant proteins, Met^{58} was replaced by a serine (PpcAM58S), an asparagine (PpcAM58N), an aspartate (PpcAM58D) and a lysine (PpcAM58K). Thus, the effect of replacing a non-polar residue by a polar residue (Ser and Asn), a negatively charged residue (Asp) or a positively charged one (Lys) was evaluated.

5.1.2.1 Heme core architecture in the reduced form

The heme core architecture of the PpcAM58 mutant proteins was probed by 2D NMR as for the wild-type (Chapter 3). The heme proton resonances were assigned (Table A.4 – Appendix) and their chemical shifts were compared to those of wild-type PpcA (Figure 5.10).

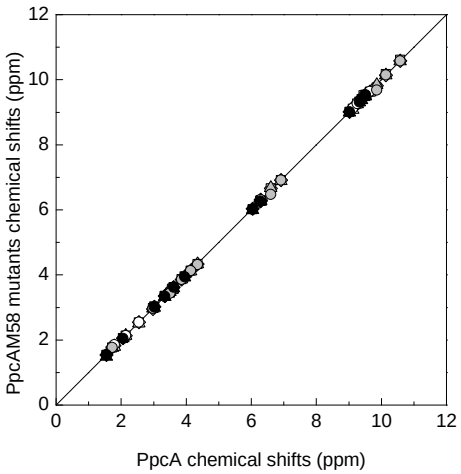

Figure 5.10 – Comparison of the observed heme proton chemical shifts of reduced PpcAM58 mutants and those of PpcA at pH 8 and 15 °C. The symbols correspond to the mutants PpcAM58D (△), PpcAM58K (○), PpcAM58N (□) and PpcAM58S (◇), and white, gray, and black symbols correspond to hemes I, III, and IV, respectively. The rmsd between the chemical shifts measured for PpcAM58 mutants and those of PpcA are (0.02; 0.03; 0.03 ppm) for PpcAM58D, (0.02; 0.07; 0.01 ppm) for PpcAM58K, (0.01; 0.05; 0.01 ppm) for PpcAM58N and (0.02; 0.03; 0.01 ppm) for PpcAM58S, (heme I; heme III; heme IV) respectively. The solid line has a unit slope.

From this comparison, a very good correlation was obtained. The rmsd value between the chemical shifts for the wild-type and mutant cytochromes is quite low, but slightly higher for heme III resonances as expected given the close location of residue Met^{58} to this heme. The NOE connectivities between the heme groups were also analyzed, and it was verified that the same set of connectivities were observed for PpcA and the mutant proteins. Overall, the results obtained show that the heme core arrangement is similar for all the proteins.

5.1.2.2 Preliminary screening of the heme oxidation profiles

As described for PpcAF15L, the heme oxidation profiles of PpcAM58 mutated proteins were first studied by 2D-EXSY NMR at pH 6 and 8 (Figure 5.11).

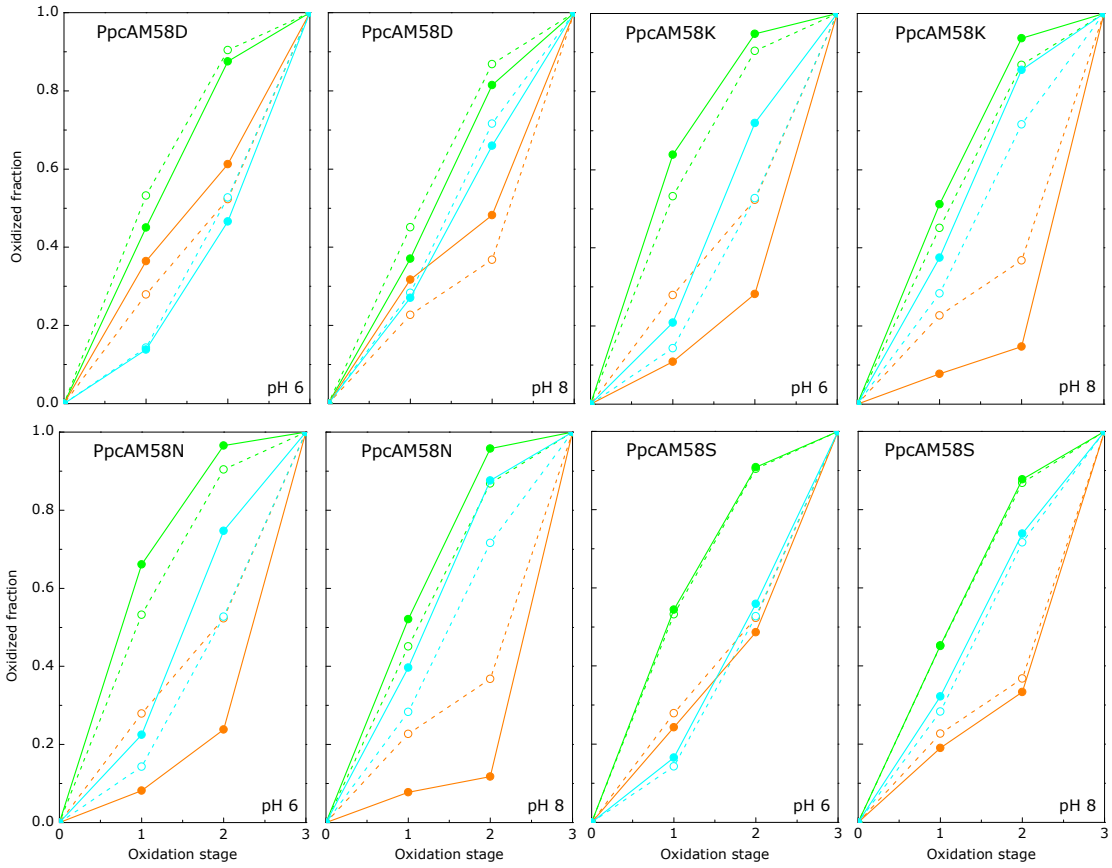

Figure 5.11 – Oxidation fraction of PpcAM58 mutants (solid symbols and lines) and PpcA (open symbols and dashed lines) at pH 6 and pH 8. Heme I, III and IV data are colored in green, orange and blue, respectively. The heme oxidation fractions were calculated according to Equation 3.1 (Chapter 3).

In all mutants, with exception of PpcAM58S, the replacement altered significantly the heme oxidation profiles at both pH values. The comparison between the mutants' and the wild-type heme oxidation fractions show significant changes in heme III, which correlates with the spatial localization of Met^{58}. However, the effect on heme III oxidation fractions is not identical in the four proteins.

The heme III oxidation fractions are clearly higher in PpcAM58D than those observed for the wild-type protein (Figure 5.11). The opposite effect is observed in mutant PpcAM58K (Figure 5.11). In these two mutants, the changes observed in the oxidized fractions of heme III can be explained by simple electrostatic considerations. Indeed, the introduction of a negative charge is expected to stabilize the oxidized form of the heme group and, thus, facilitates the removal of the electron (higher oxidized fractions). The reverse effect is expected for the introduction of a positive charge (PpcAM58K) in the vicinity of heme III.

The effect on heme oxidation profiles by the replacement of Met^{58} by the polar residues asparagine and serine yielded different results (Figure 5.11), which could not be predicted,

since polarity around heme groups can have antagonic effects [4]. In the case of PpcAM58N, an oxidation profile similar to the one displayed by PpcAM58K was obtained, whereas for PpcAM58S no significant effects were observed in comparison with the wild-type protein.

Since PpcAM58 mutants introduced significant changes in the heme oxidation profiles at pH 6 and 8, these proteins were characterized in detail. In this study, the characterization of PpcAM58S was also included, in order to confirm if when the same heme oxidation profiles are observed at pH 6 and pH 8 the final thermodynamic parameters are identical.

5.1.2.3 Thermodynamic characterization of PpcAM58 mutants

The full thermodynamic characterization of PpcAM58 mutants was carried out as described for the wild-type protein. The chemical shifts obtained for the same set of heme methyls at the different oxidation stages for the mutated proteins are plotted in Figure 5.12.

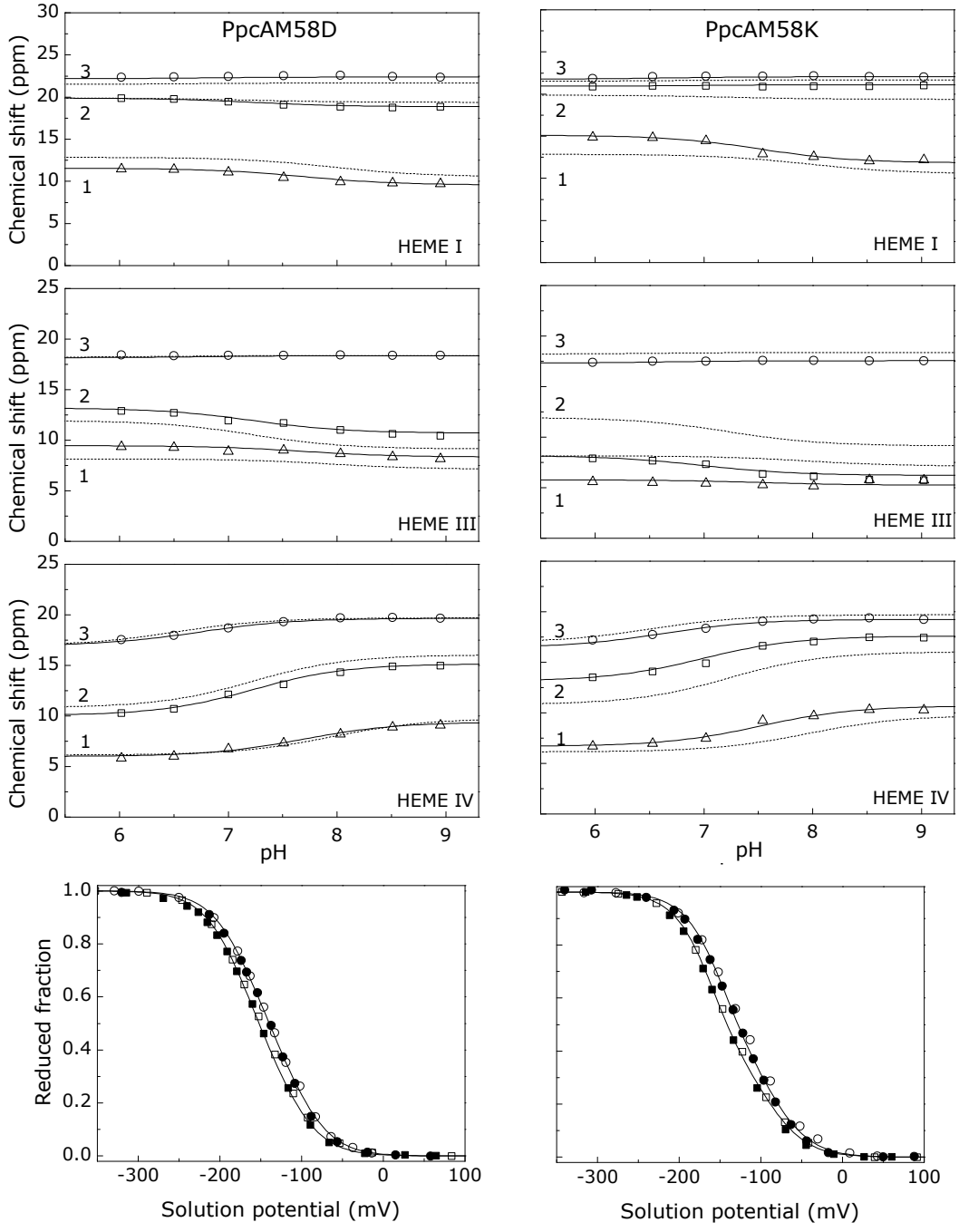

Figure 5.12 – Fitting of the thermodynamic model to the experimental data for PpcAM58 mutants. The solid lines are the result of the simultaneous fitting of the NMR and UV-visible data. The three upper panels show the pH dependence of heme methyl chemical shifts at oxidation stages 1 (△), 2 (□), and 3 (○).The dashed lines in each panel represent the best fit for the wild-type protein. The lower panel corresponds to the reduced fractions determined by UV-visible spectroscopy at pH 7.0 (○) and pH 8.0 (□). The open symbols and the filled symbols represent the data points in the reductive and oxidative titrations, respectively.

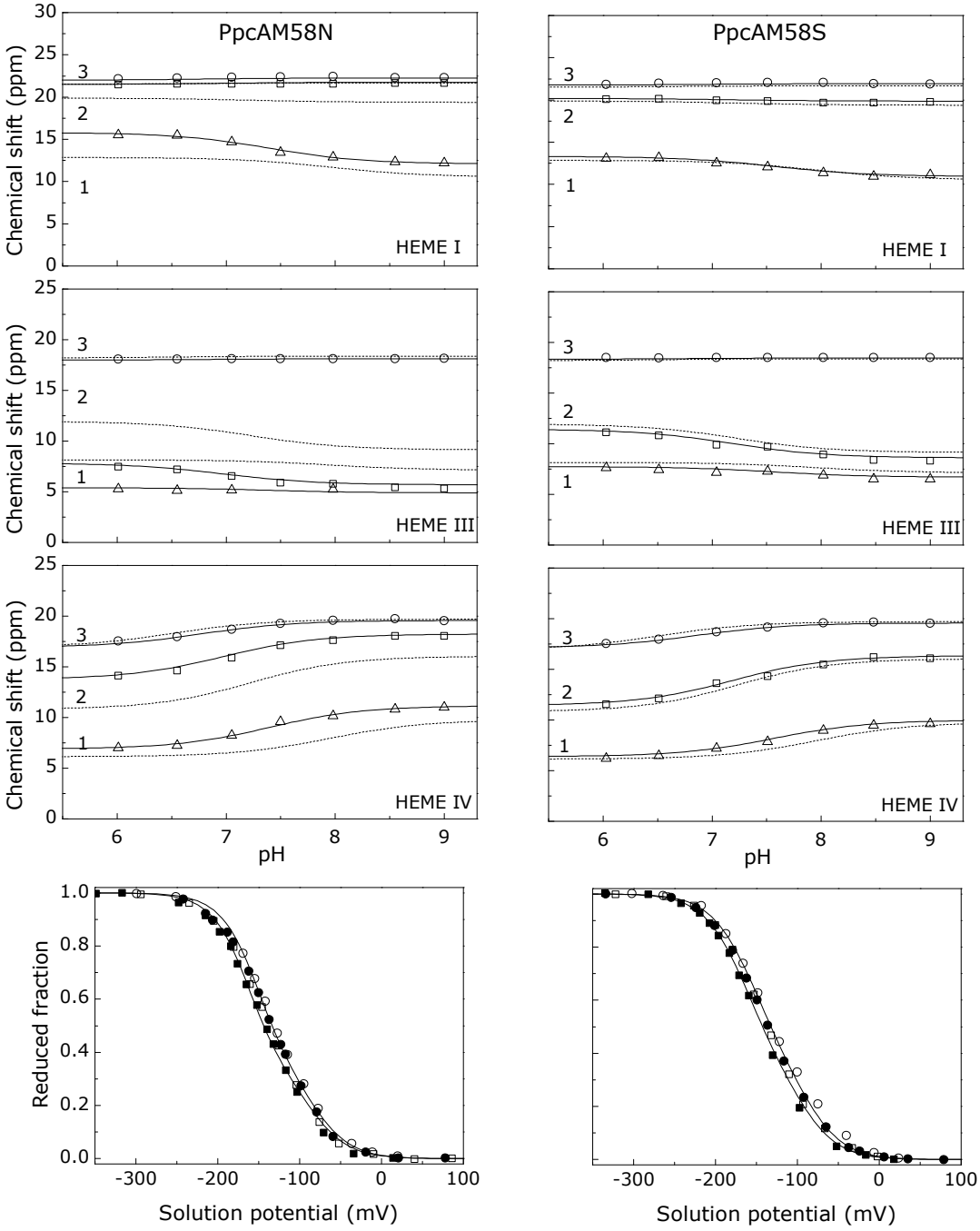

Figure 5.12 (cont.) – Fitting of the thermodynamic model to the experimental data for PpcAM58 mutants.

In contrast with PpcAF15L, the chemical shifts of all the heme groups in the fully oxidized state of PpcAM58 mutants are similar to the ones observed for the wild-type, which indicates that the heme core structure, including the geometry of the heme axial ligands [11], is maintained.

As for the wild-type protein, the thermodynamic model (Chapter 2) was used to fit the pH dependence of the observed chemical shifts of the heme methyls, together with data from UV-visible redox titrations obtained at pH 7 and 8 (Figure 5.12). The thermodynamic parameters obtained from the fitting for the four PpcAM58 mutants are shown in Table 5.4.

Table 5.4 – Energy parameters (meV) for PpcAM58 mutants. Diagonal terms (in boldface type) represent the oxidation energies of the three hemes and the deprotonating energy of the redox-Bohr center (g_H) in the fully reduced and protonated proteins. Off-diagonal values are the redox (heme-heme) and redox-Bohr (heme-proton) interactions energies. The standard errors are given in parenthesis.

	Energy (meV)			
PpcAM58D	**Heme I**	**Heme III**	**Heme IV**	**Redox-Bohr center**
Heme I	**-161 (4)**	18 (2)	6 (2)	-18 (3)
Heme III		**-156 (4)**	29 (2)	-18 (3)
Heme IV			**-134 (4)**	-44 (3)
Redox-Bohr center				**465 (7)**
PpcAM58K	**Heme I**	**Heme III**	**Heme IV**	**Redox-Bohr center**
Heme I	**-150 (4)**	8 (3)	-2 (3)	-18 (4)
Heme III		**-109 (4)**	26 (3)	-16 (4)
Heme IV			**-123 (4)**	-43 (4)
Redox-Bohr center				**457 (7)**
PpcAM58N	**Heme I**	**Heme III**	**Heme IV**	**Redox-Bohr center**
Heme I	**-153 (3)**	-4 (3)	-9 (3)	-11 (3)
Heme III		**-103 (3)**	25 (3)	-7 (3)
Heme IV			**-126 (3)**	-38 (3)
Redox-Bohr center				**444 (5)**
PpcAM58S	**Heme I**	**Heme III**	**Heme IV**	**Redox-Bohr center**
Heme I	**-159 (4)**	17 (2)	6 (2)	-13 (4)
Heme III		**-139 (3)**	30 (2)	-10 (4)
Heme IV			**-131 (2)**	-37 (4)
Redox-Bohr center				**453 (8)**

With the exception of PpcAM58S, the comparison of the thermodynamic parameters of the mutants with those obtained for the wild-type protein showed the largest differences on heme III reduction potentials. In all PpcAM58 mutants, the redox and redox-Bohr interactions are smaller than the ones of PpcA. However, as observed for PpcA, the weaker redox interaction is between the heme groups that are structurally further apart (I-IV), and the strongest redox-Bohr interaction observed is with heme IV. The lower values of the interactions, in the context of an undisturbed heme core, might have their origin on structural rearrangements of charged groups that cause variations in local dielectric constants [12].

On a pure electrostatic basis, the heme-heme interactions are expected to be positive due to the repulsion between the electrons negative charge. On the other hand, the interaction energies between the heme groups and the redox-Bohr center are expected to be negative, as deprotonation of the latter will destabilize the heme electrons. Thus, the negative interaction energies between pairs of heme groups cannot be explained by electrostatics and suggests the existence of conformational changes. Similar results were observed for tetraheme cytochromes c_3 [13-15], that were explained when their structures were solved in both redox states and compared [16-18]. The negative interactions were attributed to redox-linked conformational changes in the heme propionates and localized structural rearrangements in the side chains near the heme groups [19].

5.1.2.4 Role of Met^{58} in the functional mechanism of PpcA

In order to evaluate the effect of the mutation on the functional mechanism of PpcA, the relative populations of each microstate at physiological pH were determined as function of the solution potential (Figure 5.13).

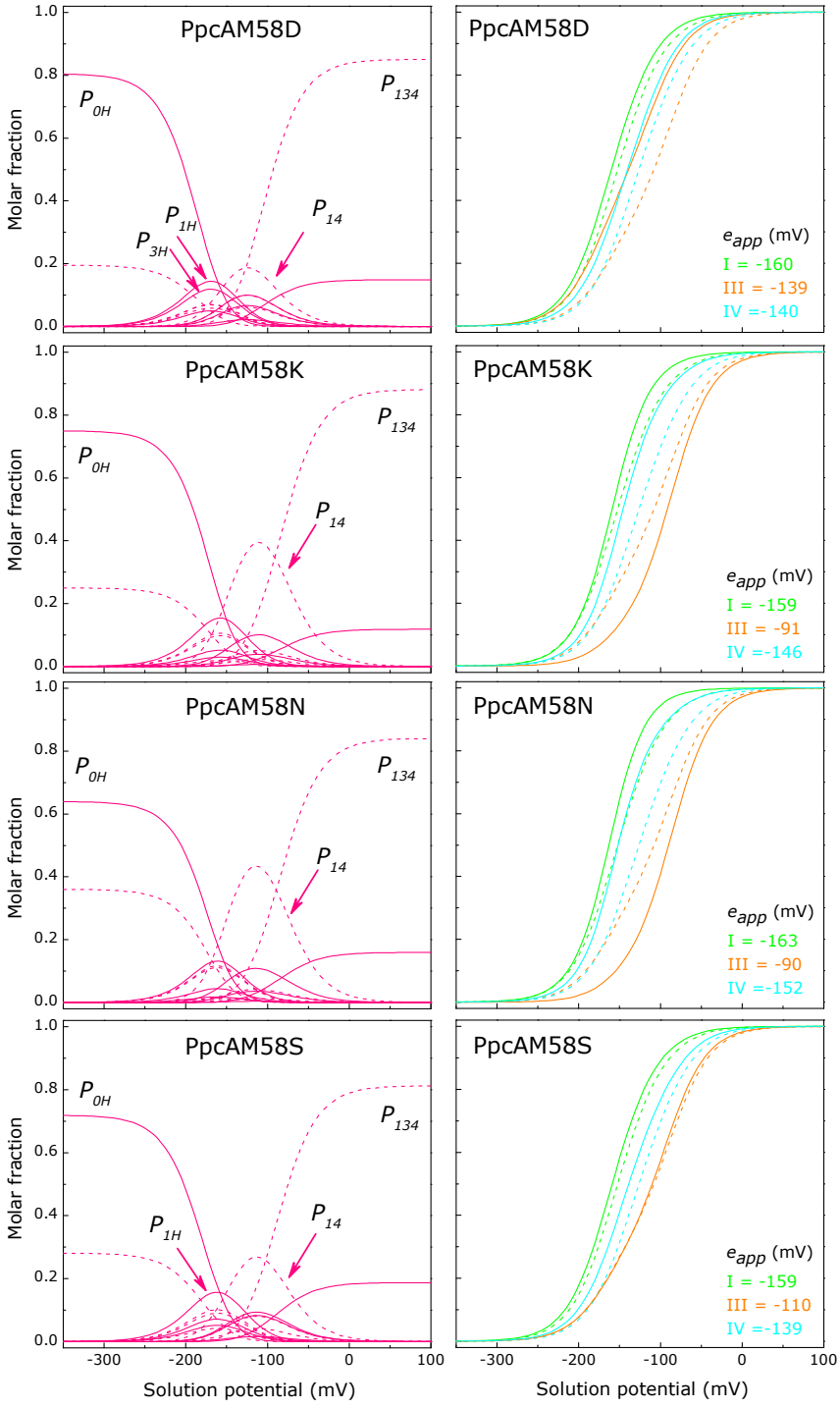

Figure 5.13 – Molar fractions of the 16 individual microstates (left panels) and oxidation fractions of individual hemes (right panels) in PpcAM58 mutants and wild-type cytochromes. The curves were calculated at pH 7.5 as a function of the solution reduction potential using the parameters listed in Table 5.4. In the left panels, solid lines and dashed lines indicate the protonated and deprotonated microstates, respectively. In the right panels, solid and dashed lines represent data for the mutant and wild-type proteins, respectively.

The analysis of the heme oxidation profiles for PpcAM58D shows that the introduction of a negative charge in the vicinity of heme III stabilizes the oxidized form of the protein, by lowering the apparent midpoint reduction potential (e_{app}) of the heme groups. As expected, heme III midpoint reduction potential is the most affected at physiological pH and the order of heme oxidation is I-(III,IV). At this pH, two microstates are now dominating the first oxidation stage (P_{1H} and P_{3H}) and no preferential pathway for electron transfer is observed.

When residue Met^{58} is replaced by the positively charged lysine, a significant alteration on heme III reduction potential is observed, but in a opposite direction to that observed in PpcAM58D. In the mutant PpcAM58K, the e_{app} value of heme III becomes more positive so that it becomes the last one to oxidize (Figure 5.13). In comparison with the wild-type protein, the order of oxidation of the heme groups is maintained, but now a different functional mechanism emerges, in which a $2e^-$ step coupled with proton transfer is well established.

Concerning to PpcAM58N and PpcAM58S mutants, the first one behaves as PpcAM58K, whereas the latter has a similar behavior to that observed for the wild-type protein (Table 5.4 and Figure 5.13). As mentioned above, an interpretation is not straightforward as small differences on polarity around heme groups are difficult to predict [4]. However, given the relatively high solvent exposure of heme III (215.8 $Å^2$) it is tempting to speculate that the small size of the serine side chain essentially does not affect the overall polarity around heme. On the contrary, the large volume of the asparagine side chain, in comparison with that of serine, can establish extra hydrogen bonds around heme III, that might lead to the stabilization of its reduced form.

In summary, the data obtained for the PpcAM58 mutants suggests that the preferred e^-/H^+ transfer pathway observed for PpcA is strongly dependent on the relative value of heme III reduction potential. Indeed, when the reduction potential of heme III reduction potential gets closer to the reduction potentials of the other two heme groups (PpcAM58D), the preferential pathway for electron transfer is disrupted. In contrast, the data obtained showed that, when heme III is clearly the last to oxidize (less negative potential), there is a well established e^-/H^+ transfer pathway, which involves a single or a two electron transfer coupled to proton transfer. The latter is favored by a larger difference between heme III reduction potential and the reduction potential of the previous heme to oxidize.

5.1.3 Lysine residues near the heme groups

The triheme cytochrome PpcA has an unusually high content of lysines, 17 out of 71 residues, which makes the surface of the protein greatly positive. To evaluate the influence of lysine residues in the vicinity of the different heme groups, lysine residues were selected for mutagenesis studies: conserved Lys^{18} between hemes I and III, Lys^{22} also between hemes I and III, Lys^{60} near heme III, and Lys^{9} and Lys^{52} near heme IV (Figure 5.14). Each lysine was replaced by an uncharged residue (glutamine) and a negatively charged one (glutamate).

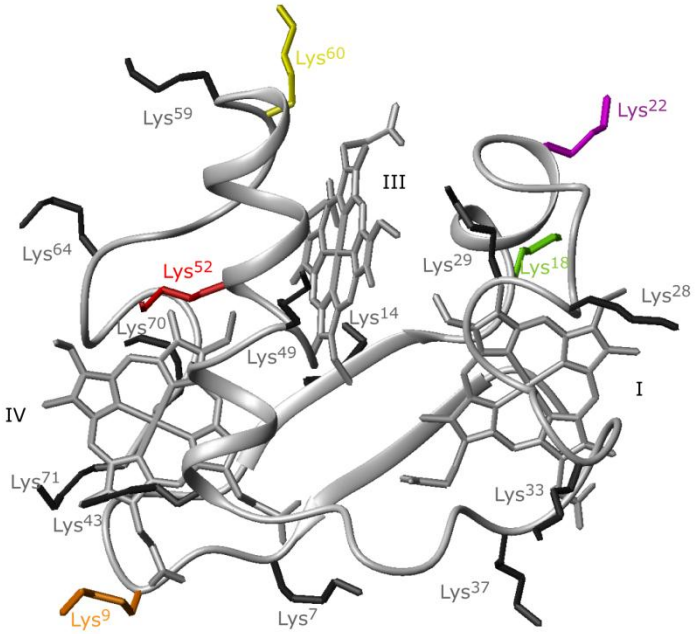

Figure 5.14 – Spatial localization of lysine residues in PpcA solution structure. Mutated lysines are highlighted in color.

5.1.3.1 Heme core architecture in the reduced form

As for the other mutated proteins, the heme proton resonances were assigned for PpcAK9Q and PpcAK9E (Table A.5 – Appendix), PpcAK18Q and PpcAK18E (Table A.6 – Appendix), PpcAK22Q and PpcAK22E (Table A.7 – Appendix), PpcAK52Q and PpcAK52E (Table A.8 – Appendix) and PpcAK60Q and PpcAK60E (Table A.9 – Appendix), following the same strategy as for the wild-type protein (Chapter 3). When the chemical shifts are compared with those obtained for the wild-type protein a good correlation is observed (Figure 5.15). Additionally, the interheme connectivities observed were the same for all the proteins, which indicates that the heme core structure is maintained.

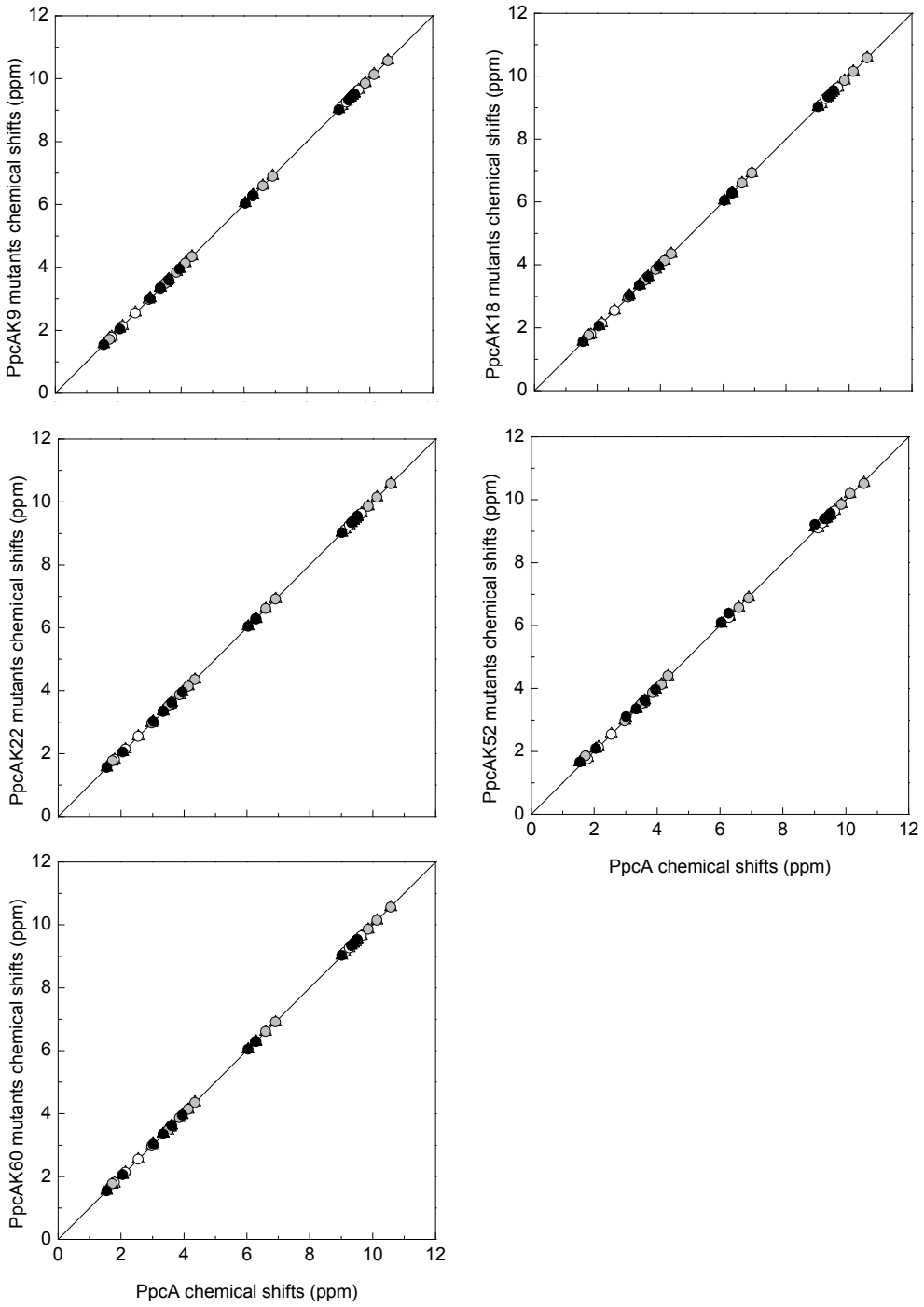

Figure 5.15 – Comparison of the observed heme proton chemical shifts of reduced PpcA lysine mutants and those of PpcA at pH 8 and 15 °C. The symbols correspond to the glutamine (△) and the glutamic acid mutants (○), and white, gray, and black symbols correspond to hemes I, III, and IV, respectively. The rmsd between the chemical shifts measured between the wild-type and PpcAK9, PpcAK18 and PpcAK22 mutants is 0.01 ppm for all the heme groups, while for PpcAK52Q is (0.01; 0.03; 0.05 ppm), for PpcAK52E (0.02; 0.05; 0.08 ppm), and for PpcAK60 mutants is (0.01; 0.02; 0.01 ppm); (heme I; heme III; heme IV) respectively. The solid line has a unit slope.

5.1.3.2 Preliminary screening of the heme oxidation profiles

2D-EXSY NMR spectra were obtained at pH 6 and pH 8 for all lysine mutants, and the chemical shifts for the same set of methyls as for the wild-type was used to monitor the stepwise oxidation of each heme.

In the case of Lys^{9} (PpcAK9Q and PpcAK9E), Lys^{18} (PpcAK18Q and PpcAK18E) and Lys^{22} (PpcAK22Q and PpcAK22E) the replacement did not affect significantly the oxidation profile of the heme groups (Figure 5.16).

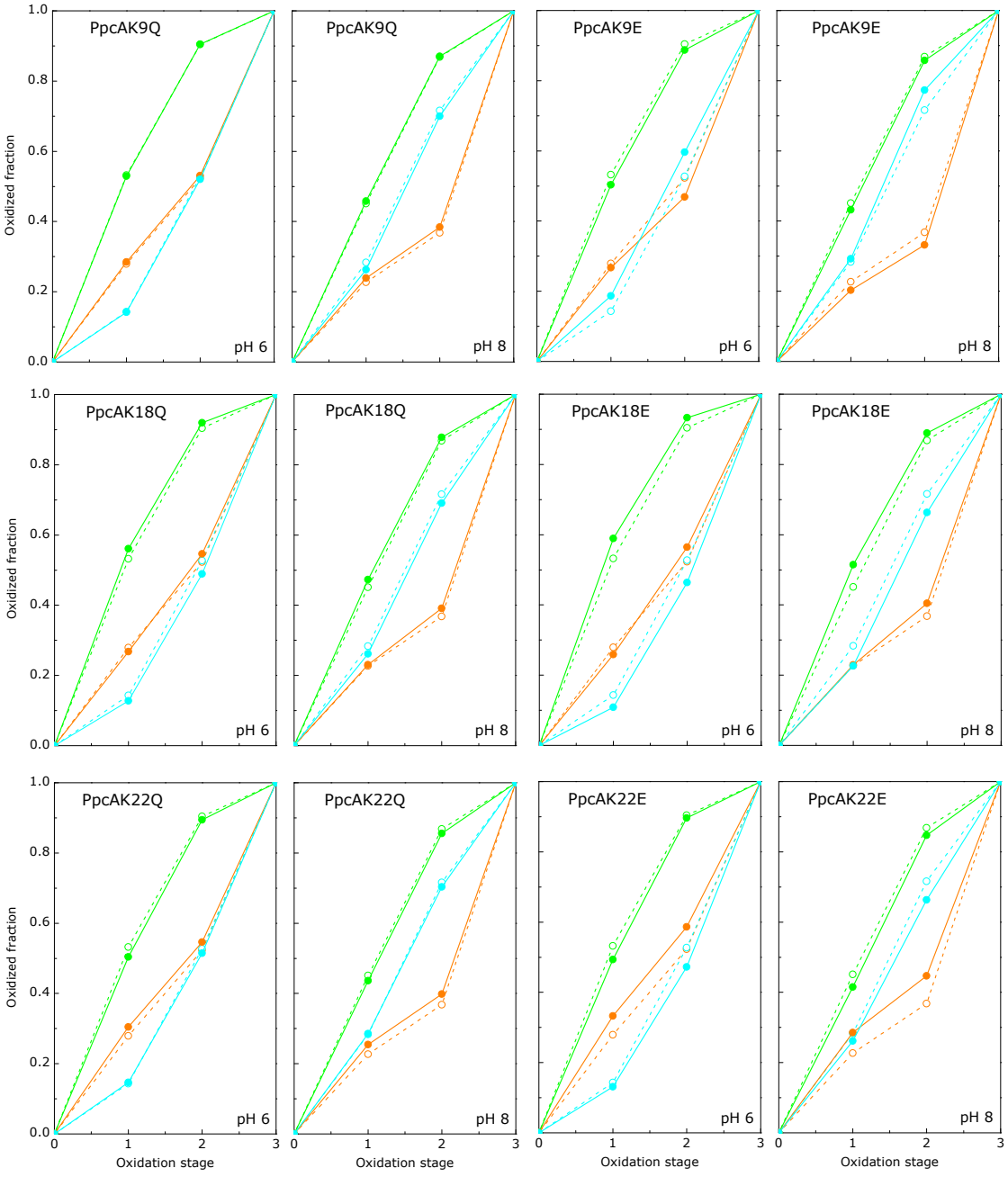

Figure 5.16 – Oxidation fraction of PpcAK9, PpcAK18 and PpcAK22 mutants (solid symbols and lines) and PpcA (open symbols and dashed lines) at pH 6 and pH 8. Heme I, III and IV data are colored in green, orange and blue, respectively. The heme oxidation fractions were calculated according to Equation 3.1 (Chapter 3).

Lys^{9} is located in the turn segment near heme IV that connects the two-strand β-sheet at the N-terminus of the polypeptide chain (Figure 5.14). From the PpcA solution structure (Chapter 4) it was observed that Lys^{9} backbone NH forms a hydrogen bond with the oxygen atom O2 of heme IV propionate 17 (P_{17}^{IV}). A double mutant in this position (K9-10A) has been studied for *Dac*$_7$ [20]. In this case, a similar result was obtained, with the replacement of the two lysines not affecting the reduction potentials of the heme groups. Thus, Lys^{9} seems to have an important role in stabilizing heme IV propionate P_{17}^{IV} (Chapter 4).

Lys^{18} is a conserved residue in most of the *c*$_7$ cytochromes from *Geobacteraceae* bacteria (Figure 1.2 – Chapter 1). This residue is located in the α-helix between hemes I and III (Figure 5.14). No significant changes were observed in the oxidized fractions of PpcAK18 mutants when compared to the wild-type. This is probably related to the fact that this residue is located on the outer surface of the α-helix, with its side chain pointing towards the protein exterior.

Lys^{22} is located one turn after Lys^{18} in the same α-helix (Figure 5.14). Thus, it is expected that its side chain is also pointing outside the protein. Consequently, the redox properties of the heme groups shouldn't be significantly affected by the mutations in Lys^{22} residue.

On the other hand, for Lys^{52} and Lys^{60} families, the removal of the positive charge changed the heme oxidation profiles significantly (Figure 5.17).

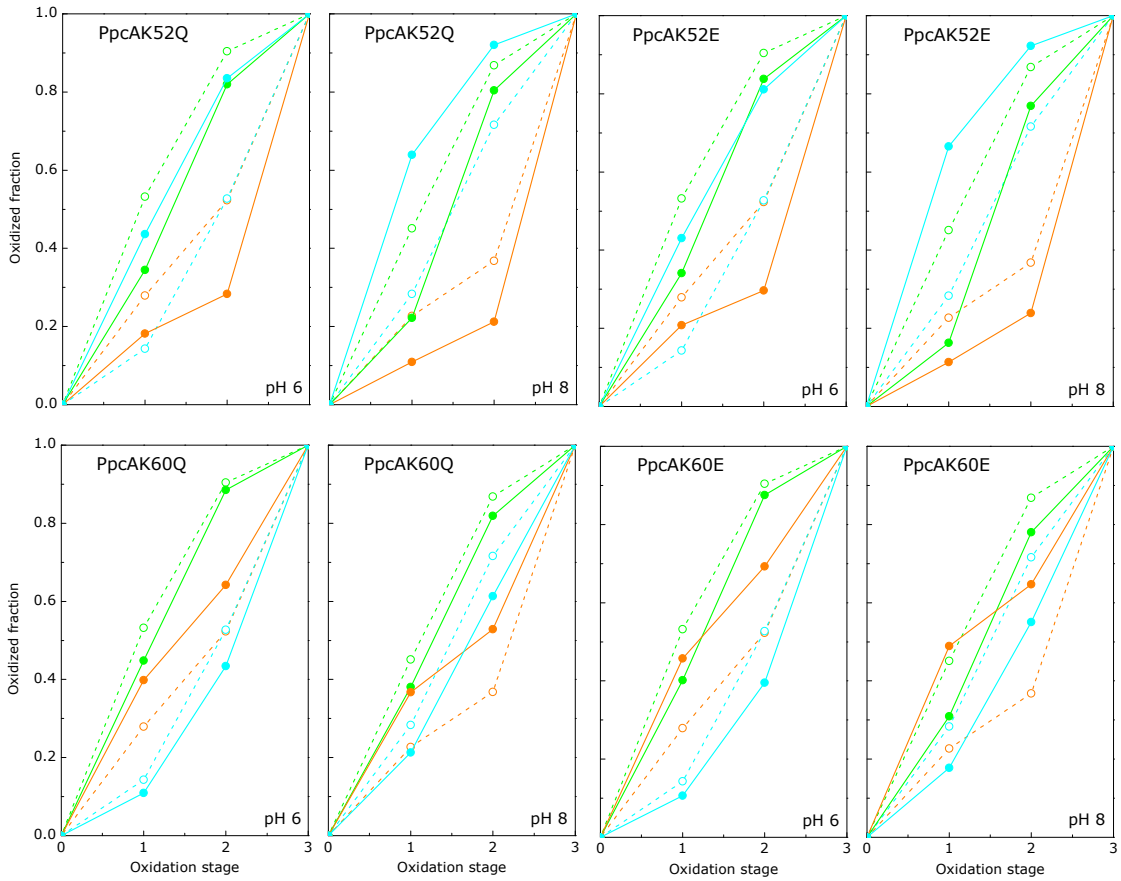

Figure 5.17 – Oxidation fraction of PpcAK52 and PpcAK60 mutants (solid symbols and lines) and PpcA (open symbols and dashed lines) at pH 6 and pH 8. Heme I, III and IV data are colored in green, orange and blue, respectively. The heme oxidation fractions were calculated according to Equation 3.1 (Chapter 3).

Residue Lys^{52} is positioned on top of heme IV in the beginning of the α-helix between hemes III and IV, with its side chain almost parallel to heme IV plane (Figure 5.14). The removal of a positive charge near heme IV is reflected in the oxidized fractions of the heme groups at both pH values. The most affected is heme IV, which becomes the first heme to oxidize. At these two pH values, the effect seems to be similar when a neutral or a negatively charged residue is introduced at position 52. This indicates that, in the environment of Lys^{52}, the glutamate residue might be protonated or hydrogen bonded to a neighboring residue.

On the contrary, the replacement of Lys^{60} positive charge by a negative or neutral one has a distinct effect on the heme III oxidation fractions at intermediate stages of oxidation. In both cases, heme III displays higher oxidation fractions as its reduced form is less stabilized. This effect is more notorious on PpcAK60E mutant and the order of oxidation of the heme groups is different when compared to PpcA (III-I-IV *vs.* I-IV-III).

Since major changes were observed in Lys^{52} and Lys^{60} mutant families, the thermodynamic properties of their heme groups were further characterized in detail.

5.1.3.3 Thermodynamic characterization of PpcAK52 and PpcAK60 mutants

In order to fully characterize the thermodynamic properties of the PpcAK52 and PpcAK60 mutants, the stepwise oxidation of the heme groups was monitored by 2D-EXSY NMR spectra at different pH values. Together with the results from redox titrations followed by UV-visible spectroscopy at pH 7 and 8, the thermodynamic parameters were calculated as described for the wild-type protein (Figure 5.18 and Figure 5.19).

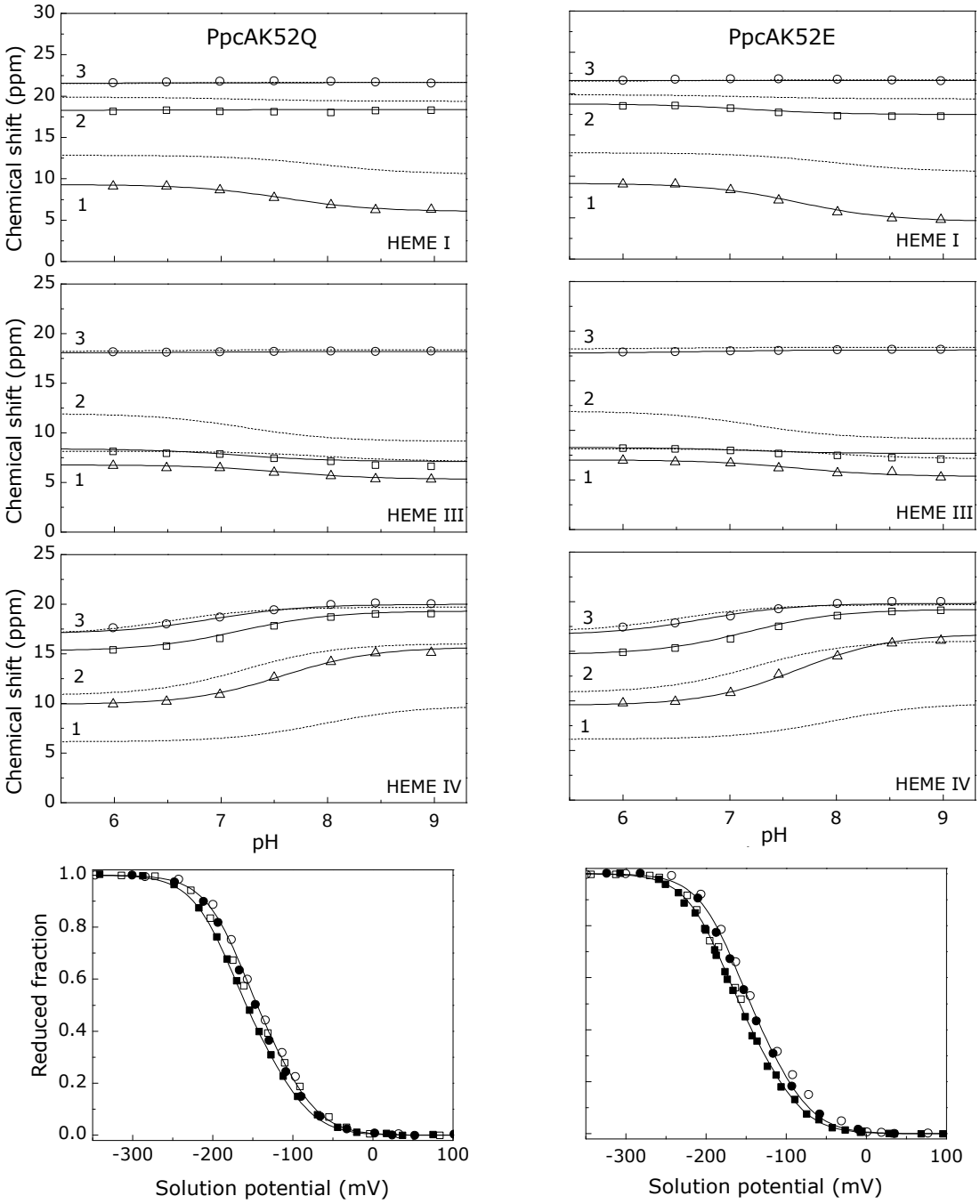

Figure 5.18 – Fitting of the thermodynamic model to the experimental data for PpcAK52 mutants. The solid lines are the result of the simultaneous fitting of the NMR and UV-visible data. The three upper panels show the pH dependence of heme methyl chemical shifts at oxidation stages 1 (△), 2 (□), and 3 (○).The dashed lines in each panel represent the best fit for the wild-type protein. The lower panel corresponds to the reduced fractions determined by UV-visible spectroscopy at pH 7.0 (○) and pH 8.0 (□). The open symbols and the filled symbols represent the data points in the reductive and oxidative titrations, respectively.

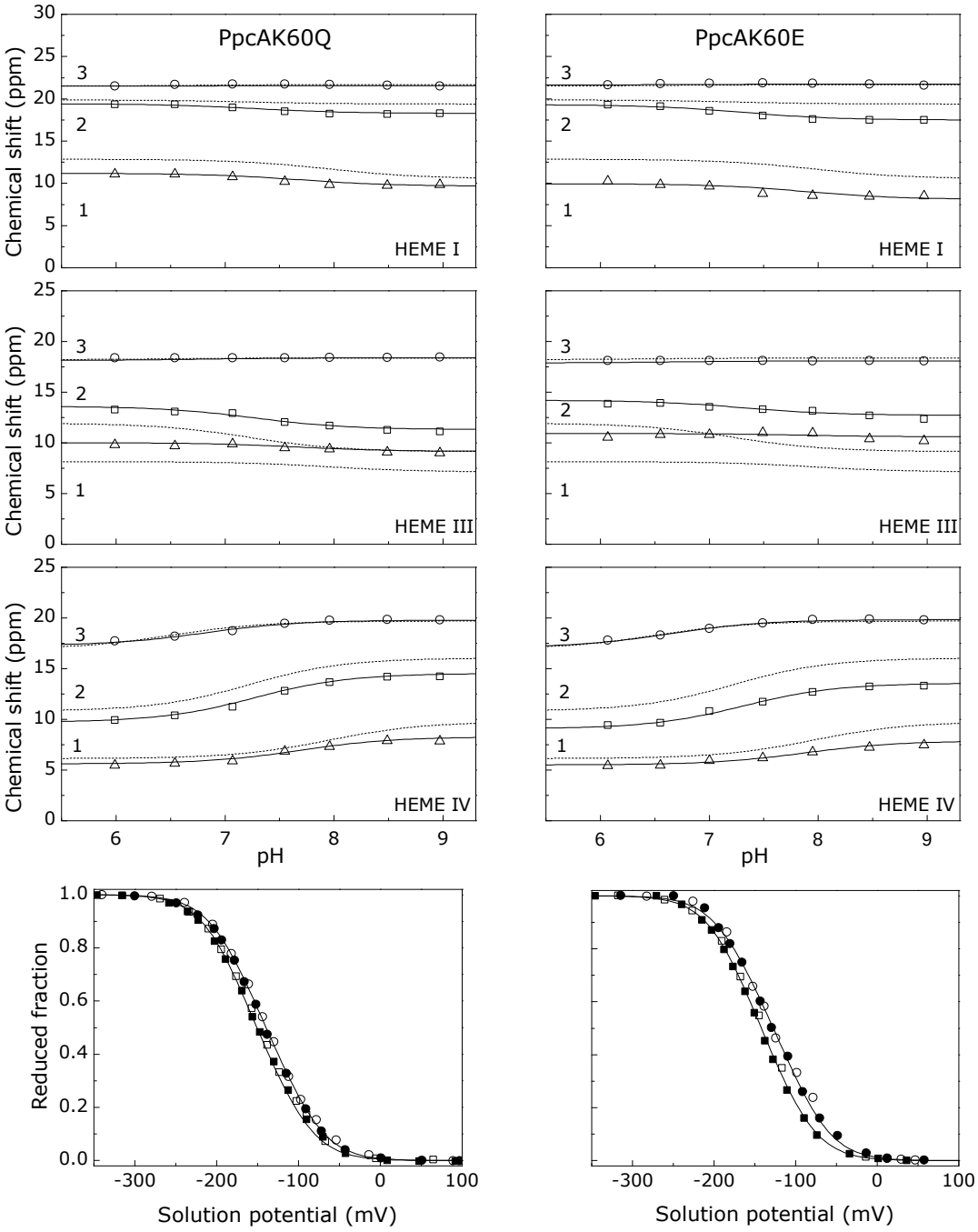

Figure 5.19 – Fitting of the thermodynamic model to the experimental data for PpcAK60 mutants. The solid lines are the result of the simultaneous fitting of the NMR and UV-visible data. The three upper panels show the pH dependence of heme methyl chemical shifts at oxidation stages 1 (△), 2 (□), and 3 (○).The dashed lines in each panel represent the best fit for the wild-type protein. The lower panel corresponds to the reduced fractions determined by UV-visible spectroscopy at pH 7.0 (○) and pH 8.0 (□). The open symbols and the filled symbols represent the data points in the reductive and oxidative titrations, respectively.

The analysis of the NMR data showed that the chemical shifts of the heme methyls in the fully oxidized state is similar to the wild-type protein. This allows a straightforward comparison between the chemical shifts at each intermediate stage and the correspondent

heme oxidation fractions. However the oxidized fractions in the intermediate stages are different for all hemes.

For PpcAK52 mutants it is clear that heme oxidation fractions of heme IV are significantly higher at both intermediate oxidation stages (stages 1 and 2). As described by Equation 2.4 (Chapter 2), the increase of the heme IV oxidation fractions are compensated by decreasing the oxidation fractions of hemes I and III at each correspondent oxidation stage.

The thermodynamic parameters obtained from the fitting of the thermodynamic model for the fully reduced and protonated proteins are presented in Table 5.5 and Table 5.6.

Table 5.5 – Energy parameters (meV) for PpcAK52 mutants. Diagonal terms (in boldface type) represent the oxidation energies of the three hemes and the deprotonating energy of the redox-Bohr center (g_H) in the fully reduced and protonated proteins. Off-diagonal values are the redox (heme-heme) and redox-Bohr (heme-proton) interactions energies. The standard errors are given in parenthesis.

	Energy (meV)			
PpcAK52Q	**Heme I**	**Heme III**	**Heme IV**	**Redox-Bohr center**
Heme I	**-154 (3)**	20 (2)	0 (2)	-15 (3)
Heme III		**-138 (3)**	20 (2)	-11 (3)
Heme IV			**-160 (4)**	-43 (3)
Redox-Bohr center				**466 (6)**
PpcAK52E	**Heme I**	**Heme III**	**Heme IV**	**Redox-Bohr center**
Heme I	**-154 (3)**	20 (2)	1 (2)	-14 (3)
Heme III		**-142 (3)**	27 (2)	-22 (3)
Heme IV			**-160 (4)**	-59 (3)
Redox-Bohr center				**482 (6)**

Table 5.6 – Energy parameters (meV) for PpcAK60 mutants. Diagonal terms (in boldface type) represent the oxidation energies of the three hemes and the deprotonating energy of the redox-Bohr center (g_H) in the fully reduced and protonated proteins. Off-diagonal values are the redox (heme-heme) and redox-Bohr (heme-proton) interactions energies. The standard errors are given in parenthesis.

	Energy (meV)			
PpcAK60Q	**Heme I**	**Heme III**	**Heme IV**	**Redox-Bohr center**
Heme I	**-164 (3)**	22 (2)	6 (2)	-15 (3)
Heme III		**-162 (3)**	30 (2)	-16 (3)
Heme IV			**-132 (3)**	-40 (3)
Redox-Bohr center				**461 (6)**
PpcAK60E	**Heme I**	**Heme III**	**Heme IV**	**Redox-Bohr center**
Heme I	**-151 (5)**	24 (3)	9 (3)	-23 (5)
Heme III		**-157 (6)**	35 (3)	-29 (5)
Heme IV			**-121 (6)**	-49 (5)
Redox-Bohr center				**482 (11)**

The thermodynamic parameters determined for PpcAK52 mutants show that the reduction potential of heme IV is lowered by 35 mV, while the redox potentials of the other heme groups are very similar to the wild-type (Table 5.5). The interactions between the heme groups are smaller than in the wild-type protein, reflecting a different electrostatic distribution on the protein [12].

The analysis of the thermodynamic parameters of PpcAK60 mutants (Table 5.6) shows that heme III is more affected, as expected from the spatial position of Lys^{60} in PpcA structure (Figure 5.14). The heme III reduction potential is lowered by about 20 mV, reflecting the stabilization of its reduced form.

5.1.3.4 Role of Lys^{52} and Lys^{60} in the functional mechanism of PpcA

The analysis of the impact of these parameters on the protein functional mechanism at physiological pH was evaluated by plotting the molar fractions of the individual microstates and the heme oxidation fractions as a function of the solution potential (Figure 5.20 and Figure 5.21).

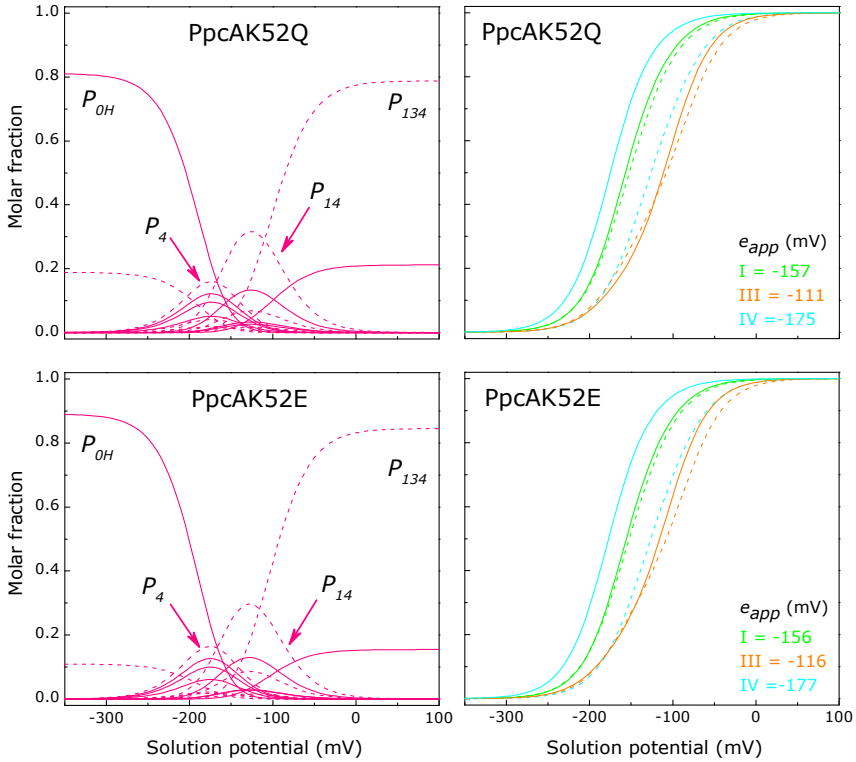

Figure 5.20 – Molar fractions of the 16 individual microstates (left panels) and oxidation fractions of individual hemes (right panels) in PpcAK52 mutants and wild-type cytochromes. The curves were calculated at pH 7.5 as a function of the solution reduction potential using the parameters listed in Table 5.5. In the left panels, solid lines and dashed lines indicate the protonated and deprotonated microstates, respectively. In the right panels, solid and dashed lines represent data for the mutant and wild-type proteins, respectively.

As a result of the removal of a positive charge at position 52, the order of oxidation of the hemes is now IV-I-III while for PpcA was I-IV-III. This reflects the significant decrease of the heme IV e_{app} value in the mutants. Additionally, the contribution of the dominant

microstates is also altered so that a $2e^-$ step coupled with proton transfer is established (left panels in Figure 5.20). Despite the fact that the heme order of oxidation changes, heme III is still the last heme to oxidize and a preferential pathway for electron transfer is maintained.

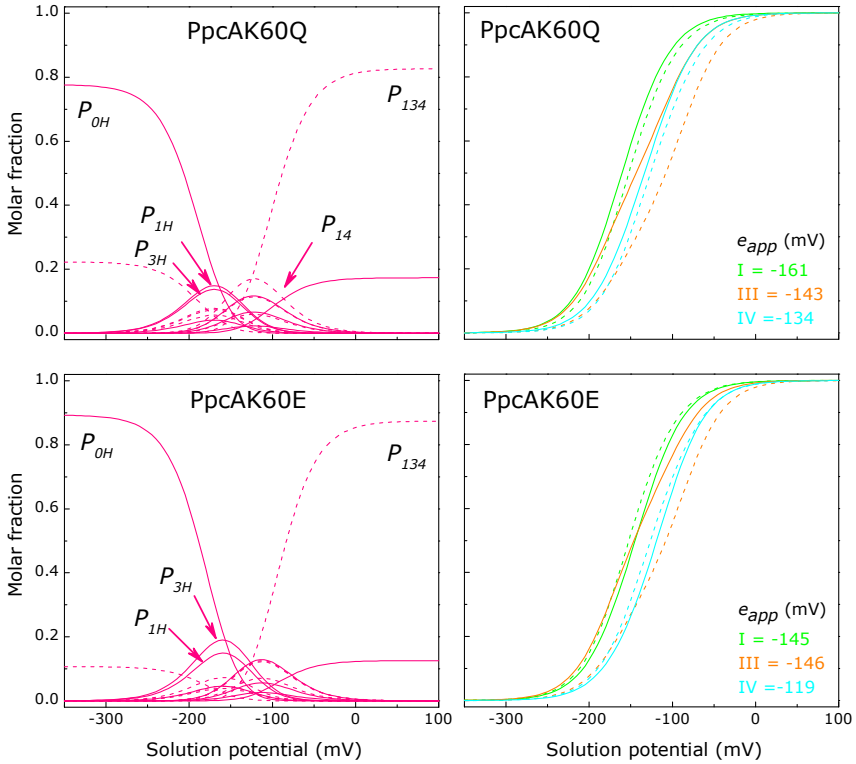

Figure 5.21 – Molar fractions of the 16 individual microstates (left panels) and oxidation fractions of individual hemes (right panels) in PpcAK60 mutants and wild-type cytochromes. The curves were calculated at pH 7.5 as a function of the solution reduction potential using the parameters listed in Table 5.6. In the left panels, solid lines and dashed lines indicate the protonated and deprotonated microstates, respectively. In the right panels, solid and dashed lines represent data for the mutant and wild-type proteins, respectively.

In the case of PpcAK60 mutants, the order of oxidation of the heme groups changes to I-III-IV for PpcAK60Q and to (III,I)-IV for PpcAK60E. The significant decrease of heme III e_{app} makes heme IV the last one to be oxidized, and a preferential pathway for electron transfer is no longer observed. From all the results obtained, it seems that a positive charge at position 60 is crucial for the establishment of a preferential electron transfer pathway on PpcA.

Overall, the results obtained in the lysine mutant families suggest a different role for these residues. Lys^{52} and Lys^{60} are involved in the control of the properties of the redox centers, whereas Lys^{9}, Lys^{18} and Lys^{22} might have a role in the recognition and interaction with the physiological redox partners. In fact, the replacement of Lys^{9} together with another residue (Lys^{10}) in the homologous protein *Dac*$_7$ affected the reactivity of the mutant protein with [Fe] hydrogenase [20].

5.2 Conclusions

The NMR studies of PpcA mutants on residues Phe[15], Lys[52], Met[58] and Lys[60] indicated that the heme core architecture of the protein was not affected by the mutations. The different mutations influenced the heme reduction potentials, redox interactions and redox-Bohr interactions, and altered the balance of the global network of cooperativities. The more notorious effects were observed for residues located in the proximity of heme III, revealing an important role for this heme in the modulation of the functional properties of PpcA (Table 5.7).

Table 5.7 – Summary of the results obtained from the thermodynamic characterization of PpcA mutated forms.

Protein	Order of heme oxidation	Electron transfer pathway
PpcA	I-IV-**III**	$P_{0H} \rightarrow P_{1H} \rightarrow P_{14} \rightarrow P_{134}$
PpcAF15L	(I,III)-IV	No preferential pathway
PpcAM58D	I-(III,IV)	No preferential pathway
PpcAM58K	I-IV-**III**	$P_{0H} \rightarrow P_{14} \rightarrow P_{134}$
PpcAM58N	I-IV-**III**	$P_{0H} \rightarrow P_{14} \rightarrow P_{134}$
PpcAM58S	I-IV-**III**	$P_{0H} \rightarrow P_{1H} \rightarrow P_{14} \rightarrow P_{134}$
PpcAK52Q	IV-I-**III**	$P_{0H} \rightarrow P_{14} \rightarrow P_{134}$
PpcAK52E	IV-I-**III**	$P_{0H} \rightarrow P_{14} \rightarrow P_{134}$
PpcAK60Q	I-III-IV	No preferential pathway
PpcAK60E	(III,I)-IV	No preferential pathway

Indeed, mutations that change the reduction potential of heme III in a way that it is no longer the last heme to oxidize (PpcAF15L, PpcAM58D, PpcAK60Q and PpcAK60E) disrupt, e^-/H^+ energy transduction mechanism. Also, the mutations that increase the reduction potential of heme III in relation to that of the other hemes (PpcAM58K, PpcAM58N, PpcAK52Q and PpcAK52E) change the preferred e^-/H^+ mechanism observed in the wild-type protein. Thus, it can be proposed that the functional role of Phe[15], Lys[52], Met[58] and Lys[60] is to regulate the heme redox properties assuring that heme III is the last heme to oxidize.

This study showed that the functional mechanism of PpcA relies on a fine tuned balance of redox and redox-Bohr interactions that assure a coherent electron transfer pathway coupled to proton transfer, which allows the protein to perform e^-/H^+ energy transduction. The proper tuning of the reduction potentials is fundamental to achieve concerted e^-/H^+ transfer that contributes to cellular energy transduction.

Finally, this work opens up the possibility of testing the physiological relevance of this tuning by evaluating the cellular growth of *G. sulfurreducens* with PpcA replaced by mutated forms.

5.3 References

[1] FA Tezcan, JR Winkler, HB Gray (1998) Effects of ligation and folding on reduction potentials of heme proteins, J. Am. Chem. Soc. 120, 13383-13388.

[2] P Voigt, EW Knapp (2003) Tuning heme redox potentials in the cytochrome *c* subunit of photosynthetic reaction centers, J Biol Chem 278, 51993-52001.

[3] H Akutsu, Y Takayama (2007) Functional roles of the heme architecture and its environment in tetraheme cytochrome *c*, Acc Chem Res 40, 171-178.

[4] AG Mauk, GR Moore (1997) Control of metalloprotein redox potentials: what does site-directed mutagenesis of hemoproteins tell us?, Journal of Biological Inorganic Chemistry 2, 119-125.

[5] L Morgado, VB Paixao, M Schiffer, PR Pokkuluri, M Bruix, CA Salgueiro (2012) Revealing the structural origin of the redox-Bohr effect: the first solution structure of a cytochrome from *Geobacter sulfurreducens*, Biochem J 441, 179-187.

[6] M Pessanha, YY Londer, WC Long, J Erickson, PR Pokkuluri, M Schiffer, et al. (2004) Redox characterization of *Geobacter sulfurreducens* cytochrome c_7: physiological relevance of the conserved residue F15 probed by site-specific mutagenesis, Biochemistry 43, 9909-9917.

[7] PR Pokkuluri, YY Londer, NE Duke, M Pessanha, X Yang, V Orshonsky, et al. (2011) Structure of a novel dodecaheme cytochrome *c* from *Geobacter sulfurreducens* reveals an extended 12nm protein with interacting hemes, J Struct Biol 174, 223-233.

[8] A Dolla, P Arnoux, I Protasevich, V Lobachov, M Brugna, MT Giudici-Orticoni, et al. (1999) Key role of phenylalanine 20 in cytochrome c_3: structure, stability, and function studies, Biochemistry 38, 33-41.

[9] LM Saraiva, CA Salgueiro, J LeGall, WM Van Dongen, AV Xavier (1996) Site-directed mutagenesis of a phenylalanine residue strictly conserved in cytochromes c_3, J Biol Inorg Chem 1, 542-550.

[10] Y Takayama, E Harada, R Kobayashi, K Ozawa, H Akutsu (2004) Roles of noncoordinated aromatic residues in redox regulation of cytochrome c_3 from *Desulfovibrio vulgaris* Miyazaki F, Biochemistry 43, 10859-10866.

[11] JM Dantas, L Morgado, YY Londer, AP Fernandes, RO Louro, PR Pokkuluri, et al. (2012) Pivotal role of the strictly conserved aromatic residue F15 in the cytochrome c_7 family, J Biol Inorg Chem 17, 11-24.

[12] RO Louro, T Catarino, CM Paquete, DL Turner (2004) Distance dependence of interactions between charged centres in proteins with common structural features, FEBS Lett 576, 77-80.

[13] DL Turner, CA Salgueiro, T Catarino, J LeGall, AV Xavier (1996) NMR studies of cooperativity in the tetrahaem cytochrome c_3 from *Desulfovibrio vulgaris*, Eur J Biochem 241, 723-731.

[14] RO Louro, T Catarino, DL Turner, MA Piçarra-Pereira, I Pacheco, J LeGall, et al. (1998) Functional and mechanistic studies of cytochrome c_3 from *Desulfovibrio gigas*: thermodynamics of a "proton thruster", Biochemistry 37, 15808-15815.

[15] CA Salgueiro, DL Turner, JL Gall, AV Xavier, J LeGall (1997) Reevaluation of the redox and redox-Bohr cooperativity in tetrahaem *Desulfovibrio vulgaris* (Miyazaki F) cytochrome c_3, Journal of Biological Inorganic Chemistry 2, 343-349.

[16] AC Messias, DH Kastrau, HS Costa, J LeGall, DL Turner, H Santos, et al. (1998) Solution structure of *Desulfovibrio vulgaris* (Hildenborough) ferrocytochrome c_3: structural basis for functional cooperativity, J Mol Biol 281, 719-739.

[17] E Harada, Y Fukuoka, T Ohmura, A Fukunishi, G Kawai, T Fujiwara, et al. (2002) Redox-coupled conformational alternations in cytochrome c_3 from *D. vulgaris* Miyazaki F on the basis of its reduced solution structure, J Mol Biol 319, 767-778.

[18] L Brennan, DL Turner, AC Messias, ML Teodoro, J LeGall, H Santos, et al. (2000) Structural basis for the network of functional cooperativities in cytochrome c_3 from *Desulfovibrio gigas*: solution structures of the oxidised and reduced states, J Mol Biol 298, 61-82.

[19] BM Fonseca, CM Paquete, CA Salgueiro, RO Louro (2011) The role of intramolecular interactions in the functional control of multiheme cytochromes *c*, FEBS Lett, *in press*, doi:10.1016/j.febslet.2011.1008.1019.

[20] M Assfalg, I Bertini, P Turano, M Bruschi, MC Durand, MT Giudici-Orticoni, et al. (2002) A quick solution structure determination of the fully oxidized double mutant K9-10A cytochrome c_7 from *Desulfuromonas acetoxidans* and mechanistic implications, J Biomol NMR 22, 107-122.

[4] Partially reproduced from L Morgado, AP Fernandes, YY Londer, M Bruix, CA Salgueiro (2010) One simple step in the identification of the cofactors signals, one giant leap for the solution structure determination of multiheme proteins, Biochem Biophys Res Commun 393, 466-470 (http://dx.doi.org/10.1016/j.bbrc.2010.02.024), according to the Editors' Copyright Policy.

6. ONGOING STUDIES

As any project seldom has a final end, this one is not an exception. In this chapter the ongoing studies involving the triheme cytochrome PpcA are described.

6.1 Studies on PpcA in the paramagnetic oxidized state

As already stated in Chapter 4, the next step towards PpcA characterization is the determination of its solution structure in the oxidized state. This will allow the analysis of redox-linked conformational changes.

6.1.1 Assignment of the heme resonances

As it was described in Chapter 1, the heme groups of PpcA are low spin (S = ½) in the oxidized form. Thus, the unpaired electron of each heme iron exerts significant paramagnetic shifts on the heme signals and nearby residues. Consequently, the same type of signals is differently affected by the paramagnetic centers, showing different levels of broadness and being spread all over the entire NMR spectral width (Figure 1.4 – Chapter 1).

The acquisition of ^{1}H-^{13}C HSQC NMR spectra may be used to assist the assignment of the heme substituents signals, since the dipolar shifts of the carbon nuclei attached to the pyrrole β-carbons are very small and, unlike the protons bonded to them, their Fermi contact shifts are directly proportional to the spin density on the pyrrole β-carbons [1]. A few ^{1}H-^{13}C HSQC NMR studies carried out on natural abundance samples have been reported for tetraheme cytochromes c_3 [2-5]. However, the complete assignment of both proton and carbon resonances of the heme substituents could not be accomplished solely from the analysis of these spectra. This difficulty arises from the overlap between the heme signals with those of the polypeptide chain, which are also displaced from their typical positions in paramagnetic proteins, making their assignment extremely complex. This is well illustrated by the 2D ^{1}H-^{13}C HSQC NMR spectrum (blue contours in Figure 6.1) obtained for the unlabeled oxidized PpcA. In this spectrum, both the heme cofactors and polypeptide chain ^{1}H-^{13}C connectivities are observable and cannot be distinguished.

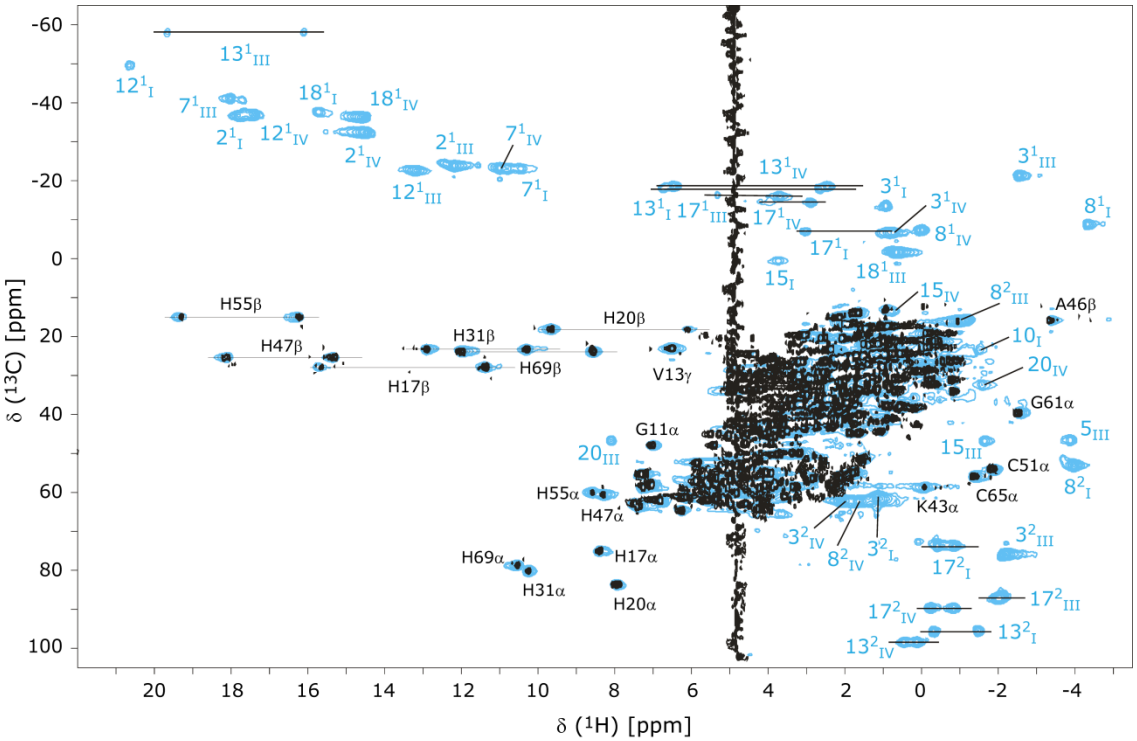

Figure 6.1 – 2D-^{1}H-^{13}C HSQC NMR spectra of the unlabeled (blue contours) and labeled (black contours) PpcA (1.2 mM) obtained at 25 °C, with 640 and 80 scans, respectively. In order to not overcrowd the figure only the resonances separated from the main signal envelope are indicated. Blue and black labels indicate the heme substituents and the polypeptide resonances, respectively. The peaks of the protons connected to the same carbon atom (CH_2 groups) are linked by a straight line.

To overcome this difficulty, PpcA was double labeled (^{13}C/^{15}N), exclusively on its polypeptide chain. The yield of double-labeled protein obtained after purification was 3.6 mg per liter of culture, sufficient for all the experiments. The labeled PpcA was used to reveal the connectivities arising entirely from the polypeptide chain in the 2D ^{1}H-^{13}C HSQC NMR spectrum (black contours in Figure 6.1). This is possible because the heme precursor (δ-aminolevulinic acid) added into the minimal media was not labeled and, consequently, the heme signals are not observable in a short (80 scans) ^{1}H-^{13}C HSQC NMR spectrum. Therefore, by simple comparison of the two NMR spectra, the heme cofactors signals and those of the polypeptide chain can be easily discriminated and subsequently assigned. This comparison allowed identifying more than 90% of the heme substituents signals (Table A.11 – Appendix), the exception being the signals that are severely broad or appear in extremely overcrowded spectral regions.

As mentioned above, the amino acid residues located in the close proximity of the paramagnetic hemes are strongly affected by the dipolar field of the heme centers, and are displaced from their typical positions. This is the case of the αCH and βCH_2 connectivities of the six heme axial histidines (His^{17}, His^{20}, His^{31}, His^{47}, His^{55} and His^{69}); αCH of Gly^{11}, Lys^{43}, Cys^{51}, Gly^{61}, Cys^{65}; βCH_3 of Ala^{46} and γCH_3 of Val^{13}. The displacement of these signals over the entire spectrum, as illustrated in Figure 6.1, further complicates the assignment. The specific labeling of the polypeptide chain allows identifying these amino acid signals. Besides

signal assignment, this identification is of major importance for structure determination as it identifies the residues closer to the heme groups.

This strategy allows the straightforward and unambiguous discrimination between the heme and the polypeptide chain signals in the ^{1}H-^{13}C HSQC NMR spectra. The clear identification of these signals is of major importance in multiheme proteins, since the displacement of the resonance by paramagnetic effects overcomplicates their assignment and the concomitant high-quality structural restraints, a crucial step in protein solution structure determination. The difficulties in obtaining such data are the main reasons for the scarcity of solution structures of multiheme proteins. This step is even more crucial in structure determination as the number of heme cofactors increases, as for example in dodecaheme cytochromes for which a total of 240 cofactor protons need to be identified.

Overall, the application of this strategy will have an important impact, opening new routes in the understanding of the structural and functional mechanisms in the super-family of multiheme proteins.

6.1.2 Solution structure determination

In the oxidized state, due to the unpaired electrons on the metal ions of the heme groups, the protein is paramagnetic. This fact makes more difficult not only the assignment of the protein resonances, but also the determination of its structure since the intensity of the cross-peaks in the 2D-^{1}H-NOESY is also affected. This fact is minimized in spectra acquired at shorter mixing times.

Double labeled $^{13}C/^{15}N$-PpcA has been produced and at the moment 90% of the resonances were assigned.

For structure calculation, extra non-standard residues in relation to the calculations in the reduced form have been used (Appendix A.4.1). These residues are two types of axial histidine ligands that consider the magnetic axes and the torsion angle that defines the orientation of the histidine ring plane with respect to the heme plane [6-8], introducing new fixed upper limit distances.

Two sets of peaks obtained at different mixing times are being used for structure calculation with PARADYANA in the oxidized state, together with dipolar shifts determined by subtracting the shifts for the reduced protein from those for the oxidized protein [8,9]. These dipolar shifts are used in structure refinement since these shifts depend on the position of the nucleus relative to the paramagnetic centers and their magnetic axes. Volume restraints are also corrected for paramagnetic leakage, as previously described [8]. Preliminary calculations have been performed; however the structure is not yet defined.

6.2 *In vivo* studies of mutated forms of PpcA

Having a large family of mutated PpcA forms characterized, it's possible to evaluate the effect that some of these mutations would have on the bacteria abilities, and verify if *G. sulfurreducens* bioremediation capacities are affected.

This work was developed in collaboration with the group of Prof. Derek Lovley (Geobacter Project – www.geobacter.org) at the Department of Microbiology, University of Massachusetts in Amherst, Massachusetts, USA, where all the tools necessary for the manipulation of *G. sulfurreducens* genetic system were available.

From the results described in Chapter 5, four mutants were selected for *in vivo* studies in *G. sulfurreducens*. These were PpcAF15L, PpcAK52E, PpcAM58K and PpcAM58S.

A *G. sulfurreducens* strain with the PpcA coding gene knocked-out (DL3) was already available in the laboratory [10], as well as an expression vector (pRG5) that allows complementation studies of *G. sulfurreducens* knockout mutants [11]. This plasmid contains a spectinomycin resistance cassette, the *taclac* promoters and a multiple cloning site [11].

PpcA coding gene was cloned in pRG5 and site-directed mutagenesis was used for the preparation of the complementation plasmids with the different mutations (Appendix A.4.2). These plasmids were electroporated into *G. sulfurreducens* DL3, and cultures were allowed to grow in plates inside an anaerobic glove bag. After obtaining isolated mutant colonies, cells were transferred to liquid media with acetate as electron donor and fumarate as electron acceptor (NBAF media) in order to evaluate their viability.

All the strains grew in NBAF media and the next step will be to study growth in media with different electron acceptors, as Fe(III) citrate, Fe(III) oxides and Mn(IV) oxides.

6.3 Interaction studies with PpcA putative redox partners

Having all the resonances assigned for PpcA in both redox states, is possible to use the NMR spectra as maps to locate specific interactions with other proteins [12-14].

Chemical shift perturbation has been used to map protein interfaces by analysis of perturbations of the chemical shifts on a 2D-^{1}H-^{15}N-HSQC spectrum of one protein when a putative unlabeled partner protein is titrated in the sample [13,14]. The chemical shifts are affected when there is an interaction causing changes on the protein interfaces.

From the predicted cellular localization, MacA was proposed to be PpcA upstream redox partner in the extracellular electron transfer to Fe(III) oxides (Figure 1.1 – Chapter 1) [15,16]. MacA (GSU0466) is a 36 kDa protein containing two *c*-type heme groups that shows sequence homology to cytochrome *c* peroxidases [17,18].

The gene coding for MacA was successfully cloned from *G. sulfurreducens* genomic DNA and inserted into vector pVA203 [19], that contains the OmpA leader sequence from *E. coli* (Appendix A.4.3). At the moment, preliminary tests for overexpression of MacA in *E. coli* are being performed.

6.4 References

[1] JR Bolton, GK Fraenkel (1964) Electron Spin Resonance Study of the Pairing Theorem for Alternant Hydrocarbons: ^{13}C Splittings in the Anthracene Positive and Negative Ions, J Chem Phys 40, 3307-3320.

[2] RO Louro, IJ Correia, L Brennan, IB Coutinho, AV Xavier, DL Turner (1998) Electronic Structure of Low-Spin Ferric Porphyrins: ^{13}C NMR Studies of the Influence of Axial Ligand Orientation, J Am Chem Soc 120, 13240-13247.

[3] RO Louro, M Pessanha, GA Reid, SK Chapman, DL Turner, CA Salgueiro (2002) Determination of the orientation of the axial ligands and of the magnetic properties of the haems in the tetrahaem ferricytochrome from *Shewanella frigidimarina*, FEBS Lett 531, 520-524.

[4] DL Turner, HS Costa, IB Coutinho, J Legall, AV Xavier (1997) Assignment of the ligand geometry and redox potentials of the trihaem ferricytochrome c_3 from *Desulfuromonas acetoxidans*, Eur J Biochem 243, 474-481.

[5] DL Turner, CA Salgueiro, P Schenkels, J LeGall, AV Xavier (1995) Carbon-13 NMR studies of the influence of axial ligand orientation on haem electronic structure, Biochim Biophys Acta 1246, 24-28.

[6] DL Turner, L Brennan, SG Chamberlin, RO Louro, AV Xavier (1998) Determination of solution structures of paramagnetic proteins by NMR, Eur Biophys J 27, 367-375.

[7] AC Messias, DH Kastrau, HS Costa, J LeGall, DL Turner, H Santos, AV Xavier (1998) Solution structure of *Desulfovibrio vulgaris* (Hildenborough) ferrocytochrome c_3: structural basis for functional cooperativity, J Mol Biol 281, 719-739.

[8] VB Paixão, H Vis, DL Turner (2010) Redox linked conformational changes in cytochrome c_3 from *Desulfovibrio desulfuricans* ATCC 27774, Biochemistry 49, 9620-9629.

[9] AC Messias, AP Aguiar, L Brennan, CA Salgueiro, LM Saraiva, AV Xavier, DL Turner (2006) Solution structures of tetrahaem ferricytochrome c_3 from *Desulfovibrio vulgaris* (Hildenborough) and its K45Q mutant: the molecular basis of cooperativity, Biochim Biophys Acta 1757, 143-153.

[10] JR Lloyd, C Leang, AL Hodges Myerson, MV Coppi, S Cuifo, B Methe, SJ Sandler, DR Lovley (2003) Biochemical and genetic characterization of PpcA, a periplasmic *c*-type cytochrome in *Geobacter sulfurreducens*, Biochem J 369, 153-161.

[11] BC Kim, C Leang, YH Ding, RH Glaven, MV Coppi, DR Lovley (2005) OmcF, a putative *c*-type monoheme outer membrane cytochrome required for the expression of other outer membrane cytochromes in *Geobacter sulfurreducens*, J Bacteriol 187, 4505-4513.

[12] N Yahata, T Saitoh, Y Takayama, K Ozawa, H Ogata, Y Higuchi, H Akutsu (2006) Redox interaction of cytochrome c_3 with [NiFe] hydrogenase from *Desulfovibrio vulgaris* Miyazaki F, Biochemistry 45, 1653-1662.

[13] MR O'Connell, R Gamsjaeger, JP Mackay (2009) The structural analysis of protein-protein interactions by NMR spectroscopy, Proteomics 9, 5224-5232.

[14] ER Zuiderweg (2002) Mapping protein-protein interactions in solution by NMR spectroscopy, Biochemistry 41, 1-7.

[15] DR Lovley (2006) Bug juice: harvesting electricity with microorganisms, Nat Rev Microbiol 4, 497-508.

[16] KA Weber, LA Achenbach, JD Coates (2006) Microorganisms pumping iron: anaerobic microbial iron oxidation and reduction, Nat Rev Microbiol 4, 752-764.

[17] M Hoffmann, J Seidel, O Einsle (2009) CcpA from *Geobacter sulfurreducens* is a basic di-heme cytochrome c peroxidase, J Mol Biol 393, 951-965.

[18] BA Methé, KE Nelson, JA Eisen, IT Paulsen, W Nelson, JF Heidelberg, D Wu, M Wu, N Ward, MJ Beanan, RJ Dodson, R Madupu, LM Brinkac, SC Daugherty, RT DeBoy, AS Durkin, M Gwinn, JF Kolonay, SA Sullivan, DH Haft, J Selengut, TM Davidsen, N Zafar, O White, B Tran, C Romero, HA Forberger, J Weidman, H Khouri, TV Feldblyum, TR Utterback, SE Van Aken, DR Lovley, CM Fraser (2003) Genome of *Geobacter sulfurreducens*: metal reduction in subsurface environments, Science 302, 1967-1969.

[19] PR Pokkuluri, YY Londer, NE Duke, J Erickson, M Pessanha, CA Salgueiro, M Schiffer (2004) Structure of a novel c_7-type three-heme cytochrome domain from a multidomain cytochrome *c* polymer, Protein Sci 13, 1684-1692.

FINAL CONSIDERATIONS

7. FINAL CONSIDERATIONS

Studies on *Geobacter* species have been revealing unique characteristics that have not been described before in any other microorganism [1]. *Geobacter* are able to transfer electrons to extracellular acceptors, as different as Fe(III) oxides and the surface of electrodes. This ability was shown to be possible due to the formation of pili and the association of membrane cytochromes to its surface [2,3].

The presence of a large number of cytochromes in *Geobacter* have shown to be important for the electron transfer between the different cell compartments and the final electron acceptors [4-6], as well as electron capacitors, allowing the storage of electrons when electron acceptors are temporarily unavailable [7,8].

The work developed in this thesis aimed to contribute to the elucidation of *G. sulfurreducens* mechanisms for electron transfer for extracellular acceptors in the periplasm (Figure 7.1).

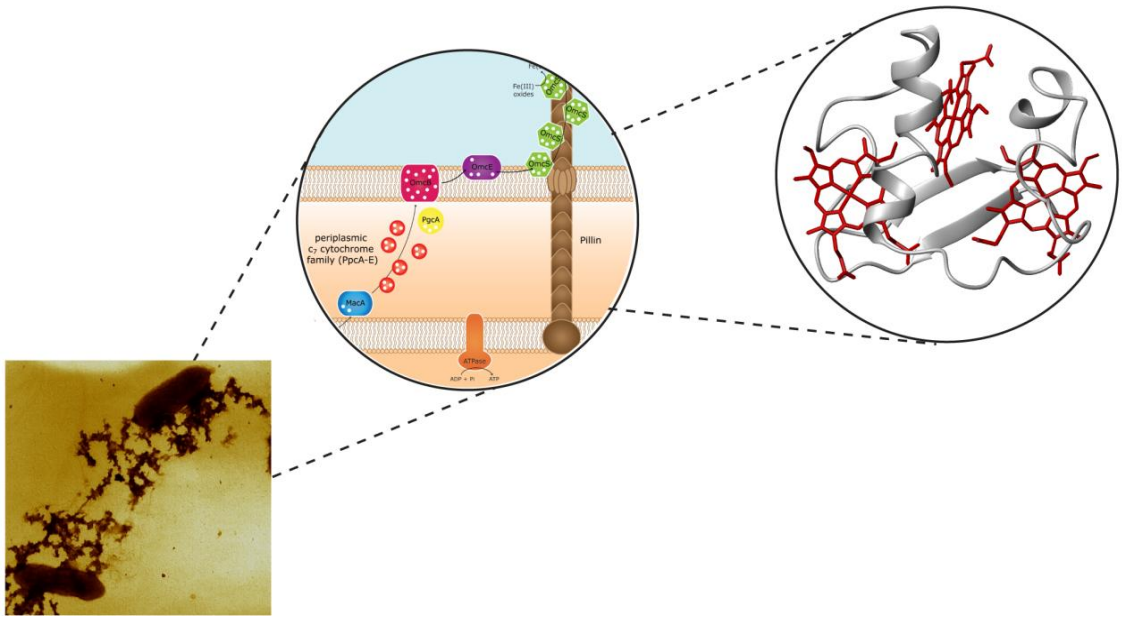

Figure 7.1 – Figurative representation of the work developed. The picture on the left show Fe(III) oxides (black precipitates) associated with *G. sulfurreducens* pili (Photo credit: Gemma Reguera, www.geobacter.org); the figure in the center represents the proposed mechanism for extracellular electron transfer by *G. sulfurreducens*, and the figure on the right represents PpcA solution structure.

The periplasmic triheme cytochromes family was thermodynamically characterized and the distinct detailed properties observed revealed different functional mechanisms with respect to reduction potentials and pK_a values, suggesting that these proteins might interact with distinct partners [9,10]. The determination of PpcA solution structure [11], as well as the characterization of PpcA mutated forms [12], allowed to reveal important aspects of its functional mechanism.

The results presented in this thesis brought new insights to the functional mechanisms of the complex network of redox proteins found in the periplasm of *G. sulfurreducens*, as well as new tools that open new routes for the study of these proteins [13].

7.1 References

[1] DR Lovley, T Ueki, T Zhang, NS Malvankar, PM Shrestha, KA Flanagan, et al. (2011) *Geobacter*: The Microbe Electric's Physiology, Ecology, and Practical Applications, Adv Microb Physiol 59, 1-100.

[2] G Reguera, KD McCarthy, T Mehta, JS Nicoll, MT Tuominen, DR Lovley (2005) Extracellular electron transfer via microbial nanowires, Nature 435, 1098-1101.

[3] C Leang, X Qian, T Mester, DR Lovley (2010) Alignment of the *c*-type cytochrome OmcS along pili of *Geobacter sulfurreducens*, Appl Environ Microbiol 76, 4080-4084.

[4] YH Ding, KK Hixson, MA Aklujkar, MS Lipton, RD Smith, DR Lovley, et al. (2008) Proteome of *Geobacter sulfurreducens* grown with Fe(III) oxide or Fe(III) citrate as the electron acceptor, Biochim Biophys Acta 1784, 1935-1941.

[5] YH Ding, KK Hixson, CS Giometti, A Stanley, A Esteve-Núñez, T Khare, et al. (2006) The proteome of dissimilatory metal-reducing microorganism *Geobacter sulfurreducens* under various growth conditions, Biochim Biophys Acta 1764, 1198-1206.

[6] ES Shelobolina, MV Coppi, AA Korenevsky, LN Didonato, SA Sullivan, H Konishi, et al. (2007) Importance of *c*-type cytochromes for U(VI) reduction by *Geobacter sulfurreducens*, BMC Microbiol 7, 16.

[7] DR Lovley (2008) Extracellular electron transfer: wires, capacitors, iron lungs, and more, Geobiology 6, 225-231.

[8] A Esteve-Núñez, J Sosnik, P Visconti, DR Lovley (2008) Fluorescent properties of *c*-type cytochromes reveal their potential role as an extracytoplasmic electron sink in *Geobacter sulfurreducens*, Environ Microbiol 10, 497-505.

[9] L Morgado, M Bruix, V Orshonsky, YY Londer, NE Duke, X Yang, et al. (2008) Structural insights into the modulation of the redox properties of two *Geobacter sulfurreducens* homologous triheme cytochromes, Biochim Biophys Acta 1777, 1157-1165.

[10] L Morgado, M Bruix, M Pessanha, YY Londer, CA Salgueiro (2010) Thermodynamic characterization of a triheme cytochrome family from *Geobacter sulfurreducens* reveals mechanistic and functional diversity, Biophys J 99, 293-301.

[11] L Morgado, VB Paixao, M Schiffer, PR Pokkuluri, M Bruix, CA Salgueiro (2012) Revealing the structural origin of the redox-Bohr effect: the first solution structure of a cytochrome from *Geobacter sulfurreducens*, Biochem J 441, 179-187.

[12] JM Dantas, L Morgado, YY Londer, AP Fernandes, RO Louro, PR Pokkuluri, et al. (2012) Pivotal role of the strictly conserved aromatic residue F15 in the cytochrome c_7 family, J Biol Inorg Chem 17, 11-24.

[13] L Morgado, AP Fernandes, YY Londer, M Bruix, CA Salgueiro (2010) One simple step in the identification of the cofactors signals, one giant leap for the solution structure determination of multiheme proteins, Biochem Biophys Res Commun 393, 466-470.

APPENDIX

A. APPENDIX

A.1 Assignment of the heme resonances of PpcA, PpcB, PpcD and PpcE in the reduced form

Table A.1 – Chemical shifts (ppm) of the heme protons of PpcA, PpcB, PpcD and PpcE in the reduced state at pH 8.0 and 15 °C.

Heme substituent	Cytochrome	Heme I	Heme III	Heme IV
5H	PpcA	9.65	10.58	9.02
	PpcB	9.71	10.63	9.00
	PpcD	9.86	9.71	9.08
	PpcE	9.43	9.83	8.98
10H	PpcA	9.12	9.86	9.33
	PpcB	9.26	9.87	9.27
	PpcD	8.08	9.86	9.40
	PpcE	9.39	9.75	9.32
15H	PpcA	9.26	9.45	9.51
	PpcB	9.27	9.51	9.40
	PpcD	9.59	9.36	9.54
	PpcE	9.28	9.52	9.64
20H	PpcA	9.50	10.14	9.39
	PpcB	9.50	10.21	9.39
	PpcD	8.74	10.11	9.47
	PpcE	9.42	10.27	9.51
2^1CH_3	PpcA	3.56	4.35	3.61
	PpcB	3.59	4.38	3.60
	PpcD	3.32	4.52	3.67
	PpcE	3.60	4.37	3.68
7^1CH_3	PpcA	3.58	4.14	3.02
	PpcB	3.65	4.14	3.01
	PpcD	3.53	3.92	2.97
	PpcE	3.46	4.06	2.99
12^1CH_3	PpcA	2.55	3.50	3.95
	PpcB	2.73	3.52	3.61
	PpcD	2.90	3.50	3.91
	PpcE	3.39	3.20	3.63
18^1CH_3	PpcA	3.34	3.86	3.34
	PpcB	3.36	4.02	3.34
	PpcD	3.23	3.87	3.38
	PpcE	3.30	4.05	3.45
3^1H	PpcA	6.30	6.91	6.04
	PpcB	6.30	6.93	5.96
	PpcD	6.16	6.66	5.98
	PpcE	6.20	6.65	5.87
8^1H	PpcA	6.29	6.60	6.28
	PpcB	6.43	6.53	6.28
	PpcD	5.48	6.61	6.28
	PpcE	6.47	6.44	6.23
3^2CH_3	PpcA	2.14	1.73	2.06
	PpcB	2.17	1.90	2.04
	PpcD	2.34	2.85	2.08
	PpcE	2.29	2.34	2.12
8^2CH_3	PpcA	1.79	2.98	1.55
	PpcB	2.11	2.97	1.48
	PpcD	1.62	2.96	1.50
	PpcE	2.06	3.04	1.36

A.2 Backbone, side chain and heme resonance assignments of PpcA in the reduced state

Table A.2 – Chemical shifts (ppm) of PpcA in the reduced state at pH 7.1 and 25 °C. The chemical shifts are deposited in the Biological Magnetic Resonance Data Bank (BMRB, http://www.bmrb.wisc.edu) under accession number 16842.

Residue number	Residue type	Atom	Chemical shift (ppm)
1	**ALA**	HA	3.775
		HB	1.269
2	**ASP**	HA	4.814
		HB2	2.200
		HB3	3.754
3	**ASP**	HN	7.355
		HA	4.611
		HB2	2.017
		HB3	2.059
		N	116.929
4	**ILE**	HN	8.348
		HA	4.004
		HB	1.473
		HD1	-0.486
		HG12	0.534
		HG2	1.016
		N	121.916
5	**VAL**	HN	8.792
		HA	4.494
		HB	1.984
		HG1	0.747
		HG2	0.857
		N	128.142
6	**LEU**	HN	9.545
		HA	4.963
		HB2	2.501
		HB3	2.211
		HD1	1.634
		HD2	1.432
		HG	2.156
		N	133.341
7	**LYS**	HN	8.614
		HA	4.270
		HB2	1.785
		HB3	1.921
		HD2	1.714
		HD3	1.750
		HE2	3.062
		HE3	3.124
		HG2	1.514
		HG3	1.642
		N	124.135
8	**ALA**	HN	8.653
		HA	4.868
		HB	0.839
		N	124.079
9	**LYS**	HN	10.359
		HA	4.012
		HB2	1.959
		HB3	1.891
		HD2	1.850
		HE2	3.176
		HG2	1.582
		N	125.272
10	**ASN**	HN	8.849
		HA	4.289
		HB2	1.877
		HB3	2.145
		HD21	1.093
		HD22	5.463
		N	114.016
		ND2	109.040
11	**GLY**	HN	6.963
		HA2	3.085
		HA3	3.463
		N	110.585

Residue number	Residue type	Atom	Chemical shift (ppm)
12	**ASP**	HN	8.080
		HA	4.291
		HB2	2.255
		HB3	2.372
		N	129.379
13	**VAL**	HN	8.613
		HA	4.187
		HB	2.368
		HG1	1.529
		HG2	-0.834
		N	121.753
14	**LYS**	HN	9.005
		HA	4.499
		HB2	1.772
		HB3	1.918
		HD2	1.630
		HE2	2.857
		HG2	1.105
		HG3	1.247
		N	129.348
15	**PHE**	HN	9.220
		HA	5.518
		HB2	3.452
		HB3	3.266
		HD1	6.105
		HD2	5.549
		HE1	6.239
		HE2	0.716
		HZ	5.905
		N	128.576
16	**PRO**	HA	4.580
		HB2	1.584
		HD2	2.692
		HD3	4.405
		HG2	0.68
		HG3	1.838

Residue number	Residue type	Atom	Chemical shift (ppm)
17	**HIS**	HN	6.606
		HA	0.927
		HB2	0.536
		HB3	1.158
		HD1	8.681
		HD2	-0.484
		HE1	1.227
		N	132.191
		ND1	166.694
18	**LYS**	HN	7.304
		HA	2.633
		HB2	0.966
		HB3	1.165
		HD2	1.022
		HE2	2.485
		HG2	0.684
		HG3	0.748
		N	118.010
19	**ALA**	HN	7.073
		HA	3.397
		HB	0.682
		N	120.296
20	**HIS**	HN	6.332
		HA	2.503
		HB2	1.053
		HB3	1.497
		HD1	7.917
		HD2	1.106
		HE1	1.165
		N	116.314
		ND1	163.583
21	**GLN**	HN	6.891
		HA	4.049
		HB2	1.553
		HB3	1.450
		HE21	1.103
		HE22	4.556
		HG2	0.305
		HG3	1.328
		N	117.409
		NE2	105.393

Residue number	Residue type	Atom	Chemical shift (ppm)
22	**LYS**	HN	6.632
		HA	4.013
		HB2	1.529
		HB3	1.615
		HD2	1.449
		HE2	2.785
		HG2	1.208
		HG3	1.277
		N	115.057
23	**ALA**	HN	6.991
		HA	4.217
		HB	1.227
		N	120.221
24	**VAL**	HN	8.386
		HA	4.615
		HB	2.728
		HG1	1.535
		HG2	1.306
		N	120.630
25	**PRO**	HA	4.770
		HB2	2.199
		HB3	2.385
		HD2	3.676
		HD3	3.898
		HG2	2.094
26	**ASP**	HN	7.827
		HA	5.107
		HB2	2.763
		HB3	3.011
		N	117.455
27	**CYS**	HN	8.574
		HA	4.986
		HB2	2.582
		HB3	2.480
		N	123.666
28	**LYS**	HN	8.107
		HA	3.519
		HB2	1.265
		HB3	1.737
		HD2	1.605
		HE2	2.905
		HG2	1.634
		HG3	1.334
		N	114.398
29	**LYS**	HN	7.776
		HA	4.061
		HB2	1.894
		HB3	2.158
		HD2	1.970
		HD3	2.067
		HE2	3.370
		HG2	1.819
		HG3	2.248
		N	118.555
30	**CYS**	HN	6.309
		HA	4.654
		HB2	1.026
		HB3	2.264
		N	111.535
31	**HIS**	HN	7.125
		HA	3.118
		HB2	0.898
		HD1	8.500
		HD2	0.563
		HE1	1.394
		N	118.451
		ND1	163.533
32	**GLU**	HN	8.019
		HA	3.722
		HB2	1.740
		HB3	1.858
		HG2	2.062
		N	125.219
33	**LYS**	HN	8.211
		HA	4.245
		HB2	1.433
		HB3	1.887
		HD2	1.522
		HE2	2.869
		HG2	1.172
		HG3	1.299
		N	114.956
34	**GLY**	HN	6.658
		HA2	3.351
		HA3	4.026
		N	107.392

Residue number	Residue type	Atom	Chemical shift (ppm)
35	**PRO**	HA	0.741
		HB2	1.692
		HB3	1.734
		HD2	3.131
		HD3	3.223
		HG2	1.156
		HG3	2.073
36	**GLY**	HN	3.888
		HA2	3.362
		HA3	4.023
		N	109.171
37	**LYS**	HN	7.982
		HA	4.121
		HB2	1.694
		HD2	1.915
		HG2	1.644
		HG3	1.798
		N	116.609
38	**ILE**	HN	10.233
		HA	3.718
		HB	1.599
		HD1	-0.47
		HG12	-0.203
		HG13	0.66
		HG2	0.827
		N	128.245
39	**GLU**	HN	8.626
		HA	4.050
		HB2	1.893
		HG2	2.206
		N	130.735
40	**GLY**	HN	9.163
		HA2	3.809
		HA3	4.136
		N	113.031
41	**PHE**	HN	8.006
		HA	4.408
		HB2	3.369
		HB3	3.293
		HD2	7.654
		HE2	7.993
		HZ	8.257
		N	121.572
42	**GLY**	HN	5.929
		HA2	4.286
		N	114.663
43	**LYS**	HN	8.962
		HA	2.433
		HB2	1.394
		HD2	1.288
		HD3	-0.599
		HE2	2.177
		HE3	2.268
		HG2	-1.275
		HG3	1.757
		N	122.906
44	**GLU**	HN	8.071
		HA	3.117
		HB2	1.617
		HB3	1.668
		HG2	1.964
		HG3	2.004
		N	114.891
45	**MET**	HN	7.647
		HA	3.931
		HB2	2.399
		HB3	1.762
		HE	2.119
		HG2	2.612
		HG3	1.674
		N	117.869
46	**ALA**	HN	8.009
		HA	4.095
		HB	0.817
		N	122.299
47	**HIS**	HN	6.989
		HA	2.763
		HB2	1.419
		HB3	1.564
		HD1	9.601
		HD2	0.7
		HE1	1.498
		N	113.277
		ND1	164.829

Residue number	Residue type	Atom	Chemical shift (ppm)
48	**GLY**	HN	6.716
		HA2	4.029
		HA3	3.355
		N	109.441
49	**LYS**	HN	8.754
		HA	3.748
		HB2	1.888
		HD2	1.674
		HE2	2.996
		HG2	1.471
		N	124.763
50	**GLY**	HN	8.484
		HA2	4.408
		HA3	3.746
		N	105.588
51	**CYS**	HN	6.721
		HA	5.646
		HB2	3.610
		HB3	2.627
		N	111.007
52	**LYS**	HN	7.998
		HA	2.504
		HB2	1.289
		HG2	1.038
		HG3	1.081
		N	120.154
53	**GLY**	HN	8.521
		HA2	3.591
		HA3	3.349
		N	102.454
54	**CYS**	HN	6.597
		HA	4.423
		HB2	2.452
		HB3	3.709
		N	120.751
55	**HIS**	HN	5.405
		HA	3.741
		HB2	1.649
		HB3	1.427
		HD1	9.601
		HD2	1.085
		HE1	1.590
		N	117.652
		ND1	164.845
56	**GLU**	HN	7.993
		HA	3.648
		HB2	1.954
		HB3	1.785
		HG2	1.863
		HG3	2.116
		N	116.899
57	**GLU**	HN	7.527
		HA	4.041
		HB2	2.207
		HG2	2.326
		HG3	2.394
		N	120.415
58	**MET**	HN	8.859
		HA	4.378
		HB2	2.239
		HB3	2.410
		HE	2.667
		HG2	2.969
		HG3	3.420
		N	115.185
59	**LYS**	HN	7.711
		HA	3.730
		HB2	2.167
		HB3	1.378
		HD2	1.951
		HG2	1.339
		N	114.315
60	**LYS**	HN	7.592
		HA	4.311
		HB2	1.666
		HB3	2.098
		HD2	1.894
		HD3	1.798
		HE2	3.306
		HG2	1.624
		HG3	2.054
		N	118.457
61	**GLY**	HN	7.566
		HA2	2.558
		HA3	1.148
		N	103.599

Residue number	Residue type	Atom	Chemical shift (ppm)
62	**PRO**	HA	3.980
		HB2	1.974
		HB3	2.014
		HD2	-0.711
		HD3	2.453
		HG2	1.017
		HG3	1.911
63	**THR**	HN	8.305
		HA	4.409
		HB	4.265
		HG2	0.694
		N	108.684
64	**LYS**	HN	8.462
		HA	5.157
		HB2	1.707
		HB3	2.140
		HD2	1.730
		HE2	3.024
		HG2	1.534
		HG3	1.585
		N	124.087
65	**CYS**	HN	8.755
		HA	4.829
		HB2	2.741
		HB3	2.844
		N	117.936
66	**GLY**	HN	8.855
		HA2	3.527
		HA3	3.952
		N	101.786
67	**GLU**	HN	7.719
		HA	4.181
		HB2	2.409
		HB3	2.319
		HG2	2.140
		HG3	2.228
		N	116.438
68	**CYS**	HN	6.447
		HA	4.708
		HB2	1.322
		HB3	2.112
		N	114.494
69	**HIS**	HN	6.893
		HA	2.770
		HB2	1.240
		HB3	1.020
		HD1	9.004
		HD2	0.746
		HE1	0.912
		N	118.048
		ND1	166.312
70	**LYS**	HN	7.032
		HA	4.233
		HB2	1.638
		HD2	1.593
		HE2	2.953
		HG2	1.146
		HG3	1.204
		N	123.359
71	**LYS**	HN	7.871
		HA	3.927
		HB2	1.519
		HB3	1.637
		HD2	1.490
		HE2	2.817
		HG2	1.222
		N	128.307

Residue number	Residue type	Atom	Chemical shift (ppm)
I	**HEME**	2^1CH_3	3.523
		3^1H	6.259
		3^2CH_3	2.088
		5H	9.601
		7^1CH_3	3.525
		8^1H	6.242
		8^2CH_3	1.750
		10H	9.076
		12^1CH_3	2.507
		13^1CH_2	3.363
			4.216
		13^2CH_2	2.507
			3.068
		15H	9.218
		17^1CH_2	3.906
			3.964
		17^2CH_2	2.939
			2.993
		18^1CH_3	3.305
		20H	9.454
III	**HEME**	2^1CH_3	4.097
		3^1H	6.550
		3^2CH_3	2.935
		5H	10.530
		7^1CH_3	3.461
		8^1H	4.308
		10H	10.102
		12^1CH_3	3.812
		13^1CH_2	3.787
			4.132
		13^2CH_2	2.798
			2.937
		15H	6.870
		17^1CH_2	4.120
			4.188
		17^2CH_2	3.218
			9.808
		18^1CH_3	1.697
		20H	9.416

Residue number	Residue type	Atom	Chemical shift (ppm)
IV	**HEME**	2^1CH_3	3.580
		3^1H	5.992
		3^2CH_3	2.023
		5H	8.974
		7^1CH_3	2.978
		8^1H	6.236
		8^2CH_3	1.503
		10H	9.288
		12^1CH_3	3.907
		13^1CH_2	3.847
			4.121
		13^2CH_2	3.062
			3.677
		15H	9.431
		17^1CH_2	4.428
			3.950
		17^2CH_2	3.097
			3.474
		18^1CH_3	3.307
		20H	9.353

A.3 Assignment of the heme signals of PpcA mutants in the reduced form

Table A.3 – Chemical shifts (ppm) of the heme protons of PpcAF15L in the reduced state at pH 8.0 and 15 °C.

Heme substituent	Heme I	Heme III	Heme IV
5H	9.49	10.63	9.03
10H	8.92	9.78	9.37
15H	9.28	9.46	9.56
20H	9.50	9.97	9.41
2^1CH_3	3.56	4.40	3.63
7^1CH_3	3.43	4.12	3.02
12^1CH_3	2.86	3.47	4.02
18^1CH_3	3.34	3.81	3.36
3^1H	6.17	7.33	6.04
8^1H	6.10	6.56	6.29
3^2CH_3	2.16	2.98	2.06
8^2CH_3	1.43	2.91	1.54

Table A.4 – Chemical shifts (ppm) of the heme protons of PpcAM58 mutants in the reduced state at pH 8.0 and 15 °C.

Heme substituent	Mutant	Heme I	Heme III	Heme IV
5H	M58D	9.61	10.57	9.00
	M58K	9.64	10.58	9.01
	M58N	9.63	10.61	9.01
	M58S	9.63	10.58	9.01
10H	M58D	9.08	9.84	9.31
	M58K	9.12	9.68	9.32
	M58N	9.11	9.76	9.33
	M58S	9.12	9.82	9.31
15H	M58D	9.25	9.47	9.50
	M58K	9.27	9.49	9.54
	M58N	9.27	9.52	9.54
	M58S	9.28	9.49	9.54
20H	M58D	9.49	10.14	9.38
	M58K	9.51	10.15	9.40
	M58N	9.51	10.17	9.40
	M58S	9.51	10.14	9.39
2^1CH_3	M58D	3.54	4.33	3.60
	M58K	3.56	4.32	3.62
	M58N	3.56	4.33	3.62
	M58S	3.56	4.33	3.62
7^1CH_3	M58D	3.56	4.11	3.00
	M58K	3.58	4.13	3.01
	M58N	3.58	4.13	3.03
	M58S	3.58	4.13	3.02
12^1CH_3	M58D	2.51	3.48	3.93
	M58K	2.55	3.44	3.94
	M58N	2.54	3.45	3.95
	M58S	2.55	3.48	3.94
18^1CH_3	M58D	3.33	3.87	3.33
	M58K	3.34	3.86	3.34
	M58N	3.35	3.87	3.35
	M58S	3.35	3.86	3.35
3^1H	M58D	6.28	6.89	6.00
	M58K	6.28	6.91	6.02
	M58N	6.29	6.91	6.02
	M58S	6.28	6.91	6.03
8^1H	M58D	6.26	6.68	6.26
	M58K	6.31	6.47	6.27
	M58N	6.28	6.66	6.28
	M58S	6.31	6.66	6.26
3^2CH_3	M58D	2.13	1.77	2.06
	M58K	2.13	1.77	2.05
	M58N	2.13	1.77	2.06
	M58S	2.13	1.78	2.06
8^2CH_3	M58D	1.79	2.97	1.49
	M58K	1.85	2.97	1.55
	M58N	1.79	2.98	1.54
	M58S	1.83	2.95	1.54

Table A.5 – Chemical shifts (ppm) of the heme protons of PpcAK9 mutants in the reduced state at pH 8.0 and 15 °C.

Heme substituent	Mutant	Heme I	Heme III	Heme IV
5H	K9Q	9.65	10.58	9.03
	K9E	9.64	10.57	9.01
10H	K9Q	9.13	9.86	9.34
	K9E	9.12	9.85	9.32
15H	K9Q	9.27	9.46	9.54
	K9E	9.25	9.45	9.51
20H	K9Q	9.51	10.15	9.40
	K9E	9.50	10.13	9.39
2^1CH_3	K9Q	3.56	4.35	3.62
	K9E	3.55	4.34	3.60
7^1CH_3	K9Q	3.58	4.14	3.02
	K9E	3.56	4.13	3.01
12^1CH_3	K9Q	2.56	3.50	3.95
	K9E	2.55	3.49	3.94
18^1CH_3	K9Q	3.35	3.86	3.35
	K9E	3.33	3.84	3.35
3^1H	K9Q	6.30	6.91	6.04
	K9E	6.29	6.90	6.03
8^1H	K9Q	6.29	6.60	6.29
	K9E	6.29	6.59	6.27
3^2CH_3	K9Q	2.13	1.74	2.06
	K9E	2.12	1.71	2.04
8^2CH_3	K9Q	1.79	2.98	1.56
	K9E	1.78	2.98	1.54

Table A.6 – Chemical shifts (ppm) of the heme protons of PpcAK18 mutants in the reduced state at pH 8.0 and 15 °C.

Heme substituent	Mutant	Heme I	Heme III	Heme IV
5H	K18Q	9.63	10.58	9.02
	K18E	9.63	10.58	9.02
10H	K18Q	9.11	9.86	9.33
	K18E	9.10	9.86	9.34
15H	K18Q	9.27	9.46	9.54
	K18E	9.28	9.45	9.54
20H	K18Q	9.51	10.15	9.40
	K18E	9.52	10.15	9.40
2^1CH_3	K18Q	3.56	4.35	3.62
	K18E	3.56	4.35	3.62
7^1CH_3	K18Q	3.57	4.13	3.02
	K18E	3.57	4.13	3.02
12^1CH_3	K18Q	2.55	3.50	3.95
	K18E	2.55	3.50	3.95
18^1CH_3	K18Q	3.34	3.85	3.35
	K18E	3.34	3.85	3.35
3^1H	K18Q	6.28	6.91	6.04
	K18E	6.28	6.92	6.04
8^1H	K18Q	6.28	6.60	6.29
	K18E	6.27	6.60	6.29
3^2CH_3	K18Q	2.14	1.75	2.06
	K18E	2.13	1.76	2.06
8^2CH_3	K18Q	1.78	2.98	1.56
	K18E	1.79	2.97	1.56

Table A.7 – Chemical shifts (ppm) of the heme protons of PpcAK22 mutants in the reduced state at pH 8.0 and 15 °C.

Heme substituent	Mutant	Heme I	Heme III	Heme IV
5H	K22Q	9.64	10.58	9.02
	K22E	9.63	10.58	9.02
10H	K22Q	9.12	9.86	9.33
	K22E	9.11	9.86	9.34
15H	K22Q	9.26	9.46	9.54
	K22E	9.26	9.47	9.55
20H	K22Q	9.51	10.15	9.40
	K22E	9.51	10.15	9.40
2^1CH_3	K22Q	3.56	4.35	3.62
	K22E	3.56	4.35	3.62
7^1CH_3	K22Q	3.57	4.14	3.02
	K22E	3.57	4.14	3.02
12^1CH_3	K22Q	2.55	3.50	3.95
	K22E	2.55	3.50	3.95
18^1CH_3	K22Q	3.34	3.86	3.35
	K22E	3.34	3.87	3.35
3^1H	K22Q	6.28	6.91	6.04
	K22E	6.27	6.91	6.04
8^1H	K22Q	6.29	6.60	6.28
	K22E	6.29	6.61	6.29
3^2CH_3	K22Q	2.13	1.74	2.05
	K22E	2.14	1.77	2.05
8^2CH_3	K22Q	1.80	2.97	1.56
	K22E	1.81	2.97	1.56

Table A.8 – Chemical shifts (ppm) of the heme protons of PpcAK52 mutants in the reduced state at pH 8.0 and 15 °C.

Heme substituent	Mutant	Heme I	Heme III	Heme IV
5H	K52Q	9.65	10.54	9.12
	K52E	9.64	10.51	9.21
10H	K52Q	9.10	9.86	9.38
	K52E	9.10	9.85	9.39
15H	K52Q	9.27	9.48	9.55
	K52E	9.26	9.48	9.56
20H	K52Q	9.51	10.18	9.40
	K52E	9.51	10.20	9.39
2^1CH_3	K52Q	3.56	4.38	3.62
	K52E	3.57	4.40	3.62
7^1CH_3	K52Q	3.58	4.13	3.04
	K52E	3.57	4.12	3.11
12^1CH_3	K52Q	2.55	3.51	3.96
	K52E	2.54	3.51	3.97
18^1CH_3	K52Q	3.35	3.86	3.35
	K52E	3.35	3.87	3.35
3^1H	K52Q	6.29	6.89	6.06
	K52E	6.28	6.87	6.09
8^1H	K52Q	6.27	6.57	6.35
	K52E	6.25	6.57	6.39
3^2CH_3	K52Q	2.13	1.81	2.08
	K52E	2.13	1.85	2.09
8^2CH_3	K52Q	1.79	2.97	1.65
	K52E	1.76	2.96	1.66

Table A.9 – Chemical shifts (ppm) of the heme protons of PpcAK60 mutants in the reduced state at pH 8.0 and 15 °C.

Heme substituent	Mutant	Heme I	Heme III	Heme IV
5H	K60Q	9.65	10.56	9.02
	K60E	9.65	10.56	9.03
10H	K60Q	9.12	9.85	9.34
	K60E	9.12	9.86	9.34
15H	K60Q	9.26	9.45	9.53
	K60E	9.27	9.47	9.54
20H	K60Q	9.51	10.14	9.40
	K60E	9.51	10.15	9.40
2^1CH_3	K60Q	3.56	4.36	3.62
	K60E	3.56	4.35	3.62
7^1CH_3	K60Q	3.57	4.13	3.03
	K60E	3.58	4.14	3.03
12^1CH_3	K60Q	2.55	3.44	3.95
	K60E	2.55	3.47	3.95
18^1CH_3	K60Q	3.34	3.86	3.35
	K60E	3.35	3.87	3.35
3^1H	K60Q	6.29	6.90	6.04
	K60E	6.29	6.91	6.04
8^1H	K60Q	6.28	6.60	6.29
	K60E	6.29	6.61	6.29
3^2CH_3	K60Q	2.12	1.74	2.05
	K60E	2.13	1.77	2.06
8^2CH_3	K60Q	1.78	2.97	1.55
	K60E	1.81	2.97	1.54

A.4 Ongoing and future studies experimental procedures

A.4.1 Studies on PpcA in the paramagnetic oxidized state

A.4.1.1 Protein expression and purification

Unlabeled and ^{15}N labeled PpcA protein were prepared as described in Chapter 2. $^{13}C/^{15}N$ labeled PpcA was prepared as the ^{15}N labeled protein, but with addition of 2 g/L ($^{13}C_6$)D-glucose to minimal media.

A.4.1.2 NMR spectroscopy

A.4.1.2.1 Sample preparation

Oxidized 1.2 mM samples of unlabeled PpcA were prepared in 45 mM phosphate buffer pH 5.5 with NaCl (100 mM final ionic strength) in 92%H_2O/8%D_2O or in 99% D_2O using 3 mm diameter NMR tubes. ^{15}N and $^{13}C/^{15}N$ labeled PpcA samples were prepared in the same buffer in 92%H_2O/8%D_2O.

A.4.1.2.2 NMR experiments

In the oxidized state, the following set of experiments was acquired: $^{13}C/^{15}N$ labeled sample: 2D ^{1}H-^{15}N-HSQC and 3D HNCA, HNCOCA, HNCACB, HNCOCACB, (H)CCH-TOCSY (45ms) and HC(C)H-TOCSY (45 ms) spectra; unlabeled sample in 92% H_2O/8% D_2O: 2D-^{1}H-COSY, 2D-^{1}H-TOCSY (25 and 75 ms) and 2D-^{1}H-NOESY (80 ms); unlabeled sample in D_2O: 2D-^{1}H-COSY, 2D-^{1}H-TOCSY (25 and 70 ms) and 2D-^{1}H-NOESY (30 and 80 ms). Spectra were acquired with a sweep width of 20 ppm (^{15}N-HSQC, HNCA, HNCOCA, HNCACB, HNCOCACB) or 40 ppm (3D TOCSY and 2D) in the proton dimension, 60 (HNCA, HNCOCA, HNCACB, HNCOCACB) or 90 ppm (3D TOCSY) in the carbon dimension and 45 ppm in the nitrogen dimension. In order to discriminate between the polypeptide chain and heme signals, 2D-^{1}H-^{13}C-HSQC NMR spectra were acquired on both labeled (80 scans) and unlabeled (640 scans) samples with a spectral window of 40 ppm and 250 ppm in proton and carbon dimensions, respectively.

A.4.1.3 Assignment strategy and methodology

A.4.1.3.1 Assignment of heme signals in the oxidized state

In the oxidized form, PpcA is paramagnetic and the unpaired electron of each heme iron exerts significant paramagnetic shifts on the heme signals and nearby residues. In this case, the strategy for the assignment of the heme substituents signals is different and relies on the analysis of ^{1}H-^{13}C-HSQC NMR spectra and on the assignments obtained from NMR redox titrations [1]. In the ^{1}H-^{13}C-HSQC NMR obtained for the unlabeled sample, the propionate α ($13^{1}CH_2$ and $17^{1}CH_2$) and β ($13^{2}CH_2$ and $17^{2}CH_2$) CH_2 groups appear in characteristic

positions in the ^{13}C dimension. These are 5 to 25 ppm for the α groups and 70 to 100 ppm for the β groups.

In the TOCSY spectrum the connectivities between the pairs of propionate CH_2 groups are identified and in the NOESY spectrum is possible to identify connectivities with the closest methyl group. The assignment of the remaining heme protons follows the strategy used for the proteins in the reduced state.

A methodology that combines the analysis of ^{1}H-^{13}C-HSQC NMR spectra obtained for labeled and unlabeled samples was developed in our laboratory and allows a straightforward discrimination between the heme cofactors signals and those from the polypeptide chain, and their confident assignment [2]. This methodology is described on Chapter 6.

A.4.1.3.2 Assignments of protein backbone and side chain signals

For $^{13}C/^{15}N$ labeled proteins, the backbone assignment is made by the analysis of the 3D HNCA spectrum, that correlates HN^{i} with $C\alpha^{i}$ and $C\alpha^{i-1}$, together with the HNCOCA that correlates HN^{i} only with $C\alpha^{i-1}$ (Figure A.1). HNCACB and HNCOCACB spectra allow assigning the β carbons of the protein residues with the same strategy.

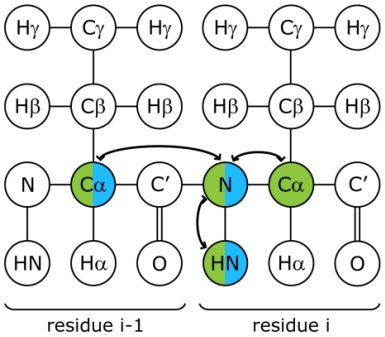

Figure A.1 – Connectivities observed in tridimensional spectra for $^{13}C/^{15}N$ labeled proteins. 3D-HNCA connectivities are represented in green and 3D-HNCOCA connectivities in blue.

For side chain assignment the (H)CCH-TOCSY and HC(C)H-TOCSY spectra are used. In these spectra the carbon and proton side chain resonances are observed for each CH, respectively (Figure A.2).

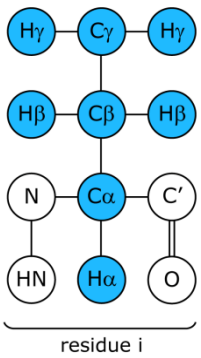

Figure A.2 – Connectivities observed in tridimensional TOCSY spectra for $^{13}C/^{15}N$ labeled proteins.

A.4.1.4 NMR structure determination

Restraints are determined from 2D-^{1}H-NOESY spectra in the same way as for the reduced protein. However, in the oxidized state, two sets of integrated peaks obtained at different mixing times (80 and 30 ms) were used.

Besides the non-standard residue types used in the reduced state, two types of histidine ligands were used for structure calculations for the oxidized state [3]. A set of 96 fixed upper limit distances associated with non-standard residues was used as input for PARADYANA for calculations.

In the oxidized state, dipolar shifts were used during structure determination and refinement, since these shifts depend on the position of the nucleus relative to the paramagnetic centers and their magnetic axes. Approximate dipolar shifts were determined by subtracting the shifts for the reduced protein from those for the oxidized protein, as previously described [4,5]. Volume restraints were also corrected for paramagnetic leakage as previously described [4]. Structure calculation was performed with the program PARADYANA, with peak volumes and dipolar shifts as input [3]. Analysis and refinement of the structure was performed as for the reduced protein.

A.4.2 *In vivo* studies of mutated forms of PpcA

This part of the work was developed at the Department of Microbiology at the University of Massachusetts in Amherst, Massachusetts, USA, integrated in the Geobacter Project (www.geobacter.org).

After the analysis of the results obtained *in vitro* for the mutated PpcA forms, four mutants (PpcAF15L, PpcAK52E, PpcAM58K and PpcAM58S) were selected for complementation studies in the PpcA knockout mutant *Geobacter sulfurreducens* DL3 strain [6].

A.4.2.1 DNA manipulations

Genomic DNA extractions were performed with the MasterPure™ Complete DNA and RNA Purification Kit (Epicentre Biotechnologies). PCR product purification and plasmid DNA purification were carried out with the QIAquick Gel Extraction Kit (QIAGEN) and the QIAprep Spin Miniprep Kit (QIAGEN), respectively. DNA manipulations were performed according to the methods described by Sambrook *et al.* [7]. Primers were purchased from Eurofins MWG Operon, and restriction enzymes and T4 DNA ligase from New England Biolabs. DyNAzyme II polymerase (Finnzymes) was used for amplification from genomic DNA and *Taq* DNA polymerase (QIAGEN) for colony PCR. *E. coli* TOP10 cells were used during DNA manipulation.

A.4.2.2 Cloning of ppcA gene in pRG5 complementation plasmid

Wild-type *G. sulfurreducens* DL1 [8] was obtained from the laboratory culture collection and grown at 30°C on acetate-fumarate medium under anaerobic conditions in an atmosphere of N_2/CO_2 (80:20) for genomic DNA extraction.

ppcA gene was amplified from *G. sulfurreducens* genomic DNA with primers cytP_for (forward primer: GGGGAATTCGGTTGCGTTTTCATCAACCTG) and cytP_rev (reverse primer: GGGGGATCCGCACCTCAGTGAAGTAACG), using a touchdown approach for PCR (underlined nucleotides highlight recognition sites for restriction enzymes; EcoRI for primer forward and BamHI for primer reverse). PCR products were analyzed in 1% agarose gels and purified.

The complementation plasmid used was pRG5 [9], that has been previously used for complementation studies of other proteins. Both vector and fragment were digested with EcoRI and BamHI and purified. Ligation was carried out with a insert:vector molar ratio of 3:1, overnight at 16 °C. The ligation product was transformed into *E. coli* TOP10 competent cells and the cells plated for selection in LB medium supplemented with spectinomycin (100 μg/mL). The resulting colonies were screened by colony PCR with M13 primers (M13F: GTAAAACGACGGCCAG and M13R: CAGGAAACAGCTATGAC), and those with a PCR product of the correct size were grow in liquid LB supplemented with spectinomycin for plasmid extraction and sequencing. The resulting plasmid was designated pMA59.

A.4.2.3 Site directed mutagenesis of pMA59

The QuikChange Site-Directed Mutagenesis kit (Stratagene) was used to prepare the plasmid pMA59 single mutants with the primers shown in Table A.10.

Table A.10 – Primers used for site-directed mutagenesis of pMA59. Capital letters highlight the mutated base pairs.

	Forward primer sequence (5'→3')	Reverse primer sequence (5'→3')	Plasmid
F15L	ggtgatgtgaagCtcccgcacaaggccc	gggccttgtgcgggaGcttcacatcacc	pMA63
K52E	gcaagggctgcGaggggtgccacgaag	cttcgtggcacccctCgcagcccttgc	pMA64
M58K	gtgccacgaagaaaAgaagaaggggccgac	gtcggccccttcttcTtttcttcgtggcac	pMA65
M58S	gggtgccacgaagaaaGCaagaaggggccg	cggccccttcttGCtttcttcgtggcaccc	pMA66

A.4.2.4 Preparation of G. sulfurreducens DL3 complementation mutants

A.4.2.4.1 Culturing conditions and growth media

The manipulation of *G. sulfurreducens* was performed according to its developed genetic system and cultures were grown at 30°C under anaerobic conditions [10]. In every step, NBAF medium was used for growth. NBAF contains 15mM acetate as electron donor, 40mM fumarate as electron acceptor, and a mixture of vitamins, salts and minerals. All media were dispensed into anaerobic pressure tubes or bottles with butyl rubber stoppers and bubbled with a N_2:CO_2 (80:20) gas mixture to remove dissolved oxygen and obtain a final pH of

about 6.7. Before inoculums, media was supplemented with 0.1% yeast extract and 1mM cysteine. An anoxic solution of spectinomycin was prepared and added to the media in a final concentration of 400 μg/mL. Plating and incubations on solid media were performed inside an anaerobic glove bag (Coy Laboratory Products Inc) with the atmosphere heated to 30°C.

A.4.2.4.2 Electroporation and plating

Electrocompetent *G. sulfurreducens* DL3 cells were prepared according to the procedure described by Coppi *et al.* [10]. Plasmids were electroporated into *G. sulfurreducens* DL3 using a GenePulser electroporator (Bio-Rad) as previously described [10]. After electroporation, cells were grown in liquid media for 5 hours for recovery before plating.

When pink colonies were visible, each culture was streaked to new plates and after to liquid media. Freezer stocks with 10% DMSO and genomic DNA extraction were performed.

A.4.3 Interaction studies with PpcA putative redox partners

A.4.3.1 DNA manipulations

PCR products were purified using Wizard® PCR Preps DNA Purification System (Promega), digested vector using E-gel® Electrophoresis System (Invitrogen) and plasmids using NZYMiniprep kit (NZYTech).

Primers were purchased from Invitrogen, restriction enzymes from Fermentas and T4 DNA ligase from NZYTech. Phusion High-Fidelity DNA polymerase (Finnzymes) was used for amplification from genomic DNA and *Taq* DNA polymerase (VWR) for colony PCR. *E. coli* DH5α cells were used during DNA manipulation.

A.4.3.2 Cloning of macA *gene in vector pVA203*

The same vector used for cloning of PpcA homologs, pVA203 [11], was used for cloning of *macA* gene (GSU0466).

macA gene, without its own leader sequence, was amplified from *G. sulfurreducens* genomic DNA with primers GSU0466_fw2 (forward primer: GCGTCGCGGCCGCGAAAGAGGATGTCATGAAACG) and GSU0466_rv2 (reverse primer: CCGGTGCAAAGAATTCTCAGTTGCTGACCGGCCTGG), by PCR (underlined nucleotides highlight recognition sites for restriction enzymes; NotI for primer forward and EcoRI for primer reverse). PCR products were analyzed in 0.8% agarose gels and purified.

Both vector and fragment were digested with NotI and EcoRI and purified. Ligation was carried out with an insert:vector molar ratio of 5:1, for 16 hours at 16 °C. The ligation product was transformed into *E. coli* DH5α competent cells and the cells plated for selection in LB medium supplemented with ampicillin (100 μg/mL). The resulting colonies were screened by colony PCR with pCK32 primers (pCK32_fw: GGCTCGTATGTTGTGTGGAA and pCK32_rv: AAGGGAAGAAAGCGAAAGGA), and those with a PCR product of the correct size

were grow in liquid LB supplemented with ampicillin for plasmid extraction and sequencing. The resulting plasmid was designated pCS466.

A.4.3.3 MacA heterologous expression

Preliminary tests for overexpression of MacA in *E. coli* have been performed using the same protocol used for the expression of PpcA described in Chapter 2 [12].

A.5 Assignment of the heme resonances of PpcA in the oxidized form

Table A.11 – ^{1}H and ^{13}C chemical shifts (ppm) of the heme substituents in the oxidized triheme PpcA. The resonances not detected by the direct comparison of the two spectra in Figure 6.1 are indicated by 'n.d.'.

Heme Substituent	Heme I		Heme III		Heme IV	
	^{1}H	^{13}C	^{1}H	^{13}C	^{1}H	^{13}C
$2^{1}CH_3$	17.79	-36.72	12.18	-23.86	14.46	-32.40
$3^{1}H$	0.91	-13.55	-2.56	-21.36	0.72	-6.69
$3^{2}CH_3$	1.15	61.34	-2.24	75.98	2.05	62.28
5H	n.d.	n.d.	-3.90	46.67	n.d.	n.d.
$7^{1}CH_3$	10.43	-23.09	18.00	-41.15	10.99	-23.26
$8^{1}H$	-4.34	-8.80	-0.86	26.54	-0.04	-7.40
$8^{2}CH_3$	-4.00	53.13	-1.01	16.02	1.63	62.33
10H	-1.54	23.42	n.d.	n.d.	1.13	n.d.
$12^{1}CH_3$	20.65	-49.63	13.18	-22.61	17.38	-36.95
$13^{1}CH_2$	2.63 6.72	-18.00	16.09 19.94	-58.02	2.43 6.45	-18.59
$13^{2}CH_2$	-1.48 -0.33	95.68	-1.74 -0.68	n.d.	0.10 0.44	98.50
15H	3.71	0.62	-1.67	46.87	0.75	13.50
$17^{1}CH_2$	0.89 3.01	-6.89	3.67 5.55	-16.05	2.87 4.18	-14.37
$17^{2}CH_2$	-0.87 -0.43	73.87	-2.07 -2.00	87.29	-0.86 -0.26	89.76
$18^{1}CH_3$	15.71	-37.62	0.64	-1.63	14.58	-36.32
20H	-0.70	n.d.	8.07	46.71	-1.60	32.42

A.6 References

[1] CA Salgueiro, DL Turner, AV Xavier (1997) Use of paramagnetic NMR probes for structural analysis in cytochrome c_3 from *Desulfovibrio vulgaris*, Eur J Biochem 244, 721-734.

[2] L Morgado, AP Fernandes, YY Londer, M Bruix, CA Salgueiro (2010) One simple step in the identification of the cofactors signals, one giant leap for the solution structure determination of multiheme proteins, Biochem Biophys Res Commun 393, 466-470.

[3] DL Turner, L Brennan, SG Chamberlin, RO Louro, AV Xavier (1998) Determination of solution structures of paramagnetic proteins by NMR, Eur Biophys J 27, 367-375.

[4] VB Paixão, H Vis, DL Turner (2010) Redox linked conformational changes in cytochrome c_3 from *Desulfovibrio desulfuricans* ATCC 27774, Biochemistry 49, 9620-9629.

[5] AC Messias, AP Aguiar, L Brennan, CA Salgueiro, LM Saraiva, AV Xavier, DL Turner (2006) Solution structures of tetrahaem ferricytochrome c_3 from *Desulfovibrio vulgaris* (Hildenborough) and its K45Q mutant: the molecular basis of cooperativity, Biochim Biophys Acta 1757, 143-153.

[6] JR Lloyd, C Leang, AL Hodges Myerson, MV Coppi, S Cuifo, B Methe, SJ Sandler, DR Lovley (2003) Biochemical and genetic characterization of PpcA, a periplasmic *c*-type cytochrome in *Geobacter sulfurreducens*, Biochem J 369, 153-161.

[7] J Sambrook, EF Fritsch, T Maniatis, Molecular Cloning: a laboratory manual, Cold Spring Harbor Laboratory Press, New York, 1989.

[8] F Caccavo, Jr., DJ Lonergan, DR Lovley, M Davis, JF Stolz, MJ McInerney (1994) *Geobacter sulfurreducens* sp. nov., a hydrogen- and acetate-oxidizing dissimilatory metal-reducing microorganism, Appl Environ Microbiol 60, 3752-3759.

[9] BC Kim, C Leang, YH Ding, RH Glaven, MV Coppi, DR Lovley (2005) OmcF, a putative *c*-type monoheme outer membrane cytochrome required for the expression of other outer membrane cytochromes in *Geobacter sulfurreducens*, J Bacteriol 187, 4505-4513.

[10] MV Coppi, C Leang, SJ Sandler, DR Lovley (2001) Development of a genetic system for *Geobacter sulfurreducens*, Appl Environ Microbiol 67, 3180-3187.

[11] PR Pokkuluri, YY Londer, NE Duke, J Erickson, M Pessanha, CA Salgueiro, M Schiffer (2004) Structure of a novel c_7-type three-heme cytochrome domain from a multidomain cytochrome *c* polymer, Protein Sci 13, 1684-1692.

[12] YY Londer, PR Pokkuluri, DM Tiede, M Schiffer (2002) Production and preliminary characterization of a recombinant triheme cytochrome c_7 from *Geobacter sulfurreducens* in *Escherichia coli*, Biochim Biophys Acta 1554, 202-211.